FLOWFIELD CHARACTERIZATION OF THE BOEING/AFOSR MACH-6 QUIET TUNNEL

A Thesis

Submitted to the Faculty

of

Purdue University

by

Kathryn A. Gray

In Partial Fulfillment of the

Requirements for the Degree

of

Master of Science in Aeronautics and Astronautics

December 2018

Purdue University

West Lafayette, Indiana

THE PURDUE UNIVERSITY GRADUATE SCHOOL
STATEMENT OF THESIS APPROVAL

Dr. Steven P. Schneider, Chair

School of Aeronautics and Astronautics

Dr. Jonathan Poggie

School of Aeronautics and Astronautics

Dr. Katya Casper

Sandia National Laboratories

Approved by:

Dr. Weinong Wayne Chen

Head of the School Graduate Program

To my mom, who constantly inspires me with her strength, determination and perseverance.

ACKNOWLEDGMENTS

First, I'd like to thank Dr. Steven Schneider for giving me this opportunity and for his continued guidance and insight. Thanks also to my committee members, Jonathan Poggie of Purdue University and Katya Casper of Sandia National Laboratories, for their comments and suggestions. This work was funded by the Air Force Office of Scientific Research.

Thanks also to Jim Younts, Jerry Hahn, and Robin Snodgrass of the ASL machine shop, who not only quickly and expertly turned my designs into hardware, but who also patiently offered suggestions for improvements. I also greatly appreciate the help provided by John Phillips on all things electronic.

I wouldn't have been able to complete this work without the help of my labmates. In particular, thanks to Brandon, Greg, Josh, Cameron and Drew for your help and advice, but also thanks to all the other members of the Schneider lab for being a reliable source of support and entertainment. Thanks also goes to Ross Chaudhry at the University of Minnesota and Sebastien Esquieu of the French CEA for providing numerical data and additional insight.

Last but not least, thank you to my friends and family from all over for your love and support. Specifically, I'd like to thank those in Lafayette: Alex, Imad, Miller, Diane, the People's crew, and everyone else who has somehow managed to make life in Indiana fun.

TABLE OF CONTENTS

Page

LIST OF TABLES

LIST OF FIGURES

Figure Page

Figure Page

SYMBOLS

A	nozzle cross-sectional area at some axial location
D_f	forward-facing probe diameter
δ	shock standoff distance
δ^*	boundary-layer displacement thickness
f	frequency
γ	ratio of specific heats
h	height above cone
M	Mach number
p	pressure
ϕ	azimuthal location on the nozzle, clockwise from geographically southern side
R	nozzle radius at some axial location
Re	Reynolds number
t	time during the run
T	temperature
x/L	flat-plate location normalized by plate length
y	vertical position in tunnel
z	axial distance downstream of the throat

Subscripts

0	stagnation condition
i	initial condition
w	wall condition
1	pre-shock quantity
2	post-shock quantity

s	indicates shock-standoff quantity
d	indicates destructive frequency
r	indicates resonance frequency

Superscripts

$'$	fluctuations from the mean
$\bar{}$	mean
$\tilde{}$	RMS

ABBREVIATIONS

AEDC	Arnold Engineering Development Complex
AFOSR	Air Force Office of Scientific Research
BAM6QT	Boeing/AFOSR Mach-6 Quiet Tunnel
DNS	Direct Numerical Simulation
NACA	National Advisory Committee for Aeronautics
NASA	National Aeronautics and Space Administration
PSD	Power Spectral Density
RMS	Root-mean-square

ABSTRACT

Gray, Kathryn Anne MSAA, Purdue University, December 2018. Flowfield Characterization of the Boeing/AFOSR Mach-6 Quiet Tunnel. Major Professor: Steven P. Schneider.

The quiet-flow capabilities of the Boeing/AFOSR Mach-6 Quiet Tunnel have been well established in the last decade, but a full characterization of the nozzle flow is an ongoing project. Pitot probes outfitted with Kulite pressure transducers were used to further the investigation of the tunnel's flowfield. Noise levels were calculated by integrating the power spectral densities of the measured pitot pressure fluctuations, and experiments were performed to investigate several aspects of the flow.

First, the temperature distribution along the nozzle was varied to determine if heating had an effect on the stability of the laminar nozzle-wall boundary layer. Runs made with initial stagnation pressures slightly above the maximum quiet pressure determined that additional nozzle-wall heating did not have an effect on the amount of runtime which experienced quiet flow. In addition, pitot-probe measurements were taken at various locations to better determine the axial dependence of the noise levels. Experiments were also performed using pitot probes of varying forward-facing diameters to determine the effects of probe geometry on the measured fluctuations. The results were found to differ significantly from simulations and from a previous set of experimental data, but a likely cause of the discrepancies was not found. A pitot probe mounted on the base of a cone confirmed that the aft end of a model does experience quiet flow. Finally, characterization of the flowfield was attempted when the tunnel is run using helium. The measured pressures for these experiments have a significant level of uncertainty because the sensor calibration changes as helium diffuses across the diaphragm. Nevertheless, the measurements suggest that there may be periods of uniform flow, although these periods remain unstable and unsteady.

1. INTRODUCTION

Each wind tunnel has a unique set of characteristics that make it useful for simulating certain aspects of flight. Variations in Mach number, enthalpy, test section size, Reynolds number, and other parameters allow a wind tunnel to replicate various aspects of flight conditions. One characteristic that conventional high-speed wind tunnels do not share with flight is the high levels of freestream pressure fluctuations that originate on the nozzle walls [1, 2]. The root-mean-square (RMS) of the pitot-probe pressure fluctuations normalized by the mean pitot pressure are typically referred to as the noise level. While it may not affect most measurements, the noise level of a tunnel does have significant effects on boundary-layer transition measurements, often causing transition to occur sooner than in flight. In some cases, the high-noise environments of conventional wind tunnels can change or even bypass the mechanisms which lead to transition [3, 4]. The state of the boundary layer has significant impacts on heating, skin friction, control surface effectiveness, and aerodynamic loads which are even more pronounced at higher Mach numbers. Thus, the ability to predict where and when transition will occur is an important step in the design process of hypersonic vehicles. Semi-empirical methods do not take into account the complexities of transition, so a more physics-based approach is necessary for more accurate predictions. Quiet tunnels, which have noise levels similar to flight conditions, are therefore necessary for improving the understanding of transition.

1.1 Sources of Wind Tunnel Noise

In 1953, Kovasznay described the fluctuations in wind tunnels as a superposition of three modes: vorticity, entropy, and sound [5]. Vorticity fluctuations, or turbulence, originate in the stilling chamber. Experiments done by Laufer showed that

these fluctuations have no significant effect on transition Reynolds numbers when the Mach number (M) is above 2.5 [6]. Entropy fluctuation levels, also referred to as temperature spottiness, in "well-designed" supersonic tunnels are small and thought to be insignificant to transition [7]. While vorticity and entropy fluctuations are more relevant in the shear layer of supersonic turbulent flow, sound fluctuations are the most important source of noise in the freestream and therefore the largest factor in the effects of tunnel noise on transition measurements [6].

Laufer did experiments between Mach 1.6 and 5 using hot wires and argued that the fluctuations measured in the freestream originate from the turbulent boundary layers on the tunnel walls [6]. These fluctuations consist of sound waves whose intensity is approximately proportional to M^4 where M is the Mach number. He later attributed the noise to irregular streamwise variation in the turbulent boundary-layer displacement thickness on the nozzle wall [8]. Many other researchers have provided further evidence that pressure fluctuations in various wind tunnels are dominated by acoustic radiation from the turbulent nozzle-wall boundary layer [9–13].

Figure 1.1 is a shadowgraph image of a 5° half-angle cone at Mach 4.3 taken at the Naval Ordnance Lab ballistics range. It shows the effects that a turbulent boundary layer can have on the freestream. The upper surface of the cone has a boundary layer that is mostly laminar with intermittent turbulent spots, while the lower-surface boundary layer is fully turbulent. The radiating acoustic noise can be seen emanating from the regions of turbulence and is not present in the laminar flow regions. The sound waves are a result of the eddies in the turbulent boundary layer, which cause the freestream flow to encounter compression and expansion corners. The analogous streamwise variations in displacement thickness in a turbulent nozzle-wall boundary layer are the primary source of acoustic fluctuations in the tunnel freestream. The key to producing low levels of freestream pressure fluctuations in a quiet tunnel is maintaining a laminar boundary layer on the nozzle wall.

There have been many attempts to characterize and predict the pressure fluctuations that radiate from turbulent boundary layers on nozzle walls. Pate and Schueler

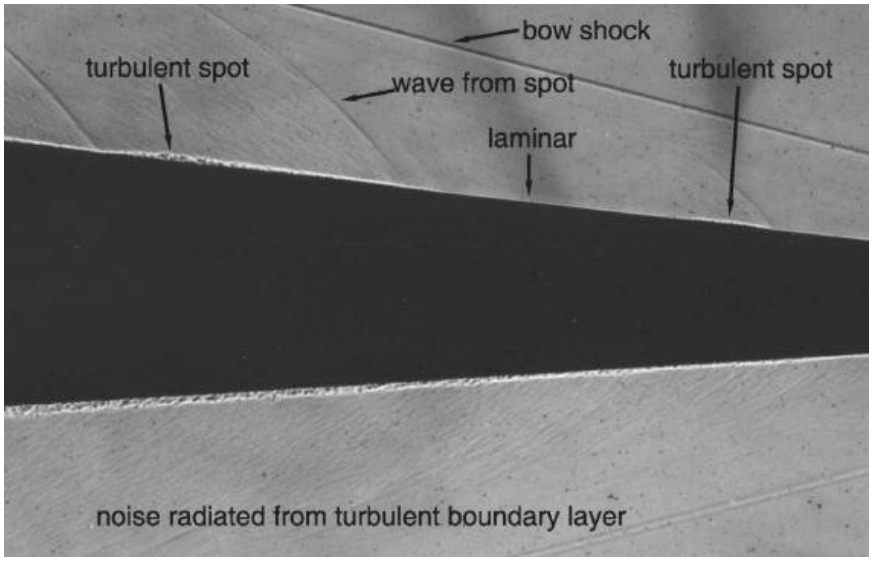

Figure 1.1. Shadowgraph of a 5° half-angle cone moving from left to right at Mach 4.3 illustrating the noise radiated off turbulent boundary layers. Image taken from Reference [1].

found that the disturbances decreased with increasing tunnel cross section [7]. In 1976, Stainback and Rainey presented a correlation for the intensity of freestream pressure fluctuations based on tunnel parameters such as temperature, area, shear stress, and freestream Mach number [14]. However, the correlation did not work as well for higher Mach numbers. Recent direct numerical simulations were performed by Duan to examine the pressure fluctuations generated from a turbulent Mach-6 boundary layer [15]. These disturbances were compared to those generated from a Mach-2.5 boundary layer, and both the amplitudes and peak frequencies of the pressure fluctuations were significantly larger for the larger Mach number. The features of the radiated disturbances were found to be consistent with the trends indicated by experimental data. Overall, the results further support the idea that the largest source of disturbances in high-speed tunnels is often the eddies in the turbulent nozzle-wall boundary layer. Note that this is particularly the case for blowdown tunnels where temperatures are not high enough to result in significant entropy fluctuations.

1.2 The Need for Quiet Tunnels

The acoustic fluctuations in the freestreams of conventional wind tunnels have been known to significantly affect the measured transition Reynolds number for decades. In the early 1950s, NACA discovered a difference in transition results at low supersonic speeds when measurements were made under comparable conditions in tunnels of various sizes [16]. It was believed that the scatter in transition Reynolds number was due to the differences in freestream pressure fluctuations between different tunnels. Following that discovery, transition Reynolds numbers in various high-speed tunnels under similar conditions were also found to display a significant scatter due to varying intensities of freestream acoustic disturbances radiating from the turbulent nozzle-wall boundary layers [13, 17].

Because the pressure fluctuations in tunnel freestreams varied among facilities and had a significant effect on transition, it was difficult to compare transition results taken in different tunnels. In 1969, Pate and Schueler quantified these noise effects to allow better comparisons between facilities. They studied transition data from the AEDC supersonic wind tunnels and published a correlation for transition Reynolds number based on tunnel noise [7]. The measurements were taken using 2D sharp leading edge models at 9 wind tunnel facilities between Mach 3 and 8. The correlation is a function of radiated aerodynamic noise parameters (displacement thickness and skin friction) and the tunnel test section circumference. It is independent of Mach and Reynolds numbers and also only applies to wind tunnels with turbulent nozzle-wall boundary layers. Pate's correlation for transition Reynolds numbers, like Stainback's correlation for tunnel noise, is not as accurate for higher Mach numbers. However, it was later shown that the inaccuracies at higher Mach numbers lead only to small variations in the location of transition.

Following Pate and Schueler's work, several other correlations between transition Reynolds number and tunnel noise were presented in the 1970s [18, 19]. Measurements taken much later at Purdue University indicate that the effects of tunnel noise

on transition cannot be fully explained with a simple correlation to the amplitude of freestream disturbances [3]. Still, recent attempts to correlate transition have shown promise. For example, Marineau developed methodologies to correlate transition in hypersonic wind tunnels using either measured pitot-pressure data or models of the freestream based on parameters used in Pate's correlation [20]. His methods successfully correlated cone measurements taken in AEDC's Tunnel 9 and Tunnel F at Mach numbers between 9 and 10 with an error in the predicted start of transition of about 14%. This is a significant improvement over predictions based on a constant N factor, which can result in errors greater than 40%, or fail to predict transition altogether. Although Marineau's efforts are specifically applicable only to second-mode dominated transition, it is a promising step towards better transition predictions in conventional tunnels. However, his methods require several adjustable parameters and it is therefore not clear how general the methods are. No correlation can encompass the complexities of transition or substitute for a physics-based model.

Since the freestream noise levels in conventional wind tunnels have been definitively shown to influence transition, the need for tunnels without this noise was obvious. Furthermore, it was shown that the source of the freestream pressure fluctuations was a turbulent nozzle-wall boundary layer. Thus, tunnels with laminar nozzle-wall boundary layers were developed. Methods used to ensure a laminar boundary layer include limiting particulates in the flow, highly polished nozzles, and removal of the turbulent boundary layer at the contraction. For details on the early development of quiet tunnels, see Reference [1].

After decades of experimentation, the first successful quiet tunnel was finished in 1983. Details about the tunnel's development and the features which reduced the freestream disturbances can be found in Reference [21]. NASA's Mach 3.5 Pilot Quiet Tunnel at Langley produced noise levels ranging between 0.03% to 0.8% of the mean pressure and freestream Reynolds numbers (Re) between 9.8×10^6 and 5.9×10^7 per meter [22]. The extent of the quiet core depended on the Reynolds number. For many experiments, only upstream regions of models were in the quiet flow region,

and downstream regions had elevated noise levels that may have had a significant effect on transition. It was found that transition is largely influenced by the noise incident on the upstream portion of a sharp cone [23]. However, it is likely that the disturbances which impinge on the model farther aft still have a significant effect [1].

A Mach-6 quiet tunnel was then built by NASA and the flow was initially characterized in 1991. It produced low-disturbance, uniform, Mach-5.91 flow up to a unit Reynolds number of about 10.0×10^6 /m [24]. The Mach number increased slightly with increasing Reynolds number, since a higher Reynolds number leads to a thinner boundary layer and thus a larger inviscid area in the nozzle. However, the Mach number did not vary by more than 1% inside the region of uniform flow. The nozzle was later shipped to Texas A&M University. There, efforts to characterize the flow showed a similar performance as was originally reported with noise levels as low as 0.06%, although there was increased intermittency during runs with higher initial stagnation pressures [25].

The Purdue hypersonic low-disturbance tunnel was designed to supplement the NASA facilities. The Boeing/AFOSR Mach-6 Quiet Tunnel (BAM6QT) was completed in 2001 and achieved low-pressure quiet flow in 2003. The history of characterizing the BAM6QT will be discussed in Section 1.5 and details about the facility are in Section 2.1.

1.3 Effects of Heating on Flow Stability

Temperature effects on boundary-layer stability have been studied in detail. In 1947, Lees used asymptotic linear stability theory to propose that a cool wall stabilizes a laminar boundary layer in air at low Mach numbers [26]. Heating has the reverse effect, destabilizing the low-speed boundary layer. It was later established by Mack that cooling stabilizes the first-mode disturbances, which are the most prevalent disturbances in low Mach-number flow [27]. The instabilities in higher supersonic and hypersonic flows are dominated by the second mode. The second-mode instability

grows more rapidly on cold walls and is destabilized by cooling [28]. Therefore, Mack concludes that uniform cooling has an overall destabilizing effect on boundary layers as the Mach number increases above 3 [29].

In supersonic wind tunnels, heating has been shown to increase the Reynolds number for which laminar flow is seen on nozzle walls [30, 31]. Stainback et al. heated the nozzle wall of a small, conventional Mach-5 tunnel using strip-type heaters wrapped around the outer surface of the nozzle and contraction [31]. Uniform wall temperatures up to about 478K were reached, with $T_w/T_0 = 1.4$. The unheated boundary layer experienced transition at $x = 27.18$ cm downstream from the nozzle throat at Re $= 7.8 \times 10^6$ /m. When the walls were heated, the transition unit Reynolds number at the same location increased by almost 20% to 9.3×10^6 /m. They postulated that the delay in transition was due to a thickening of the boundary layer with wall temperature. A thicker boundary layer is less sensitive to wall roughness of a given size than a thinner one and therefore less likely to transition to turbulence.

The effects of temperature distribution, rather than overall temperature, have also been investigated. Masad and Nayfeh studied the effects of both uniform heating and heating strips in subsonic boundary layers in air [32]. A subsonic boundary layer is dominated by the first mode, which was previously known to be destabilized by heating. In addition to confirming the flow was destabilized by uniform heating, Masad and Nayfeh found that both uniform cooling and strategically-placed heating strips were shown to provide a stabilizing effect. It was concluded that the localized heating reversed the direction of heat transfer downstream of the strips. Therefore, the downstream fluid was cooled by the wall and the first-mode-dominated boundary layer was more stable. It is clear that, at least for subsonic flows, both the temperature and the temperature distribution can affect boundary-layer stability.

Computations have been performed to investigate temperature distribution effects on supersonic flows. Gasperas used compressible linear stability theory and the e^N method to investigate the effects of temperature distribution on a Mach 6.84 flat-plate boundary layer [33]. The amplitudes of second-mode disturbances in the streamwise

direction were examined for three cases: an adiabatic wall, a cold wall with $T_w/T_0 = 0.4$, and a wall which was adiabatic until a location of $x/L = 0.2$, where a sharp linear drop reduced the temperature to that of the cold-wall case. The cold wall had larger second-mode instability amplitudes than the adiabatic wall for all locations. However, the wall with the linear drop in temperature resulted in even lower amplitudes than the adiabatic case at locations just downstream of $x/L = 0.2$. Upstream of that location, the instabilities were identical because both walls were adiabatic there. At $x/L = 0.4$, the amplitudes were similar to those on the adiabatic wall, although the frequencies differed. Farther downstream, the amplitudes grew and approached those of the cold wall. Thus, Gasperas showed that a streamwise decrease in temperature can have a stabilizing effect on a boundary layer.

Several efforts have shown that throat heating is an effective way to stabilize a nozzle-wall boundary layer. Demetriades showed that local surface heating in an 8-inch region centered on the throat results in fewer turbulent bursts and delays transition in the boundary layer of a Mach-3 nozzle [34]. Computational work done by Schneider utilized the e**N method and indicated that heating at the throat is an effective means of stabilizing the first-mode waves [35, 36]. Additionally, throat heating had a favorable effect on the second mode, which grows only near the nozzle exit. This is unexpected, as the decreasing wall temperature from the throat to the exit makes the wall seem cold and would therefore be expected to increase growth of the second mode. Uniform heating at the throat also thickens the boundary layer and therefore makes potential roughnesses appear smaller.

1.4 Effects of Probe Geometry on Measured Pressure Fluctuations

Measuring freestream disturbances in high-speed wind tunnels is not trivial, and many methods have been used, including intrusive methods such as hot wires and pitot probes. Placing any probe in the flow creates a bow shock through which the freestream passes. It is therefore nearly impossible to make direct measurements of the

freestream. The pressure fluctuations measured by a sensor are affected by the shock in ways that are not well understood. The transfer function defines the relationship between the pre-shock and post-shock frequency content of the disturbances and cannot be experimentally determined. Without knowledge of the transfer function, the freestream disturbances cannot be recovered from the measured disturbances without making significant assumptions.

It was known as early as the 1950s that the instrumentation used to measure the disturbances in supersonic flows is critical. Vrebalovich states three necessary criteria for such instruments: a high frequency response, a small enough size so that the probe does not prohibitively alter the flow, and a known response to various fluctuating quantities [37]. This last criterion refers to the idea of the transfer function, and it has been a goal of experimentalists to understand the effects of probe geometry on the transfer function for over half a century. Folsom summarized early work on this topic in 1956, showing that static-pressure measurements depend on the probe shape and size [38]. He also provides a calibration correction which varies considerably for different probe tip shapes.

Stainback and Wagner conducted experiments using both hot wires and a pressure transducer to measure fluctuating pitot pressures [39]. It was discovered that the pitot-pressure data had fluctuation amplitudes approximately 40% larger than those found using hot wires. They proposed that disturbances reflecting off the pitot-probe transducer face caused the increase in transfer function. The method they proposed to recover freestream static pressure fluctuations from pitot pressure fluctuations assumes transfer functions that are independent of both frequency and pitot probe geometry.

Further investigation into the influence of a pitot-probe geometry on the measured pressure fluctuations has been performed in recent years. Ali et al. used pitot probes with exchangeable heads to vary the forward-facing geometry and found that differences in forebody shape yielded significantly different pressure spectra [40]. Tunnel noise experiments made in the AEDC Hypervelocity Wind Tunnel 9 included mea-

surements taken using two different pitot-probe geometries, one with a cylindrical tip and one with a conical tip [41]. Noticeable differences between the power spectral densities for the two configurations were observed, namely that the conical geometry resulted in a smoother spectrum. However, the computed noise levels were not significantly different between the two cases.

Additional work has gone into studying the effects of cavity resonance on the measured disturbances. For example, McGilvray et al. used a combined experimental and numerical approach to research the possibility of a Helmholtz resonance in the cavity created by the shroud which protects a pressure transducer from the airflow [42]. A new design for the shielding which included a smaller cavity as shown to reduce a large portion of the recorded disturbances, showing that the measured pressure fluctuations was previously dominated by the resonance. Additionally, Hornung and Parziale made Euler computations of supersonic flow over a pitot tube and found that the pitot noise is amplified compared to the freestream noise by a factor which decreases with increasing Mach number [43]. They additionally found that a pitot probe with a cavity increases the amplification factor by at least a factor of 2 compared to the probe with a flat face. The results seen by both of these efforts indicate the significant role of resonance frequencies that are present when pitot probes contain cavities.

Chaudhry and Candler [44] performed direct numerical simulations to study the transfer function for various flat-faced pitot-probes with similar geometries that did not include a cavity. This analysis was done assuming axisymmetric freestream flow with flow-parallel acoustic disturbances of 200 discrete frequencies of constant amplitude such that the RMS pressure fluctuations was 1.4%. It was determined that the sound waves reflect between the shock and pitot-probe face and create a resonance measured by the sensor with a frequency defined as the standoff frequency. The standoff frequency f_s is defined as the speed of sound divided by twice the shock standoff distance. Integer multiples of f_s were found to experience destructive interference, and constructive interference was found to occur at $0.415 f_s$. Table 1.1 lists the shock

standoff distance (δ), primary destructive frequency ($f_{s,d}$), and primary resonance frequency ($f_{s,r}$) for four different probe diameters (D_f). The primary destructive frequency ($f_{s,d}$) is that which is most suppressed by the transfer function and is equal to the standoff frequency. The primary resonance frequency is that which is most amplified by the transfer function and is the frequency for which peak constructive interference occurs, or $f_{s,r} = 0.415 f_s$. The frequency values were calculated from Reference [44], and values for δ were determined using experimental measurements of the shock standoff distance for a body of revolution with a flat nose at Mach 6, which are presented on page 105 of Liepmann and Roshko [45].

Table 1.1. Standoff distance (δ), primary destructive frequency ($f_{s,d}$), and primary resonance frequency ($f_{s,r}$) for pitot probes with various forward-facing diameters (D_f). Note that these frequencies correspond to flow-parallel incident disturbances, and the results presented in Section 3.3 were computed using angled disturbances.

D_f [in]	δ [in]	$f_{s,d}$ [kHz]	$f_{s,r}$ [kHz]
0.066	0.019	431	179
0.118	0.033	246	102
0.236	0.066	124	51
0.284	0.080	102	42

Recent computations performed by Duan indicate that the acoustic waves that radiate from a Mach-6 turbulent boundary layer have a angle of about 120° [15]. Therefore, Chaudhry repeated the transfer function simulations with angled plane acoustic waves at 120° rather than flow-parallel disturbances. All other assumptions about the incident fluctuations remain the same. The resulting transfer functions are significantly different than the original simulations and matched more closely to experimental results [46]. The simulation results presented in Section 3.3 are those produced using angled disturbances and thus the primary destructive and resonance frequencies may not correspond to those listed in Table 1.1. It is unclear exactly

what effects the angled disturbances have on the predicted primary destructive and resonance frequencies, but further details on the new experiments will be published in Reference [47]. Nevertheless, Chaudhry's simulations do strongly suggest that probe geometry has a substantial impact on the transfer function.

Because the measured PSDs vary based on not only the wind tunnel in which they are measured but also the probe used for the experiments, comparisons between facilities are difficult unless the same pitot geometry is used in each tunnel. The freestream pressure fluctuations cannot be determined without knowing the transfer function for a specific probe. Although computations can provide an expected transfer function for a geometry, these cannot be directly compared to experimental results because simulations must assume a specific type of input disturbance which may not be present in an experiment. Chaudhry has developed a method for comparing ratios of numerically-derived transfer functions for a particular type of input disturbance to the ratios of experimentally-found PSDs [47]. Those methods and comparisons to the present work will be presented in Section 3.3.

1.5 Previous Characterization of Flow in the BAM6QT

The Boeing/AFOSR Mach-6 Quiet Tunnel was designed to meet the need for hypersonic wind tunnels with flight-like noise levels. At the throat is a set of bleed valves that, when opened, removes the nozzle-wall boundary layer to result in quiet flow conditions. Further details about the factors that contribute to quiet flow are included in Section 2.1. Although the BAM6QT was completed in 2001, initially the attempts to maintain a laminar boundary layer on the nozzle wall were unsuccessful. Preliminary measurements were made to determine flow uniformity, noise levels, and Mach number [48]. The noise levels were found to depend on stagnation pressure p_0, with values around 4% for $p_0 = 15$ psia and around 1% for $p_0 = 150$ psia. This trend is typical of conventional tunnels with turbulent nozzle-wall boundary layers [3]. The Mach number was also Reynolds-number dependent. The mean Mach number

on the centerline was about 6.0 at $Re \approx 0.3 \times 10^6$/ft and decreased to about 5.5 at $Re \approx 3 \times 10^6$/ft. Measurements made on the centerline at various axial locations showed a scatter in Mach number of about 2%, the cause of which was unknown. Additional data published in 2002 contributed to the early characterization of the BAM6QT nozzle [49]. These measurements confirmed that the noise level decreases with increasing Reynolds number but that values less than 0.1% were not seen. The noise levels were radially uniform, but were not low enough for the flow to be considered quiet. Again, varying Mach numbers were determined on the centerline, with values between 5.8 and 6.0.

Quiet flow was first achieved for pressures below $p_0 = 8$ psia in 2003 at various axial locations on the nozzle [50]. The Mach number for the quiet flow conditions was found to be 5.7. At higher pressures, which resulted in noisy flow conditions, the Mach number was found to decrease as axial distance from the throat increased. Borg took measurements in the contraction to determine if disturbances originating in the driver tube were significant enough to affect noise levels downstream [51]. His results did show disturbances in the contraction section caused by free convection and temperature gradients, but these were determined not to be the cause of early transition to turbulence. For initial stagnation pressures $p_{0,i}$ between 90 and 145 psia, an increase in temperature fluctuations was observed approximately 2.5 to 3 seconds into the run.

A surrogate aluminum throat was used in place of the electroformed-nickel throat section in an attempt to discover the reason for early transition at pressures above $p_0 = 8$ psia. Measurements using the surrogate throat were reported by Juliano in 2006 [52]. Once polished, the surrogate throat produced quiet noise levels up to $p_0 = 90$ psia consistently and up to 130 psia intermittently. Off-centerline measurements showed a noise increase at approximately $t = 1.5 - 2$ s into the run for $p_{0,i} = 95$ and 120 psia. Quiet-pressure data collected earlier by Skoch using the surrogate nozzle at stagnation pressures between 13 and 20 psia revealed noise levels between 0.03 and 0.06% [53]. Note that the polish on the surrogate throat was not as smooth as the

original nickel throat. These noise levels decreased with increasing stagnation pressure and were found to vary with axial location. A flaw was found in the bleed lip of the electroformed nozzle and was thought to be the probable cause of early transition with that throat. This section was modified to remove the flaw and reinstalled in the tunnel in August of 2006. Quiet flow was achieved for stagnation pressures up to 130 psia [52]. Typically, when the nozzle is opened the performance decreases because dust can settle in the nozzle, but successive dust-blowing runs slowly increase the maximum quiet pressure.

A comprehensive investigation of BAM6QT high-pressure, quiet-flow capabilities was reported by Steen [54] in 2010. At the time of most of those measurements, the maximum quiet pressure was around $p_0 = 140$ psia. For pressures below this value, quiet flow was achieved when the bleed valves were open, with noise levels typically around 0.01% for the first two seconds of the run. The method Steen used to calculate noise levels, which has been used for subsequent measurements including those presented in this work, utilizes the integrated pitot-pressure power spectral density up to 50 kHz. Further details are described in detail in Section 2.3. After approximately two seconds an increase in noise levels was observed, with some runs becoming noisy by the time of tunnel unstart. The magnitude of the increase was dependent on the measurement location and the Reynolds number. Only locations father downstream experienced this noise increase, which was larger for higher Reynolds numbers. Because this increase in noise was also seen when the surrogate throat was used, it is unlikely that it is caused by the throat. It is thought that this noise increase could originate in the contraction and may be related to the increase in temperature fluctuations observed by Borg.

Steen took pitot-probe measurements at various axial and radial locations to determine tunnel uniformity and measured noise levels for both quiet flow (bleed valve open) and noisy flow (closed bleed valve). She found that the Mach numbers for the bleeds-closed configuration were between 5.6 and 5.9 and the noise levels were between 1.5% and 4.5%. The noise levels decreased as the stagnation pressure increased

up to $p_{0,i} > 140$ psia, after which the noise levels were independent of pressure. It is strange that the noise levels above stagnation pressures of 140 psia do not continue to decrease with Reynolds number, since it is well established that the acoustic disturbances radiated from a turbulent boundary layer decrease as Reynolds number increases due to the thinning of the boundary layer [13]. The reasons for this finding have not been discovered. Steen found that the turbulent boundary layer was about 1.5 in. thick on the upper wall and 1.75 in. thick on the lower wall at $p_{0,i} = 90$ psia, and was thinner at higher pressures. When the bleed valve was opened, quiet flow was observed for $p_{0,i} \leq 140$ psia with noise levels typically around 0.01% and Mach numbers between 5.8 and 6.25. The spatial extent of the uniform quiet core was unknown, but a hot film that was installed 5 inches downstream of the nozzle exit indicated that there is still quiet flow at locations beyond the nozzle exit.

A series of attempts to clean the nozzle, also detailed by Steen, occurred in the spring and early summer of 2010. The nozzle was opened at various locations and tests were performed to determine the status of quiet flow. After opening the nozzle at Section 4 in June of that year, no quiet flow occurred. Scratches were found on the inner surface, so it was re-polished by Paul Thomas of American Pride Mold Polishing. It was reinstalled in July of that year, and the quiet pressure slowly increased over the course of several months of tunnel use. It is thought that these runs blew dust out of the nozzle, eventually raising the maximum quiet pressure to about 165 psia. This was towards the end of Steen's experiments, so her thesis did not include details about the flow quality after the re-polishing.

Long after the increase in quiet pressure, Sweeney performed further experiments to characterize the flow and build on Steen's work [55]. Using the same method of integrating power spectral densities, he found noise levels ranging from 2.0-2.5% when the bleed valve were closed. These were shown to be relatively constant across the diameter of the tunnel. For the most part, they decreased as Reynolds number increased, which is in line with the findings of Pate [13]. However, he does not present data for bleeds-closed runs with stagnation pressures above 140 psia and therefore

does not comment on the earlier findings of Steen. The Mach number was found to vary between 5.7 and 5.8, which is consistent with Steen's measurements. Overall, his results suggest that the flow characteristics for noisy flow were unchanged by the re-polishing. Pitot-pressure fluctuations measured with the bleed valve open confirmed the increase in maximum quiet pressure, revealing noise levels around 0.01% to 0.02% for $p_{0,i} < 170$ psia. The quiet noise levels were not dependent on stagnation pressure, but the number of turbulent bursts did increase for higher pressures. The quiet-flow Mach numbers ranged between 6.0 and 6.05 and were relatively uniform regardless of radial location.

1.6 Objectives

This thesis reports additional work done to better characterize the flow in the BAM6QT. Since extensive uniformity measurements have been made by Steen and Sweeney [54, 55], the focus for several of the present measurements was to follow up on topics discussed in their work. In addition, a few experiments were performed to test new and existing hardware. The following five topics were investigated:

1. Band heaters were used to vary the temperature distribution along the nozzle. These heaters were installed by Steen but had not been used. The tunnel was run using initial total pressures just above the maximum quiet pressure in order to determine if feasible changes in the nozzle temperature distribution have any effect on the maximum quiet pressure.

2. Previous researchers have found that the noise levels during quiet flow increase after approximately two seconds of runtime. Furthermore, it was discovered that this occurs at locations downstream of a certain point and is more obvious at higher Reynolds numbers. A pitot probe was placed at various axial locations to determine the precise location of the point where the noise increase begins. Comparisons were made between conditions at three different initial stagnation

pressures. Finding a more precise location for the beginning of this effect could grant insight into the nature and origin of this noise increase.

3. Pitot-probe sleeves were used to adjust the probe geometry to determine the resulting effects on the measured pressure fluctuations. Data from four forward-facing diameters were taken under identical conditions so comparisons could be made for both noisy and quiet flow. The results were then compared to direct numerical simulations and to previous measurements taken by Sweeney [55].

4. Previously, noise levels had only been measured using pitot probes without a model present. A pitot probe was mounted to the base of a 7-degree half-angle cone at zero angle of attack with the sensor facing upstream. The probe was placed at locations both inside and outside of the cone's shock to measure the pressure fluctuations. Noise levels were determined to verify that the flow is quiet at the aft end of a model.

5. Using helium instead of air would increase the Reynolds number for a given Mach number and increase the Mach number, so it is of interest to determine whether the BAM6QT can achieve uniform flow using helium. Pitot-probe measurements of the flow in the tunnel were taken using helium as the test gas. The data were compared to previous experiments using air and to numerical results produced by others.

2. FACILITY AND EXPERIMENTAL METHODS

2.1 The Boeing/AFOSR Mach-6 Quiet Tunnel

The experiments discussed here were performed in the Boeing/AFOSR Mach-6 Quiet Tunnel (BAM6QT) at Purdue University. It is one of only a few known hypersonic quiet tunnels in the world. A schematic of the BAM6QT is provided in Figure 2.1. The BAM6QT is a Ludwieg tube composed of a long driver tube, a converging-diverging nozzle, and a large vacuum tank. A burst-diaphragm system composed of two thin aluminum or mylar sheets separated by a gap is located between the diffuser and the vacuum tank. To operate the tunnel, the pressure in the driver tube is increased to the desired initial stagnation pressure, while the gap pressure is kept at half the difference between the upstream pressure and vacuum. To start airflow, the gap is evacuated and the pressure differential between the upstream diaphragm and the vacuum in the gap causes the upstream diaphragm to burst. The downstream diaphragm, which suddenly experiences the same large pressure differential, subsequently bursts. This causes a shock to propagate downstream into the vacuum tank and an expansion fan to propagate upstream through the nozzle, starting the wind tunnel. The expansion fan reflects between the two ends of the driver tube, causing a stagnation pressure drop of about 1% per reflection. Each cycle lasts about 200 ms, and during the reflection cycle the stagnation pressure is quasi-constant. Unstart occurs when the pressure difference between the driver tube and the vacuum is no longer large enough to maintain uniform supersonic flow in the nozzle, typically after about four seconds. The tunnel can be run using an initial stagnation pressure $p_{0,i}$ in the range of 5-300 psia with an initial stagnation temperature T_0 of approximately 430 K.

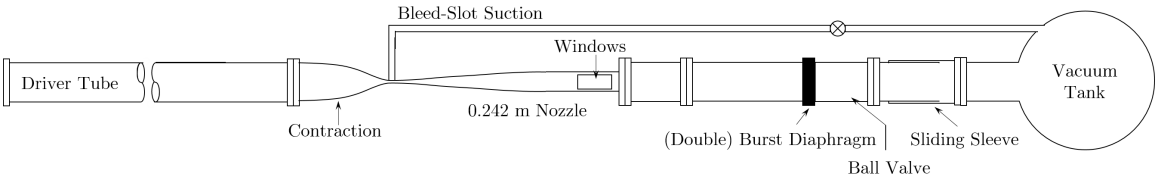

Figure 2.1. A schematic of the Boeing/AFOSR Mach-6 Quiet Tunnel.

The BAM6QT has several design features which keep the boundary layer laminar on the nozzle walls and decrease tunnel noise. The nozzle is polished to a mirror finish, which reduces the chance of roughness-induced transition in the boundary layer. The air passes through four stages of filters to remove particulates from the flow. The divergent part of the nozzle is very long to reduce the growth of the Görtler instability. Also, the turbulent boundary layer is removed through a bleed slot just upstream of the throat, enabling a fresh laminar boundary layer to form downstream. In this configuration, the BAM6QT experiences freestream noise levels on the order of 0.01% [54]. At high enough Reynolds numbers, the boundary layer on the wall will transition to turbulence even with the bleed slots opened and quiet flow will not be achieved. Since 2010, the maximum quiet Reynolds number was about 12.7×10^6/m, but this number was reduced to approximately 9.5×10^6/m when the contraction was opened for an o-ring replacement in December 2016. In May of 2018, the maximum quiet Reynolds number had increased to about 11×10^6/m. The Reynolds number is calculated using the method described in Section 2.3. If the bleed slot at the throat is not used, the boundary layer on the contraction is not removed. In this case, the BAM6QT can be run as a conventional tunnel with noise levels near 3% [54]. Additionally, since a turbulent boundary layer is thicker than its laminar counterpart, the effective nozzle area decreases and the Mach number is reduced to 5.8. Run times are also longer when the bleed valve is not opened.

The BAM6QT is unique even among quiet tunnels because there is the option for windows to be placed in the last section of the nozzle for optical access. A rectangular

7-inch by 14-inch Plexiglas window offers the largest field of view, but is rated to stagnation pressures of only 170 psia. An insert containing two porthole windows 5 inches in diameter provides a more limited field of view, but is safe for pressures up to 260 psia. Finally, a steel blank can be used, which does not provide optical access but is rated above the tunnel's maximum pressure of 300 psia. Although optical access was not required for imaging any models during tunnel runs for the present experiments, the windows provide a quick method of ensuring the tape used to affix wires is secure, observing probe vibration, and checking sensor placement between or during runs.

The BAM6QT is typically run with air as the test gas. When helium was used in place of air, the valve at the upstream end of the driver tube that normally supplies compressed air must be closed. The helium tank can then be attached to a regulator for filling the driver tube. Using helium is a two-person job, as the person who fills the tunnel cannot also monitor the helium at the upstream end of the driver tube. The second person may need to replace an empty tank with a new one. Before filling, the tunnel must first be drawn to vacuum so the air is removed. Then, the tunnel can be filled manually as usual, with the exception of possible helium tank replacements performed by the second person. Details of the instructions for running the tank using helium can be found in Reference [56].

2.2 Instrumentation

2.2.1 Pitot Probes and Traverse

Pressure measurements were made using a Kulite pressure transducer installed in the pitot probe shown in Figure 2.2. A double wedge composes the vertical part of each probe that is inside the tunnel to minimize blockage, and three support rods feed through the traverse bar. Each probe can traverse approximately 4.5 inches vertically. The diameter of the test section is not constant, because it is part of the diverging nozzle, but it is approximately 9.5 inches. Consequently, two probes of

different double-wedge lengths are required to measure the full vertical range. Radial positions are measured from the centerline ($y = 0$ in.), with positive values denoting locations above $y = 0$ in. There are probes that extend farther upstream to collect data at locations closer to the throat, but for the experiments presented here the only probe used is the one shown in Figure 2.2. This probe is typically used for the upper half of the tunnel but can also measure locations as low as one inch below the centerline. A complete radial span was not needed for these experiments, so this was the only probe necessary.

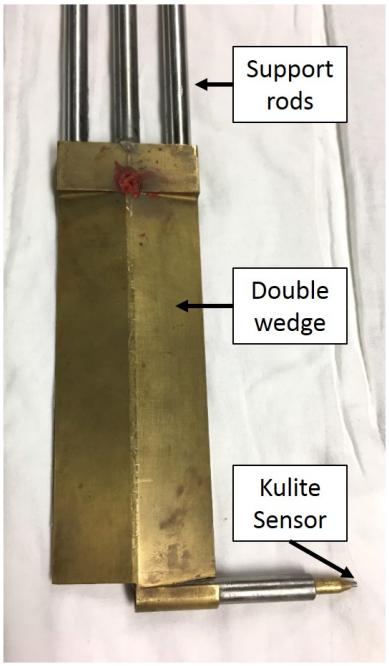

Figure 2.2. The pitot probe used for taking pressure measurements.

The pitot probes are held in place by a traverse mechanism which allows the probe to be positioned at a desired location. Once installed, the probe was moved to the approximate location of the centerline. A 6-inch ruler with precision of $1/64^{th}$ in. (0.40 mm) was used to measure the distance from both the upper and lower inner nozzle walls to the center of the back of the sensor. The probe was then adjusted until the sensor was positioned at $y = 0$ in. Figure 2.3 shows the traverse system with a pitot probe installed in the tunnel. There is an upper and a lower part of the traverse.

The upper part supports the motor and the rail positioner. Two metal plates are on the positioner to clamp on the three support rods of a pitot probe. These plates can be moved using the motor and the electronic controller, and since the plates hold the probe, this traverses the probes vertically. Details about the electronic controller system can be found in Appendix B. The probe can also be moved vertically by sliding the support rods through the traverse bar manually between runs.

The lower part of the traverse contains two rails that run parallel to the tunnel centerline which allows approximately 9 inches of movement in the axial direction. A ball screw can be turned by hand to slide the upper part of the traverse along the rails via linear bearings. Axial locations are measured in inches downstream of the throat. A scale is attached to the front of the traverse that provides an axial position relative to the traverse support struts with a precision of 0.5 mm.

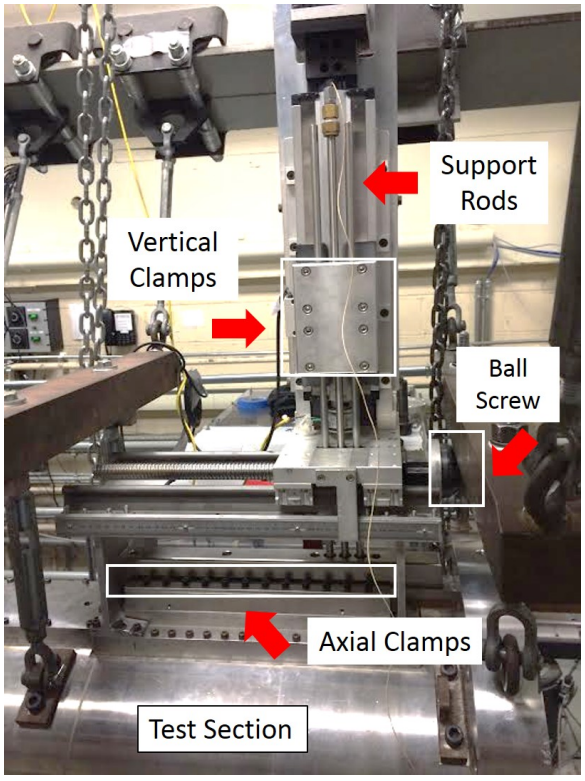

Figure 2.3. The traverse and probe support mechanisms with a pitot probe installed.

2.2.2 Kulite Pressure Transducers

Three models of Kulite pressure transducers were used for these experiments: XCE-062-15A, XTEL-190-500A, and XCQ-062-15A. The specifics of each model are described in detail below. Each 0.066-inch diameter sensor consists of a Wheatstone bridge on a silicon diaphragm, which deforms due to the pressure differential across the diaphragm. The Wheatstone bridge is made of strain gage elements and the resistance changes according to the pressure value. A linear correlation exists between the output voltage and the pressure. Each sensor is calibrated at least once per entry using the pressure measured from a Paroscientific Inc. Model 740 Digiquartz Portable Standard pressure gage and the mean Kulite voltage. The calibration procedures are described below with the details of each type of Kulite.

Each Kulite has one of two screens on the face of the sensor protecting the diaphragm. The A screen consists of one centered hole 0.040 inches in diameter, and the B screen has eight 0.006-inch diameter holes arranged in a circle near the outside of the face. Figure 2.4 shows a close-up view of the two different screens. Each Kulite sensor has a resonance at a frequency around 300 kHz. A-screen Kulites have a flat frequency response up to 30-40% of resonance, while B-screen Kulites have frequency responses that roll off at about 20% of resonance [57]. Although the A-screen option has a higher frequency response, it does not provide as much protection from particulates as the B-screen. For pitot probes, B-screen Kulites are used whenever they are available to reduce the risk of particulate damage. For two entries, A-screen Kulites were used. No significant differences were seen in the signals corresponding to the different screens. Steen observed unusual bursts in the A-screen signal that were not present in the B-screen signal [54]. However, those were only observed when the probe was within two inches of the lower nozzle wall and after four seconds into a run. For the present measurements, the probe was never placed at this location and data from times after four seconds were not used.

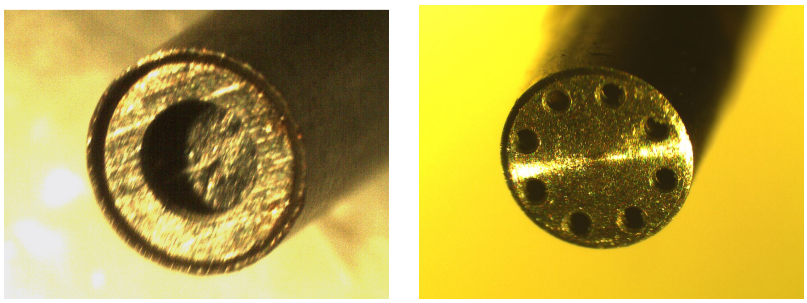

(a) A-screen (b) B-screen

Figure 2.4. Closeup images of the two Kulite screen options. Both are model XCE-062-15A sensors with diameters of 0.066 in.

The Kulite signal was passed through a conditioning box made in-house that also powers the sensor [54]. There are two low-noise outputs from the box, the DC signal and the AC signal. The DC signal is the sensor output amplified by a factor of 100. The AC output is high-pass filtered at 840 Hz and amplified by an additional factor of 100, for a total gain of 10,000. Data are collected using Tektronix DPO7054 digital oscilloscopes in Hi-Res mode and the Kulite signals were either DC or AC coupled. The mean pressure is the result of taking the DC output from the conditioning box and using the DC coupling option on the scope. The pressure fluctuations for noisy flow are found using the DC output from the conditioning box and the AC coupling scope option. The pressure fluctuations for quiet flow are much smaller, so the amplified AC output from the Kulite is used along with the AC coupling.

To make each pitot probe, a Kulite XCE-062-15A sensor was super-glued into the sleeve at the support so that the face of the sensor is flush with the nose. Typically a B screen was used to provide more protection from particulates in the flow. The same exact sensor was not always used for each entry, but the model was identical. The sensors used for pitot probes can be pressurized to about 300 psia without suffering damage but are mechanically stopped above 15 psia. The Kulite is calibrated in the sub-atmospheric range of expected pitot pressures at least once each week of testing. The ball valve is first opened to bring the driver tube down towards vacuum.

When the Paroscientific pressure gage reads a steady value (typically after a couple of minutes) the oscilloscopes are triggered and the mean voltage is recorded along with the Paroscientific pressure value. The ball valve can then be opened to further decrease the pressure in the driver tube, or the tunnel can be filled to increase the pressure. This process is repeated until at least 8 data points are collected which are in the range of the pitot signal. Figure 2.5(a) shows an example calibration for a pitot-probe Kulite.

There are two Kulites installed in the BAM6QT that are used for tunnel operation and to measure run parameters. The first is a model XTEL-190-500A Kulite flush-mounted to the tunnel wall in the beginning of the contraction section. The Mach number at this location is about 0.003 [54], so the pressure measured by this sensor is assumed to be the stagnation pressure at any point during the run. This Kulite model measures pressures up to 500 psia, well above the operating range of the BAM6QT. It was calibrated using the same method as the Kulites in the pitot probe, but instead of bringing the tunnel down to vacuum the data points were taken at approximately 15 psia intervals as the tunnel was pressurizing. For each entry, data over the relevant range of initial stagnation pressures were measured for the calibration. A sample calibration for the contraction Kulite is shown in Figure 2.5(b). The second sensor permanently installed in the tunnel is an XCQ-062-15A Kulite located in the diffuser section. This is the older version of the same type of sensors used to make pitot probes. It is mechanically stopped at 15 psia, and since it is located in a section of the tunnel that is pressurized before a run, it outputs a constant voltage of about 12V. When the diaphragms burst, the static pressure drops almost immediately as the expansion wave passes over the Kulite. The sudden drop in the sensor voltage triggers the oscilloscopes to begin collecting data. For a quiet run this also activates the fast valve for the bleed slots.

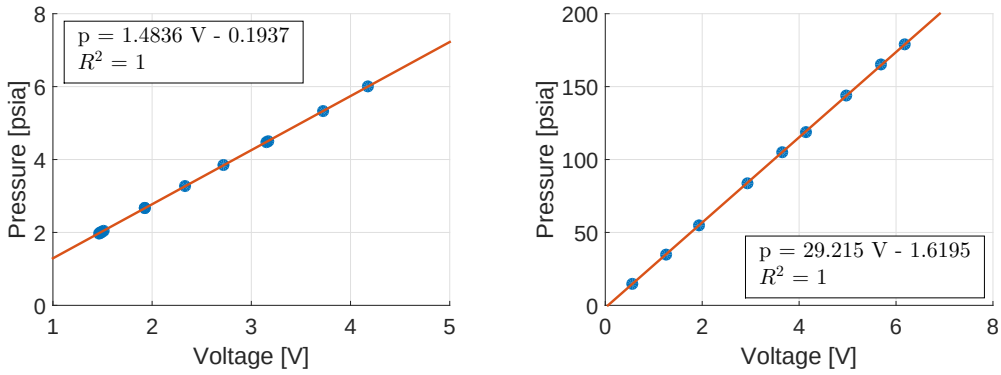

(a) Pitot-probe Kulite

(b) Contraction Kulite

Figure 2.5. Sample sensor calibrations. The blue circles are measured data, the red lines are the resulting calibrations.

2.2.3 Pitot Sleeves

Sleeves were used to vary the forward-facing diameter (D_f) of the pitot probes for a series of experiments performed to investigate effects of probe geometry on the measured pressure fluctuations. This work follows that done by Sweeney, who designed and tested three pitot sleeves [55]. The sleeves were designed to fit over a Kulite sensor that was already installed in a pitot probe. The smallest-diameter sleeve required a significantly different geometry than the other two, which may have affected his results. A new sleeve for the smallest forward-facing diameter was designed to have a geometry more similar to the larger two sleeves. This sleeve and the two larger sleeves designed by Sweeney were used for the present experiments. They each consist of a 0.040 in. long cylindrical section, a circular cone section with some half-angle, and a cylindrical support section 0.22 in. long which contains four set screws used to secure the sleeve on the probe support. Table 2.1 lists the dimensions of each sleeve and Figure 2.6 shows the hardware. The sleeve length is the total sleeve length, including the two cylindrical sections and the cone section. For the no-sleeve case, the base diameter refers to the diameter of the probe support, which is the stainless steel rod shown on the right of Figure 2.6(a). Although the base diameter

and half angle vary, the most significant difference is assumed to be the forward-facing diameter. Note that the brass sleeve used in the no-sleeve case is much smaller than the three sleeves used to adjust the forward-facing diameters, which cover the brass sleeve completely and fit over the stainless steel rod. Detailed drawings of all three sleeves used for these measurements are included in the appendix.

Table 2.1. Dimensions of probe geometries with and without sleeves.

Geometry	D_f	Base Diameter	Sleeve Length	Sleeve Angle
No Sleeve	0.066 in	0.315 in	n/a	n/a
Small Sleeve	0.118 in	0.6 in	2.25 in	6.9°
Medium Sleeve	0.236 in	0.564 in	2.25 in	4.7°
Large Sleeve	0.283 in	0.564 in	2.5 in	3.6°

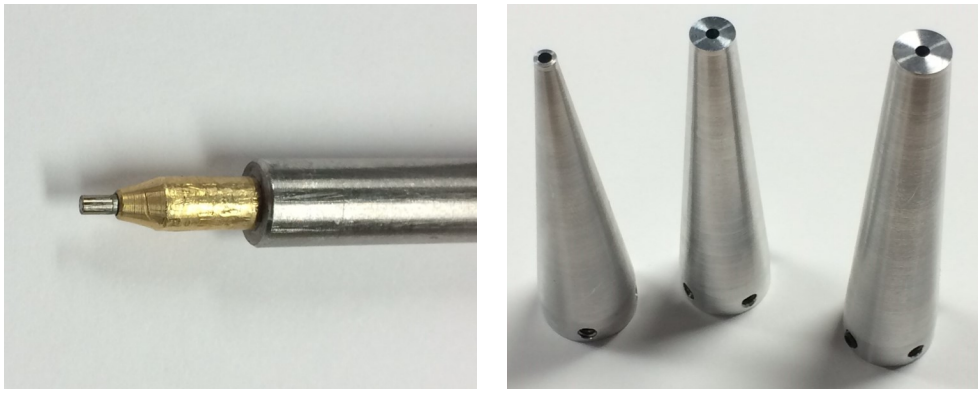

(a) The no-sleeve configuration.

(b) The sleeves used to modify the forward-facing diameter.

Figure 2.6. Photographs of the probe geometries used for current experiments.

The design used by Sweeney was necessary to ensure the sleeve fit over the Kulite and the brass piece that holds the sensor without severely increasing the diameter of the base of the sleeve. In order to use the new smallest-diameter sleeve the Kulite must be glued directly in the sleeve before attaching the sleeve to the probe, as

opposed to being installed in the probe and then sliding the sleeve over the sensor. Unfortunately, the base diameters of all three sleeves are larger than the slot on the top of the tunnel, and the sleeved pitot probe cannot be lowered into place. Therefore the sensor cannot be installed in the probe before the probe is installed in the tunnel.

This problem was solved by cutting the Kulite cable approximately 8 inches from the sensor. A Kulite cable consists of six smaller internal wires surrounded by a white casing. Of the six internal wires, four are necessary to power and use the sensor. Small pin-and-socket connectors were soldered onto each of the eight required wires. Figure 2.7 shows the wire with the soldered connectors in the probe support and in the no-sleeve hardware. The long portion of the wire was installed in the pitot probe support, which was placed in the tunnel. The sensor was glued into a sleeve and the Kulite wires were carefully fed though the tube at the base of the probe support. The sleeve was then secured on the probe using the set screws. Finally, the wires were connected and secured to the probe using high-temperature aluminum tape. When a new sleeve size was desired, the sleeve containing the Kulite was removed from the probe. The sensor was taken out of the sleeve using acetone and super-glued into the new sleeve, which could then be immediately secured to the pitot probe and the wires reattached.

2.2.4 Cone-Mounted Pitot Probe

A new pitot probe was designed to attach to the base of a cone (Figure 2.8(a)). The Kulite sensor is super-glued into place and the rod is held at a particular vertical location using set screws. The distance between the sensor and the cone can be adjusted. The cone used was the Edelman Modular Cone, which is a right, circular cone with a 7-degree half angle and a nominally sharp nosetip [58]. It was chosen because its angle-of-attack adapter is held in place by four bolts that screw into the base of the cone. The base of the cone-mounted pitot probe is mounted between the adapter and the cone using those same four bolts. For all experiments done with

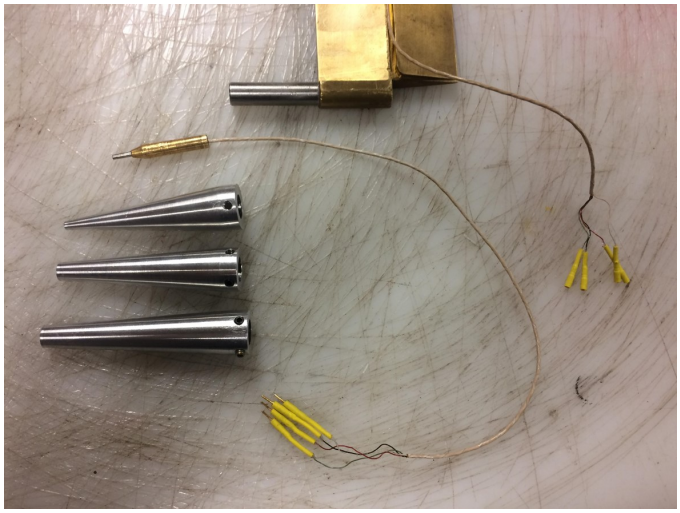

Figure 2.7. The cut Kulite wire with the pin and socket connectors. Sensor is installed in the no-sleeve configuration.

the cone-mounted pitot probe, the zero-degree adapter was used. The pitot probe is shown mounted to the cone in Figure 2.8(b).

The sensor face is perpendicular to the freestream flow, so the air inside the bow shock of the cone flows at an angle relative to the face of the sensor. However, Pope and Goin state on page 353 that pitot probes are insensitive to angle of attack up to 10° if the inner cavity diameter is at least 10% of the outer probe diameter [59]. For cavity-to-probe diameter ratios of 98%, the measurements are insensitive to angles of attack up to 15°. The sensing surface diameter used here is that of the Kulite, 0.066 inches, and the outer forward-facing diameter of the probe is 0.12 inches. The ratio of diameters is thus 55%, indicating that angles of attack up to 10° should not affect the measurements. Pope and Goin considered only traditional pitot probes measuring mean pitot pressures, rather than a sensor measuring pressure fluctuations. Nevertheless, it is assumed that the small angle of attack of the cone-mounted probe will not have a significant effect on the measurements.

(a) The cone-moutned pitot-probe hardware.

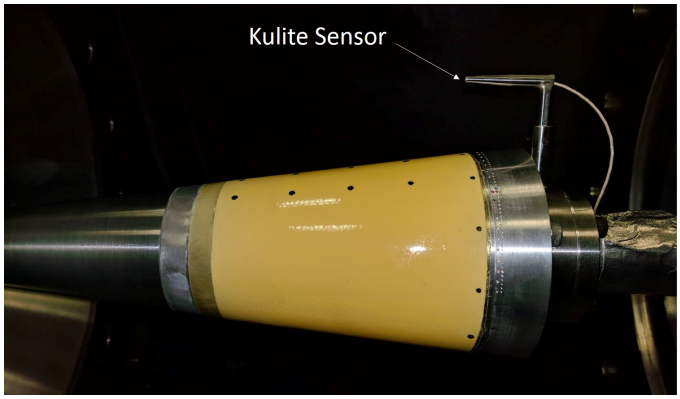

(b) The pitot probe attached to the base of the Edelman Modular Cone, which is mounted in the BAM6QT.

Figure 2.8. Photographs of the hardware used to measure noise levels at the aft end of a cone. Drawings are included in the appendix.

2.2.5 Hot Films

Flush-mounted surface hot films are used to measure the heat transfer on the nozzle wall. Unlike pitot probes, which are intrusive and generally cannot be used simultaneously with a model, the hot films are located on the nozzle wall out of the way of other experiments. They are kept at a constant temperature with a Bruhn-6 Constant Temperature Anemometer and indicate whether the boundary layer is laminar or turbulent. A turbulent boundary layer results in noisy flow in the freestream. Therefore, researchers can ensure a segment of data is taken during a period of quiet

flow by avoiding the large peaks in the hot-film signal that result from turbulent bursts.

For the majority of the entries performed for the present work, a Senflex multi-element hot-film array was installed near the end of the nozzle. Uncalibrated data from one hot film located at approximately $z = 74.5$ in. were used to qualitatively determine the state of the wall boundary layer. Typical traces for quiet flow conditions are shown in Figure 2.9(a). When a large model was used, heating streaks were observed on the lower portion of the model that were not seen on the upper portion [60]. It was determined that the high-temperature aluminum tape that was used to secure the lead wires for the array generated a disturbance that impinged on the model. Since the hot-film array was interfering with the flow, it was replaced with a single hot film. The new hot film was purchased from Dantec and was installed in October 2017. The 2.1 mm diameter sensor was flush-mounted to the nozzle-wall surface and is located at approximately $z = 73$ in. Figure 2.9(b) shows typical traces from the new hot film for quiet flow. Note that the new hot film is also uncalibrated, and also provides qualitative measurements only. The signals from the two hot films have different shapes but display the same characteristics. Each shows the approximately 0.3 seconds of tunnel startup, a few turbulent bursts, and unstart between $t = 4$ s and $t = 5$ s. The old hot film showed the increase in noise after two seconds more clearly. Nevertheless, the new hot film shows clear differences between quiet flow and turbulent bursts or fully turbulent flow. Further details about the new hot film can be found in Reference [61].

2.2.6 Heaters

The air that is used to fill the tunnel is heated to approximately 160°C by a circulation heater at the upstream end of the driver tube. The driver tube is heated and insulated with Fiberglass, and there are three band heaters installed on the contraction, upstream of the throat. These heaters maintain a temperature near

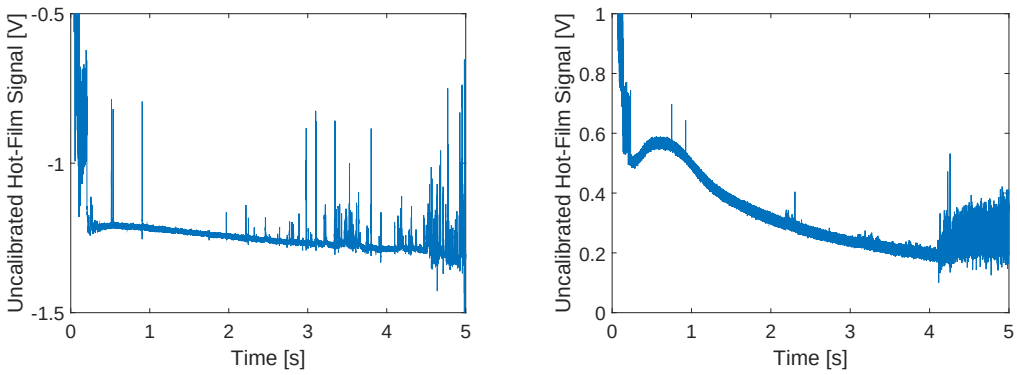

(a) The old hot film.

(b) The new hot film.

Figure 2.9. Typical hot-film traces for quiet flow conditions. Two different runs with $p_{0,i} = 130$ psia, bleeds open.

160°C and prevent liquefaction of the air in the expansion to Mach 6. Note that the contraction also utilizes Fiberglass insulation, while the nozzle expansion is not insulated.

Additionally, there are four band heaters on the nozzle expansion that were installed by Steen (Figure 2.10). Throughout this work, all discussion regarding changing the nozzle temperature refers to adjusting the setpoints of these four heaters. The locations of these heaters are given in Table 2.2. A thermocouple is positioned under each band heater to regulate the temperatures. In addition to those under the heaters, Steen installed 32 J-type thermocouples at various axial and azimuthal locations. The azimuthal locations, ϕ, are measured in four 90° increments as shown in Figure 2.11. These sensors are located on the outside of the nozzle so that they do not disturb the flow and are capable of measuring temperatures up to 1200°C. Four switches, each connected to 8 thermocouples, were mounted on a panel to display the temperatures. The switches can be turned to read the temperature measured by a particular thermocouple. Table 2.3 shows the locations of the sensors, which are accurate to approximately 0.5 in.

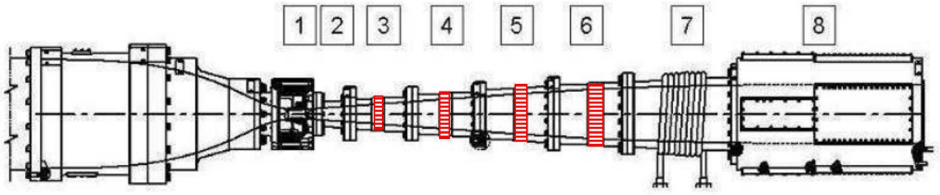

Figure 2.10. Schematic of BAM6QT nozzle with heater locations indicated by red stripes. Modified from Reference [52].

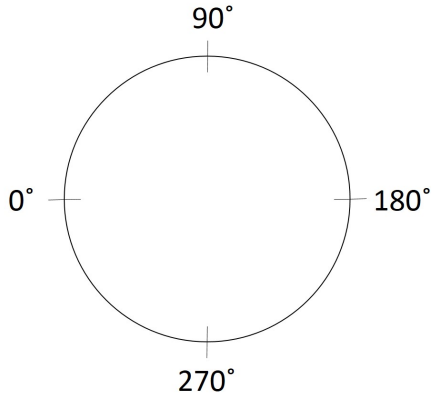

Figure 2.11. Azimuthal positions ϕ on the nozzle. Looking into the page corresponds to looking upstream.

Table 2.2. Locations of band heaters. Distance downstream of the throat, z, is measured to the center of the heater.

Heater	Nozzle Section	z [in]
1	3	12.5
2	4	23.5
3	5	35.5
4	6	47.5

2.3 Data Processing Methods

2.3.1 Run Conditions

The initial stagnation temperature is measured with a thermocouple at the upstream end of the driver tube. Once pressurized, the tunnel is allowed approximately

Table 2.3. Positions of the 32 thermocouples installed by Steen [54].

Thermocouple	z [in]	ϕ	Thermocouple	z [in]	ϕ.
1.1	6.5	180°	3.1	34.6	90°
1.2	9.4	180°	3.2	39.0	180°
1.3	11.9	90°	3.3	42.3	180°
1.4	16.2	180°	3.4	44.7	180°
1.5	16.2	90°	3.5	46.6	0°
1.6	16.2	0°	3.6	46.6	90°
1.7	16.2	270°	3.7	46.6	180°
1.8	18.5	180°	3.8	51.3	180°
2.1	21.1	180°	4.1	54.5	180°
2.2	22.9	90°	4.2	57.2	180°
2.3	27.3	180°	4.3	59.6	0°
2.4	30.5	180°	4.4	59.7	90°
2.5	32.4	180°	4.5	59.8	180°
2.6	34.6	0°	4.6	59.7	270°
2.7	34.6	270°	4.7	63.2	180°
2.8	34.6	180°	4.8	67.5	180°

ten minutes to equilibrate before running, after which uncertainties in the measurement due to temperature variations are assumed to be small. The pressure is also recorded prior to bursting the diaphragm, and the stagnation pressure during the run is measured by the contraction Kulite. These values are used in the isentropic relation in Equation 2.1 to calculate stagnation temperature (T_0) at a point during a run:

$$T_0(t) = T_{0,i} \left(\frac{p_0(t)}{p_{0,i}} \right)^{\frac{\gamma-1}{\gamma}} \tag{2.1}$$

where p_0 is the stagnation pressure during a run, $T_{0,i}$ and $p_{0,i}$ and are the initial stagnation temperature and pressure, and γ is the ratio of specific heats. The stagnation temperature and pressure are used to calculate the static temperature (T) and pressure (p) during the run using the isentropic relations,

$$p(t) = p_0(t)\left(1 + \frac{\gamma - 1}{2}M^2\right)^{\frac{\gamma-1}{\gamma}} \tag{2.2}$$

$$T(t) = \frac{T_0(t)}{1 + \frac{\gamma-1}{2}M^2} \tag{2.3}$$

where $M = 6.0$ for quiet flow and $M = 5.8$ for noisy flow. The unit Reynolds number Re is determined from the static pressure and temperature and is given by

$$Re(t) = \frac{p(t)M}{\nu(t)}\sqrt{\frac{\gamma}{RT(t)}} \tag{2.4}$$

where R is the ideal gas constant and viscosity ν is determined using Sutherland's law.

2.3.2 Mach Number

The pitot pressure measured by the Kulite sensor in a pitot probe is assumed to be the stagnation pressure behind a normal shock ($p_{0,2}$), and the freestream stagnation pressure ($p_{0,1}$) is the pressure measured by the contraction Kulite. These two pressures can be used to determined the Mach number during a run using the isentropic relation

$$\frac{p_0}{p} = \left(1 + \frac{\gamma - 1}{2}M^2\right)^{\frac{\gamma}{\gamma-1}} \tag{2.5}$$

and the normal-shock relations

$$\frac{p_2}{p_1} = 1 + \frac{2\gamma}{\gamma + 1}\left(M_1^2 - 1\right) \tag{2.6}$$

$$M_2^2 = \frac{2 + (\gamma - 1)M_1^2}{2\gamma M_1^2 - (\gamma - 1)} \tag{2.7}$$

where γ is the ratio of specific heats. The ratio $p_{0,2}/p_{0,1}$ can be expressed as

$$\frac{p_{0,2}}{p_{0,1}} = \frac{p_{0,2}}{p_1}\frac{p_1}{p_{0,1}} \tag{2.8}$$

where $p_1/p_{0,1}$ is given in Equation 2.5 and $p_{0,2}/p_1$ is determined by combining Equations 2.5, 2.6, and 2.7 to result in the Rayleigh pitot-tube formula for supersonic flow [62]. This formula expresses the ratio of post-shock stagnation pressure to freestream static pressure as a function of freestream Mach number only, and is given by:

$$\frac{p_{0,2}}{p_1} = \frac{p_{0,2}}{p_2}\frac{p_2}{p_1} = \left[\frac{(\gamma+1)^2 M_1^2}{4\gamma M_1^2 - 2(\gamma-1)}\right]^{\frac{\gamma}{\gamma-1}} \left[\frac{1-\gamma+2\gamma M_1^2}{\gamma+1}\right] \tag{2.9}$$

Using this formula in Equation 2.8 results in an equation for $p_{0,2}/p_{0,1}$ that is dependent only on Mach number:

$$\frac{p_{0,2}}{p_{0,1}} = \left[\frac{(\gamma+1)^2 M_1^2}{4\gamma M_1^2 - 2(\gamma-1)}\right]^{\frac{\gamma}{\gamma-1}} \left[\frac{1-\gamma+2\gamma M_1^2}{\gamma+1}\right] \left(1+\frac{\gamma-1}{2}M_1^2\right)^{\frac{-\gamma}{\gamma-1}} \tag{2.10}$$

However, Mach number cannot be expressed explicitly. Since both $p_{0,2}$ and $p_{0,1}$ can be experimentally measured, Equation 2.8 can be solved using an iterative approach.

2.3.3 Nozzle-Wall Boundary-Layer Displacement Thickness

If one-dimensional flow is assumed, the Mach number in a supersonic nozzle is solely dependent on the ratio of the inviscid cross-sectional area at some location in the nozzle to the cross-sectional area at the sonic point. This ratio, A/A*, can be determined from the Mach number with the equation [62]:

$$\left(\frac{A}{A^*}\right)^2 = \frac{1}{M^2}\left[\frac{2}{\gamma+1}\left(1+\frac{\gamma-1}{2}M^2\right)\right]^{\frac{\gamma+1}{\gamma-1}} \tag{2.11}$$

This one-dimensional assumption is not truly valid for the more complicated, three-dimensional flow in a wind tunnel. However, it does provide a simple method of estimating the boundary-layer displacement thickness (δ^*) using the Mach number. The area of the sonic point, A^*, is that of the throat and is constant. The inviscid area at another point along the nozzle is the area that is outside of the boundary layer. If R is the nozzle radius at some point and r is defined such that inviscid area

$A = \pi r^2$, then $\delta^* = R - r$. Thus, if the Mach number is known the area ratio A/A* can be found using Equation 2.11, and the displacement thickness is then:

$$\delta^* = R - \sqrt{\frac{A^* \times (A/A^*)}{\pi}} \tag{2.12}$$

The approximate boundary-layer displacement thickness is calculated to estimate whether a sensor is inside the nozzle-wall boundary layer. The radius at the nozzle exit is $R = 4.763$ in. and the sonic area for the BAM6QT is $A^* = 1.21$ in^2. For bleeds-open, laminar boundary-layer Mach-6 flow, Equations 2.11 and 2.12 yield $\delta^* \approx 0.237$ in.

2.3.4 Noise Level Calculation

Noise levels are traditionally measured as the root-mean-square (RMS) of the pitot-pressure fluctuations normalized by the mean pitot pressure. Different methods of computing the RMS pressure and varying bandwidths can result in different values for noise levels. Prior to Steen's Masters Thesis in 2010, BAM6QT noise levels were defined as the root-mean-square of the pitot-probe fluctuations normalized by the mean pitot pressure:

$$\%Noise = \frac{\sqrt{\overline{p'^2}}}{\bar{p}} \times 100 \tag{2.13}$$

where $p' = (p - \bar{p})$ denotes the pressure fluctuations from the mean pitot pressure $\bar{p}$. However, using this method with Kulite sensors can lead to inaccurately high noise levels due to the sensor resonance around 300 kHz if those higher frequencies are included. Instead, the noise levels are computed using the method presented by Steen which has an upper frequency limit of 50 kHz [54]. A brief comparison to other frequency intervals is included at the end of this section.

Data segments 0.1 seconds long were converted to pressure, the mean was subtracted from the signal to result in p', and the fluctuations were normalized by the mean pitot pressure. The power spectral density (PSD) of the normalized pressure fluctuations was then calculated using the MATLAB function `pwelch`. This function

uses Welch's method with a Hamming window, a 50% overlap, and a window size corresponding to a PSD frequency resolution of 2 kHz. The resulting PSD was then integrated over the range of nominally 0 to 50 kHz and the square root was taken to give the root-mean-square of the pressure fluctuations in this frequency band. Note that although the integration starts at $f = 0$ kHz, the AC signal that is used for quiet data is high-pass filtered at 840 Hz. Finally, the RMS was multiplied by 100 to yield the noise level as a percent of the mean pitot pressure. Figure 2.12 shows typical PSDs resulting from quiet and noisy flow taken with two different Kulites. The resonant frequency of each sensor differs but is clearly seen as the sharp peak near $f = 250$ kHz. This resonance is internal to the sensor and is a not a feature of the flow. The PSDs indicate the problem of inaccurately high noise levels that would result from integrating over a frequency range that contains the Kulite resonance.

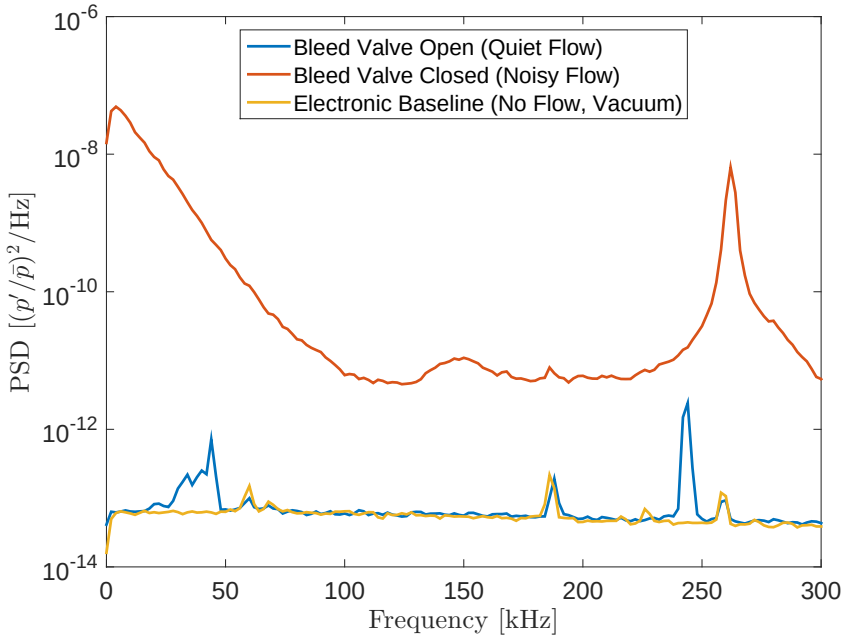

Figure 2.12. Typical power spectral densities used for integration to calculate noise levels for quiet and noisy traces. Probe is located at $z = 93$ in. and stagnation pressure is $p_0 = 125$ psia for both runs. Kulite resonance can be seen around $f = 250$ kHz for both sensors.

This method was used to calculate noise levels throughout this thesis. However, it is very sensitive to the range of frequencies over which the PSD is integrated. The 0 - 50 kHz bandwidth was chosen by Steen to avoid effects of sensor resonance and remain in the range of the Kulite's flat frequency response. The roll-off frequency is quoted as approximately one fifth of the resonant frequency, which Steen observed to be as low as 198 kHz. The range of 0 - 50 kHz is used to maintain consistency, and all BAM6QT noise levels since 2010 have been reported using this method and frequency range. When comparing noise levels to those of other tunnels or from measurements taken in the BAM6QT prior to Steen's work, it is important to keep in mind that the frequency interval used may differ. For example, these integration limits produce quiet-flow noise levels that are half the magnitude of those seen when integrating up to 500 kHz, which includes the resonance [63]. To further illustrate this dependence on the chosen range of frequencies, the PSD for quiet flow shown in Figure 2.12 was integrated to various upper frequency limits. The resulting noise levels are listed in Table 2.4. These values agree with the previous discovery, as integrating up to 500 kHz produced a noise level that is more than twice the noise level that resulted from integrating to 50 kHz. However, the noise levels do not change significantly for intervals that include frequencies above 50 kHz as long as the sensor resonance is not included.

Table 2.4. Calculated noise levels resulting from integrating the same PSD over various frequency intervals.

Frequency Interval [kHz]	Noise Level [%]
0 - 50	0.0082
0 - 100	0.0101
0 - 200	0.0128
0 - 300	0.0172
0 - 400	0.0181
0 - 500	0.0188

3. RESULTS AND DISCUSSION

3.1 Effects of Nozzle Temperature Distribution

The four nozzle band heaters described in Section 2.2.6 were used to determine whether modest changes in the temperature distribution along the nozzle had any effects on boundary layer stability and could increase the quiet pressure of the tunnel. The temperatures measured by the 32 thermocouples listed in Section 2.2.6 on the outside of the nozzle were recorded a few minutes prior to each run. The top of the nozzle has previously been found to be consistently hotter than the bottom [54]. This effect was also observed with the present experiments. Figure 3.1 shows the temperature along the nozzle at the four azimuthal positions. Axial position is measured as the distance from the throat. Recall that the nozzle is about 101 in. long. These values were taken before the first run of the day and none of the four band heaters were turned on. Note that regions of the nozzle where the $\phi = 180°$ thermocouples appear to measure the lowest temperature do not contain thermocouples at $\phi = 270°$ or at $\phi = 90°$. For every axial position that does contain 4 radial thermocouples, $\phi = 270°$ (the bottom of the nozzle) has the lowest temperature and $\phi = 90°$ (the top of the nozzle) the highest. The largest difference between the top and bottom wall temperatures is 10.7 °C and occurs 34.6 inches from the throat. The thermocouple at $\phi = 180°$ is located on the geographically northern wall of the nozzle and typically measures a temperature value between those on the top and bottom of the nozzle. For consistency, only thermocouples located at $\phi = 180°$ were used to describe the temperature distribution.

The four band heaters described in Section 2.2.6 were used to vary the temperature distribution along the nozzle. The first time the heaters were turned on, the heaters were allowed to heat the nozzle for over an hour before a run was performed. After

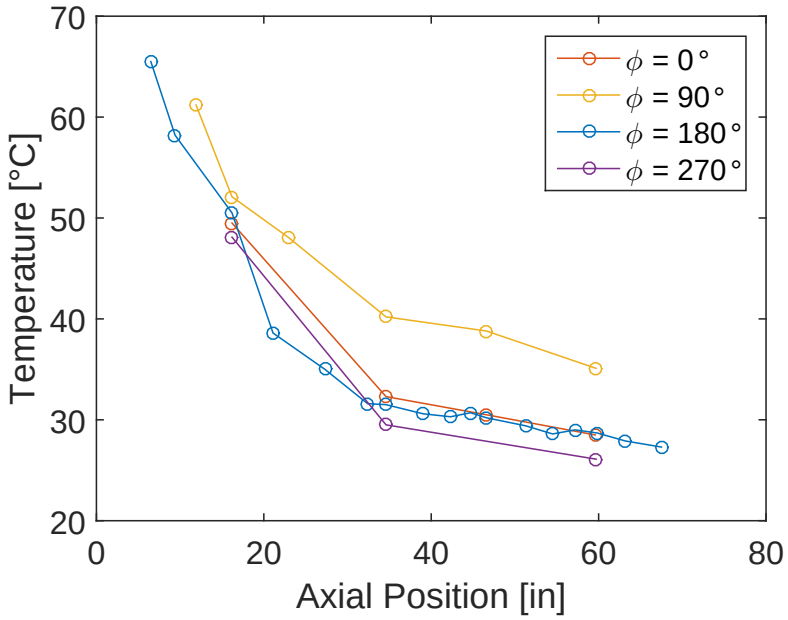

Figure 3.1. Temperatures measured by thermocouples on outer nozzle wall at all 4 radial positions. The heaters were not used. Recall that $\phi = 90°$ corresponds to the top of the nozzle, and $\phi = 270°$ corresponds to the bottom.

this period, the values measured by the thermocouples were steady and the nozzle was assumed to be in thermal equilibrium. If the temperature set point was changed (either raised or lowered) after a run, about an hour was allotted for the nozzle to reach equilibrium.

Each time the heaters were used a negative temperature gradient was implemented, meaning the temperature decreased with distance downstream of the throat. This distribution was based on conclusions such as those presented by Gasperas, Masad and Nayfeh, and Schneider that suggest a decreasing temperature may stabilize the flow [32, 33, 35]. The farthest-upstream heater had a maximum set point of 120°C to provide a safety buffer since the highest safe temperature for the nickel nozzle throat in the BAM6QT is around 150°C [64]. At temperatures above this, it is possible that the electroformed nickel could lose its hardness. The farthest-downstream heater had a maximum set point of 40°C, since the goal was to slowly

taper the heating until near room temperature. Figure 3.2 contains examples of temperature distributions measured along the north wall of the nozzle ($\phi = 180°$). Again, the axial position z is measured in inches downstream of the throat. Recall that there is no insulation on the nozzle expansion. The blue trace, with a maximum temperature of 61.4 °C, corresponds to measurements taken when the four band heaters were not used. The temperature drop-off is the natural result of the heating that is constantly applied to the contraction. The other three traces correspond to temperatures taken when additional heating was applied. The peak at about $z = 16$ in. occurs just downstream of the first nozzle heater, which is located at $z = 12.5$ in. Note that it appears artificially pronounced in this plot because data from thermocouples at azimuthal locations other than $\phi = 180°$ are not included. Figure 3.3 shows the temperatures for the run with $T_{max} = 107.2$°C at all azimuthal locations, and there is not as much of a drastic peak at $z = 16$ in. when data from all thermocouples are included. Also note that although the maximum temperature shown in Figure 3.2 is around 110 °C, some thermocouples which were at $\phi = 90°$ read higher values, as can be seen in Figure 3.3. Therefore the distributions shown in Figure 3.2 do not reflect the maximum temperatures along the nozzle, and T_{max} refers to the maximum temperature measured on the north wall ($\phi = 180°$).

A pitot probe was positioned on the centerline at $z = 93$ in. The stagnation pressures chosen for these measurements were between 170 psia, which was the maximum quiet pressure at the time, and 185 psia. Any effects on the maximum quiet pressure would be seen in runs with these initial stagnation pressures. In addition, there are a larger number of turbulent bursts at higher pressures. Therefore, the effects on the number of turbulent bursts can be more easily seen at higher pressures.

Figure 3.4 shows the hot film trace for a typical run with an initial stagnation pressure of 170 psia and no additional heating from the four band heaters. The spikes in the signal between $t = 2$ s and $t = 4$ s indicate turbulent bursts. For this initial stagnation pressure, quiet flow was almost always achieved by 0.5 seconds, and continued for roughly 4 seconds. However, the turbulent bursts increase in number

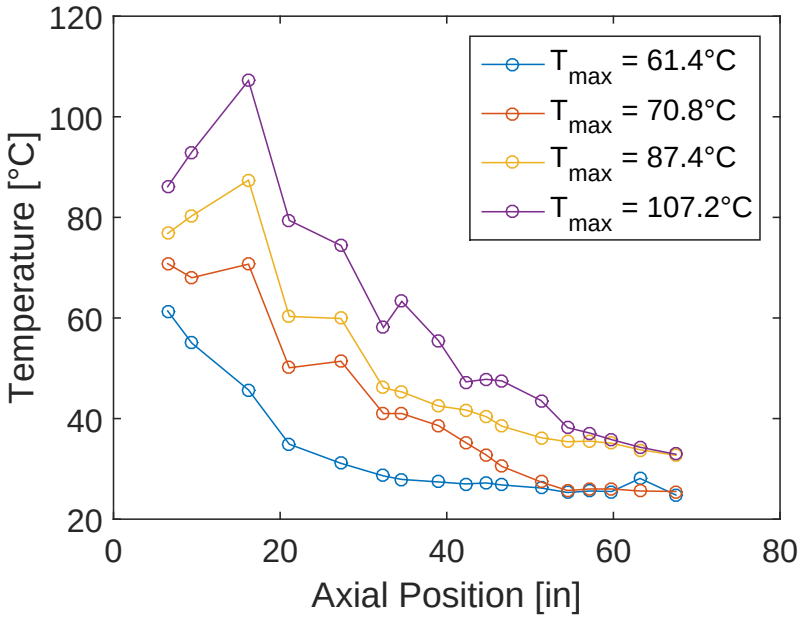

Figure 3.2. Example temperature distributions along the outside of the north side of the nozzle ($\phi = 180°$). No insulation was used, and the thermocouples were exposed to the air.

at approximately $t = 2$ s, as in Figure 3.4. The increased number of bursts is accompanied by a general increase in noise levels, a topic which is discussed in Section 3.2. As a result of tunnel start-up and this noise increase, data are typically analyzed between $t = 0.5$ s and $t = 2$ s. Therefore, the time period between $t = 0.5$ s and $t = 2$ s was considered for determining the fraction of time the flow was quiet, for all runs.

The standard deviation of the hot film fluctuations was used to determine whether or not the flow was quiet. The hot film (rather than the pitot pressure) was chosen as the standard for quiet flow because typical experiments performed in the BAM6QT do not include a pitot probe and therefore rely on the hot film for determination of quiet flow. Note that the hot film shows more turbulent bursts than the pitot probe, as will be shown at the end of this section. The standard deviation for a hot film trace of quiet flow resulting from $p_{0,i} = 170$ psia for these experiments is approximately

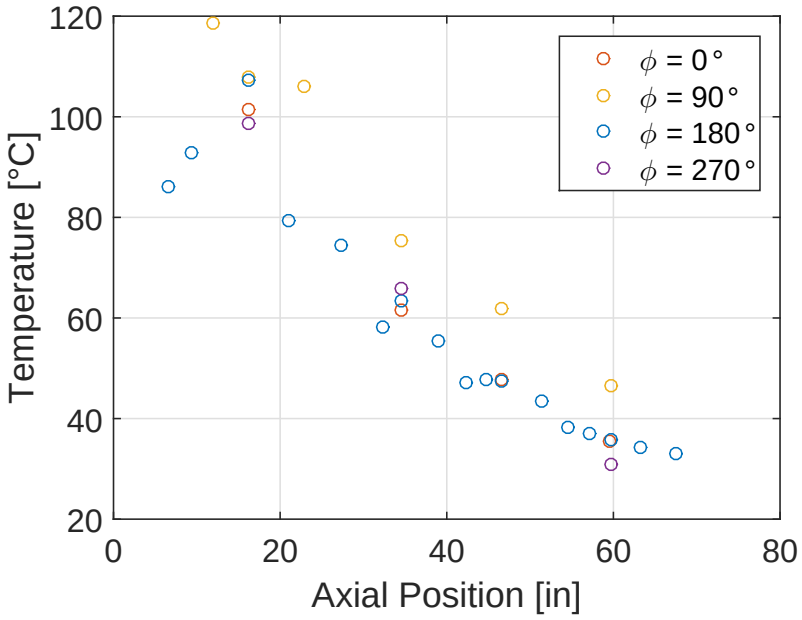

Figure 3.3. The temperatures from each thermocouple for the run with the highest heating in Figure 3.2

.

0.004 V. Since that value decreases for quiet flow with lower stagnation pressures, it was chosen as the cutoff value for determining if the flow was quiet. The hot film signal was broken into time periods of 0.005 seconds (because turbulent bursts typically last for about 0.005 seconds) and time periods for which the hot film signal standard deviation was less than or equal to 0.004 V were considered to contain quiet flow. An example trace is shown in Figure 3.5. The hot film signal is first plotted in blue, and the red trace, which indicates that the standard deviation was less than or equal to 0.004 V, is plotted on top of the original signal. It can be seen that the algorithm successfully determines periods of quiet flow. However, because the hot film is uncalibrated, it may not be the case that this particular algorithm will be successful for other tests. This method should not be considered the standard for determining quiet flow as the standard deviation of the quiet-flow hot-film signal may vary between entries.

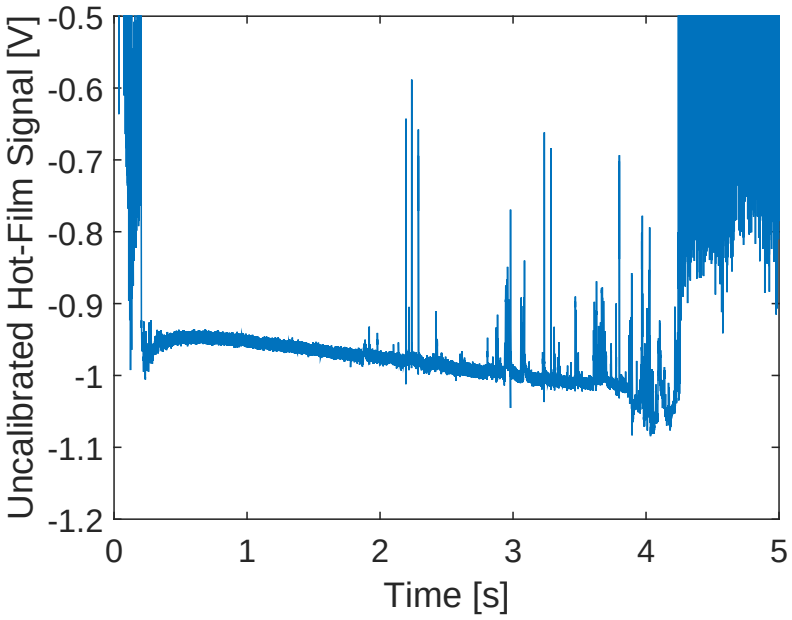

Figure 3.4. Time trace of the uncalibrated hot film during a run with $p_{0,i} = 170$ psia. Spikes in the signal indicate turbulent bursts.

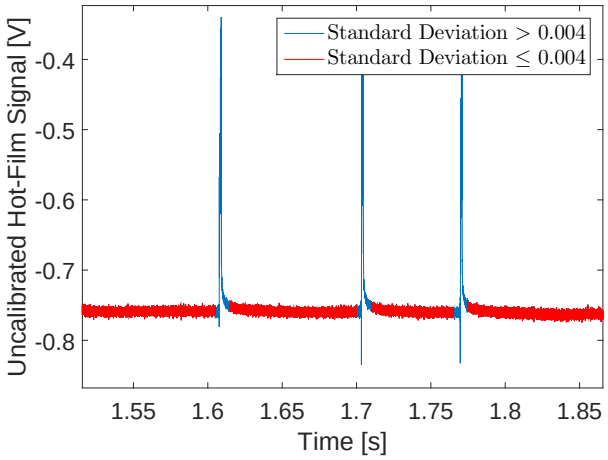

Figure 3.5. Part of a hot-film trace from a run with $p_{0,i} = 170$ psia. The red segments indicate 0.005-second periods during which the standard deviation of the fluctuations is less than or equal to 0.004 V.

Figure 3.6 is a plot of the percentage of quiet time against the maximum temperature measured by the $\phi = 180°$ thermocouples. Each data point represents a different

run. For the present analysis, the percentage of a run which is quiet refers to the percentage of time between $t = 0.5$ s and $t = 2$ s which has a standard deviation less than or equal to 0.004 V. When considering this figure, it is important to remember that the maximum quiet pressure with no additional heating was 170 psia. Higher initial pressures will have longer portions of time that are above this value and are therefore expected to have a smaller percentage of quiet time. To account for this, Figure 3.6 also contains dashed lines that indicate the average percentage of time that contains stagnation pressures below 170 psia when the initial stagnation pressure was either 180 or 185 psia. No line is shown for $p_{0,i} = 170$ psia because in that case the entire run is below the maximum stagnation pressure.

The runs with $p_{0,i} = 170$ psia generally contain quiet flow for more than 97% of the run between $t = 0.5$ s and $t = 2$ s. This is expected, since that time period was chosen because it contains mostly quiet flow if $p_{0,i}$ is less than the maximum quiet pressure of 170 psia. Smaller percentages of quiet time indicate an increase in turbulent bursts. Also expected is the trend of increasing stagnation pressure experiencing decreased percentages of quiet flow time. Even when the initial stagnation pressure was as high as 185 psia, the flow typically did not become quiet until p_0 dropped below 170 psia. Furthermore, no relationship between the heating and the amount of quiet flow is evident. The scatter for the initial stagnation pressures is likely due to inherent randomness, and there is no apparent correlation between temperature distribution and percentage of quiet flow.

As mentioned above, periods of the run before $p_0 = 170$ psia is reached typically experience noisy flow. Figure 3.7 shows the hot-film trace for a run with $p_{0,i} = 185$ psia. The first second of runtime contains noisy flow, as the stagnation pressure does not drop below 170 psia until about a second into the run. There is also an overall increase in the number of turbulent bursts compared to those seen in the hot film trace for the $p_{0,i} = 170$ psia run shown in Figure 3.4. Both of these factors contribute to the decrease in the percent of time for which the flow is quiet.

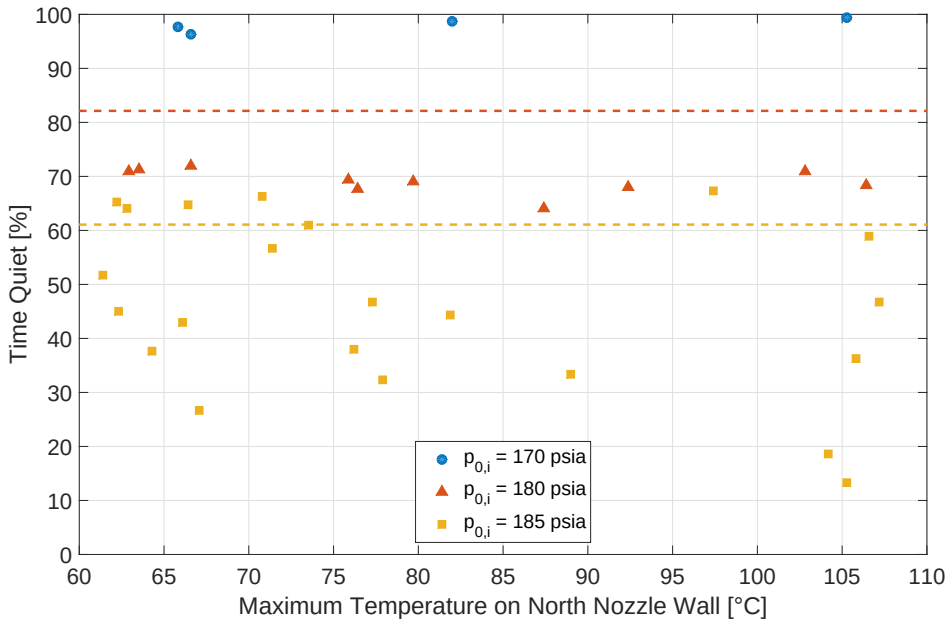

Figure 3.6. Percentage of run time between $t = 0.5$ s and $t = 2$ s that was quiet verses the maximum measured temperature. Dashed lines indicate the average percentage of runtime with $p_{0,i} \leq 170$ psia.

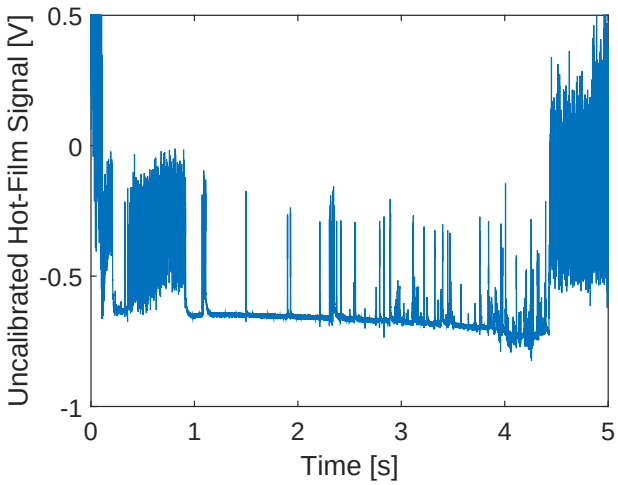

Figure 3.7. Uncalibrated hot-film signal for a run with $p_{0,i} = 185$ psia.

However, the number of turbulent bursts that occur in a run is largely random and could be adding additional scatter to the results presented in Figure 3.6. In

order to determine if heating has an effect on the maximum quiet pressure, the first (and therefore highest) pressure for each run that corresponded to quiet flow is shown versus the maximum temperature on the nozzle in Figure 3.8. Runs with $p_{0,i} = 170$ psia are not shown, since the stagnation pressure was always below the maximum quiet pressure by the time tunnel startup ends. There is a slight trend of decreasing quiet pressure with increasing heating on the nozzle wall, but the significant scatter seen here as well is too large to conclusively correlate increased tunnel performance with less heating. Regardless of the nozzle-wall temperature, the average maximum quiet pressure for these runs is approximately 170 psia, which was what was previously reported by Sweeney [55].

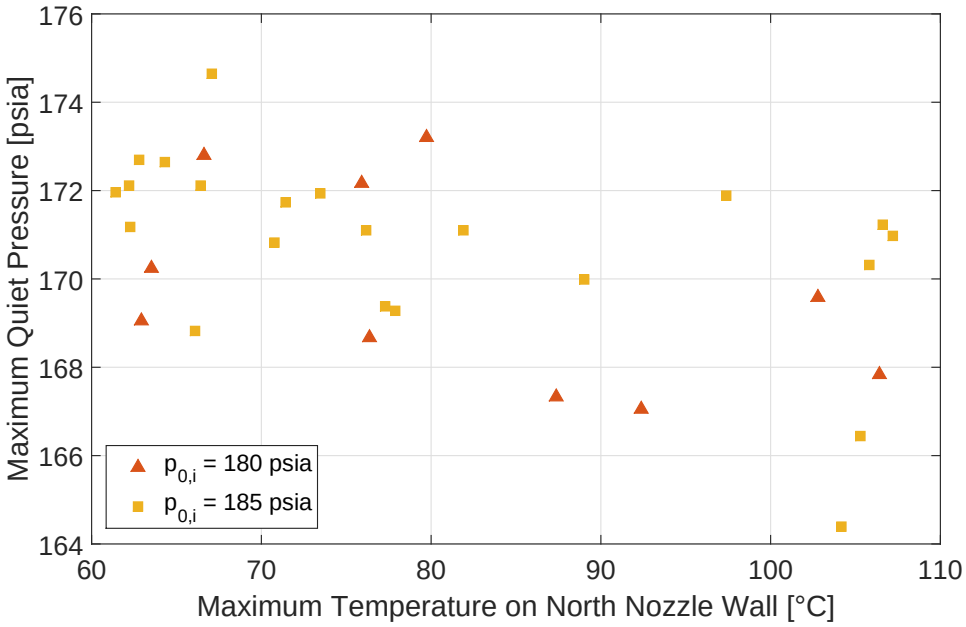

Figure 3.8. Stagnation pressure for which the flow first becomes quiet for runs with varying temperature distributions.

The amount of heating was limited by the maximum temperature of the nickel throat, and it is possible that higher temperatures would have had an effect on the boundary layer stability. The maximum temperature ratio used for these experiments was approximately $T_w/T_0 = 0.98$. Recall that the computations performed

by Gasperas that examined temperature distribution effects on the second-mode instability in a flat-plate boundary layer assumed a heated wall temperature ratio of $T_w/T_0 = 0.87$ [33]. The flow in the BAM6QT nozzle is significantly different, and the temperature ratios needed to see an effect on second-mode stability due to a temperature gradient is unknown. Additionally, the experiments performed by Stainback et al. utilized a uniformly-heated nozzle with a temperature ratio of $T_w/T_0 = 1.4$ [31]. This is a larger temperature ratio than could be achieved on the nozzle due to the limitations of the current throat. One reason for the fabrication of the new stainless steel throat is that it can stand higher temperatures. It is possible that the new throat would allow a range of temperatures that could be used to observe an increase in the maximum quiet pressure.

Even though the maximum quiet pressure is approximately 170 psia regardless of the heating used, a higher initial stagnation pressure yields a higher Reynolds number for a given stagnation pressure later in the run. This is because a higher $p_{0,i}$ results in a lower stagnation temperature once the stagnation pressure reaches the target value, and thus a higher Reynolds number compared to a run which starts at a lower $p_{0,i}$. For example, on average, the runs which have $p_{0,i} = 185$ psia reach $p_0 = 160$ psia and Re $= 13.1 \times 10^6$ /m at approximately two seconds into the run. This is about 4% higher than the Reynolds number that results from $p_{0,i} = 175$ and $p_0 = 160$, which is 12.6×10^6 /m. Therefore, running the tunnel with a $p_{0,i}$ above the maximum quiet pressure can result in slightly larger Reynolds numbers while still achieving small time periods of quiet flow. The increase is small but potentially useful for some applications.

Figure 3.7 shows that while a run may not contain a high percentage of time for which the flow is quiet, there are often time segments of at least 0.1 seconds that do have quiet flow. This is the typical length of time used by researchers in the BAM6QT to analyze data, so quiet segments at least that long are useful. Due to the random nature of the turbulent bursts, it is not possible to control exactly which stagnation pressure would exhibit quiet flow. Nevertheless, turbulent bursts appear in the hot-

film signal, which is collected by researchers who do not use pitot probes. The hot film can be used to avoid processing data for time periods that contain turbulent bursts. Figure 3.9 shows the lower-wall ($\phi = 270°$) hot-film signal plotted with the signal from a pitot probe on the centerline at $z = 93$ in. The pitot-probe signal is the raw voltage, which has been scaled down by a factor of 100 and offset by a constant value to allow visual comparison with the hot-film signal. All bursts that are in the pitot-probe signal also appear in the hot-film trace. Additionally, there is noise picked up by the hot film that is not in the pitot-probe signal. This suggests that the hot film is a sufficient measure of quiet flow, because all times that are quiet according to the hot film are also quiet according to the pitot probe. Thus, when models are used which do not contain a pitot probe, the hot film alone can be trusted to confidently ensure quiet flow in a desired time period. This is useful especially at high $p_{0,i}$ where there are many turbulent bursts. Note that these experiments were performed when the Senflex hot-film array was installed in the tunnel. A similar comparison between pitot-probe signals and traces from the new hot film should be performed to ensure the hot film remains a reliable way to determine quiet flow.

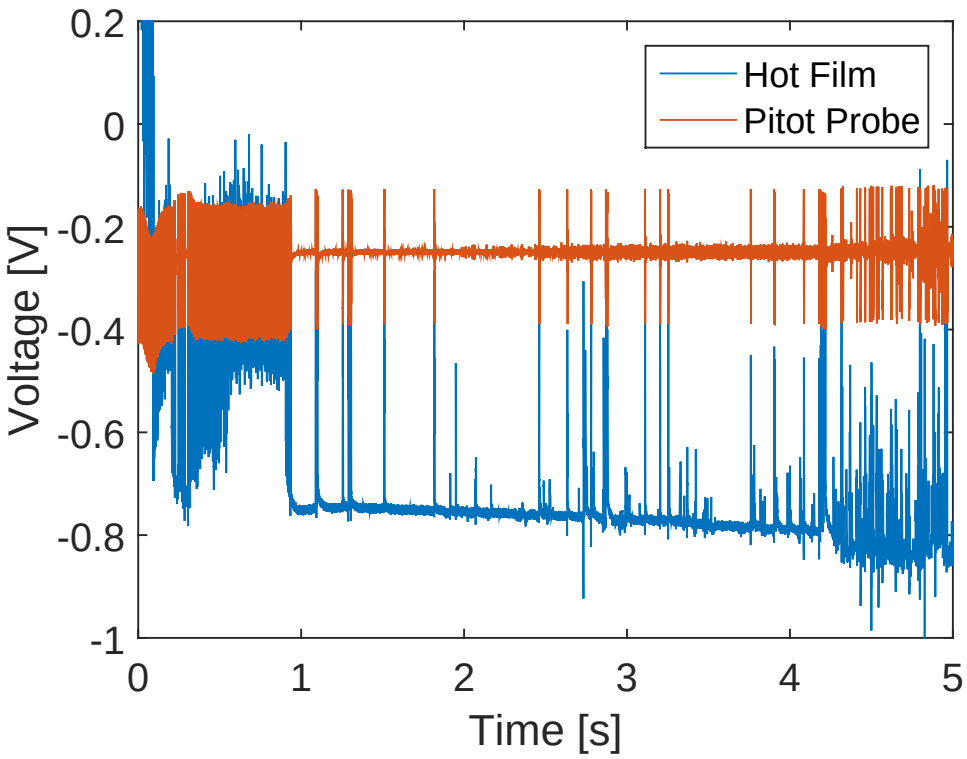

Figure 3.9. The uncalibrated Senflex hot-film array and pitot-probe signals for a run with $p_{0,i} = 185$ psia. Values are qualitative only.

3.2 Axial Dependence of Noise Levels

The noise increase that occurs during quiet runs after approximately 2 seconds of runtime is thought to result from free convection in the driver tube [51], but is still not well understood. It occurs while the freestream Reynolds number is decreasing, which is difficult to explain. Steen found that for data obtained on the centerline, the noise increase occurred consistently at $z = 93.6$ in. but not at $z = 84.9$ in., and that the magnitude of the increase was Reynolds-number dependent [54]. It is possible that the downstream portion of a model would experience an increase in pressure fluctuations near the end of a run. Additionally, the increase in fluctuations may not be present on upstream regions of the model. Experiments were performed for the present work to better determine the precise location which first experiences the noise increase and to quantify the magnitude of the increase.

The same B-screen Kulite and pitot probe that were used for the experiments described in the previous section were used for these measurements. The sensor was positioned on the centerline for all runs, and the axial location was adjusted between runs to span a variety of streamwise locations. Because Steen did not see an increase in noise levels at $z = 84.9$ in, the farthest upstream position measured for this analysis was $z = 84.25$ in. This is also the upstream limit of the particular probe, and the downstream limit is $z = 93$ in. Three initial stagnation pressures were used: $p_{0,i} = 170$ psia, $p_{0,i} = 130$ psia, and $p_{0,i} = 90$ psia. However, due to time constraints there were only two runs made at the highest initial stagnation pressure. Unfortunately, before further experiments at this pressure could be performed, the tunnel was opened to replace an o-ring and the maximum quiet pressure dropped to 135 psia. Thus, the $p_{0,i} = 170$ psia data set is incomplete. However, measurements were previously taken at $z = 93$ in. for the experiments discussed in Section 3.1 for which no additional heating was used and $p_{0,i} = 170$ psia. Therefore, although these measurements were made several months prior to the rest of the data presented in this section, the conditions were similar. These data are included in this analysis to allow

comparisons between upstream and downstream locations for the highest-pressure conditions.

Figures 3.10 through 3.12 show the noise levels calculated for time periods of 0.1 seconds throughout several runs at various axial locations. Measurements were made at additional positions for the lower two initial stagnation pressures but are not all included in the plot so that trends can be observed without cluttering the figure. There is an increase in the noise level seen in the $p_{0,i} = 90$ psia case for $z \geq 87$ in. The disturbance increase starts at $t = 2.5$ s. For the $p_{0,i} = 130$ psia case, the increase happens slightly earlier in the run and is much greater in magnitude. Note that all noise levels are still well within the quiet limit of about 0.05% [22]. Large increases in noise begin at a similar axial location of $z = 87$ in. The furthest upstream distance tested, $z = 85$ in., also shows a slight increase in noise level by the end of the run, but not nearly to the extent of the $z = 89$ in. or $z = 91$ in. case. Both the 90 psia and the 130 psia initial stagnation pressure measurements indicate noise levels that generally increase downstream. For $p_{0,i} = 170$ psia, there is a clear increase in noise levels at $z = 93$ in compared to $z = 85$ in. The downstream measurement was taken during an earlier tunnel entry with the same probe and sensor due to the limited dataset, as described above.

Figure 3.13 summarizes the results from runs at all probe positions. Each point represents one run. The y axis is the difference in noise level between the flow at $t = 0.5$ s and at $t = 3.6$ s expressed as a percentage of the noise level at $t = 0.5$ s. These times were chosen to maintain consistency between runs, and each run experienced tunnel start up by $t = 0.5$ s and lasted until at least $t = 3.6$ s. Some runs at locations farther upstream experienced a decrease in pressure fluctuations. This effect has not been shown to be repeatable and is likely random. The Reynolds number dependence is clear in this figure. For initial pressures of 90 psia, noise levels did not increase significantly at locations further upstream than $z = 89$ in. At higher Reynolds numbers, when $p_{0,i} = 130$ psia, an increase occurred between $z = 87$ in. and $z = 88$ in. Downstream of $z = 88$ in., the $p_{0,i} = 130$ psia runs experienced

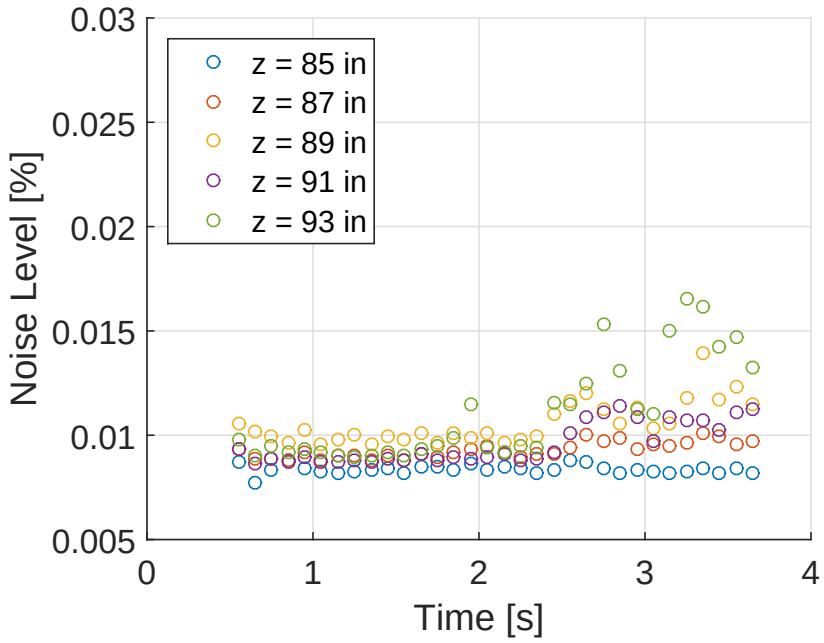

Figure 3.10. Noise levels when $p_{0,i} = 90$ psia. Probe on centerline.

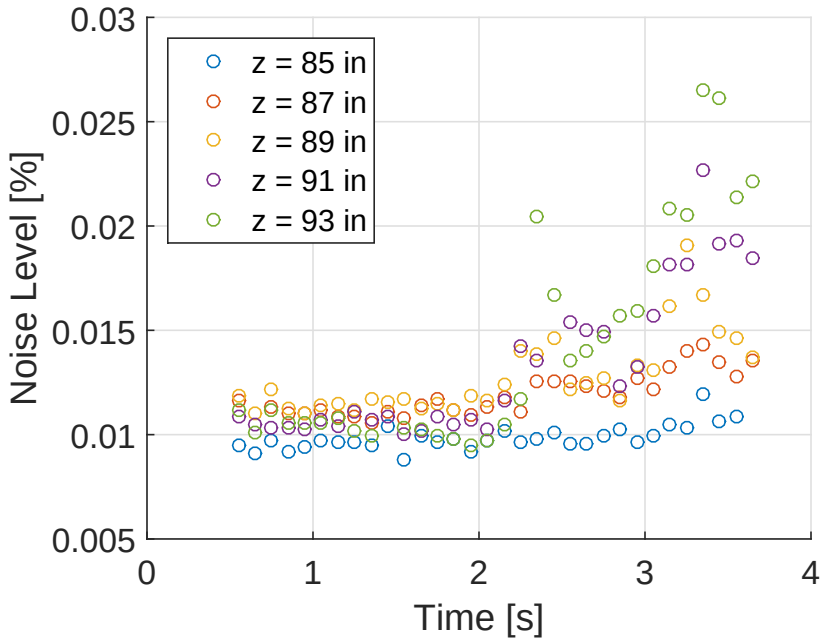

Figure 3.11. Noise levels when $p_{0,i} = 130$ psia. Probe on centerline.

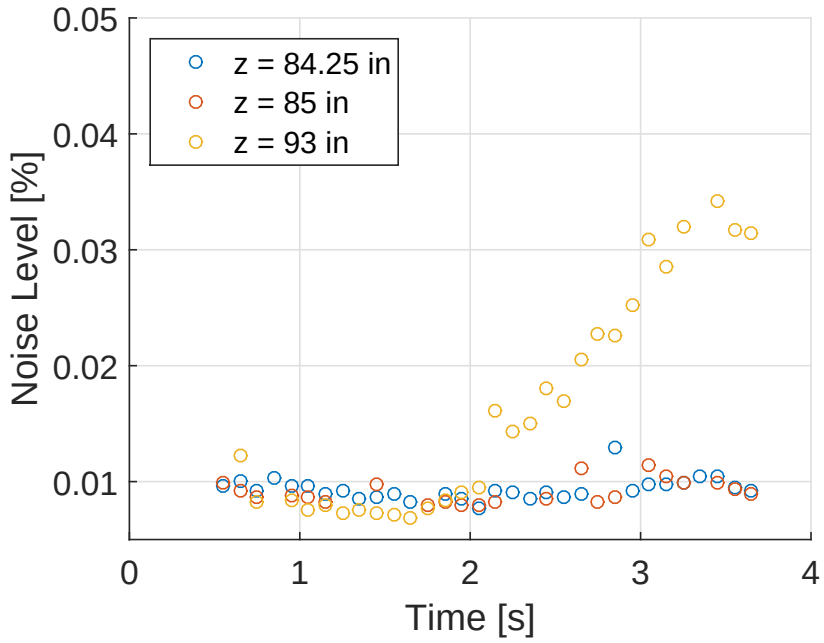

Figure 3.12. Noise levels when $p_{0,i} = 170$ psia. Probe on centerline.

increases in noise levels that were slightly larger than those of the $p_{0,i} = 90$ psia runs until $z = 90$ in. At this location, the Reynolds number effects are obvious. With the exception of $z = 92.5$ in., the increase is significantly larger for the higher pressure runs. The reason for the dip at $z = 92.5$ in. is unknown. The $p_{0,i} = 90$ psia runs had a maximum increase of 42% at $z = 92$ in, the $p_{0,i} = 130$ psia runs experienced noise increases up to 97%, and the maximum increase for the $p_{0,i} = 170$ psia runs was 157%. Note that although the maximum increase for the $p_{0,i} = 130$ psia runs and the $p_{0,i} = 170$ psia runs occurred at the farthest downstream location, this was not the case for the $p_{0,i} = 90$ psia runs. This has not been shown to be a consistent result. Recall that the change in the tunnel's maximum quiet pressure prevented additional quiet runs with $p_{0,i} = 170$ psia, so only three points are represented in Figure 3.13. Therefore, details of the trend cannot be ascertained from this set of measurements.

The noise increases begin at a similar time during the run as the contraction temperature fluctuations reported by Borg [51]. However, if the fluctuations were only

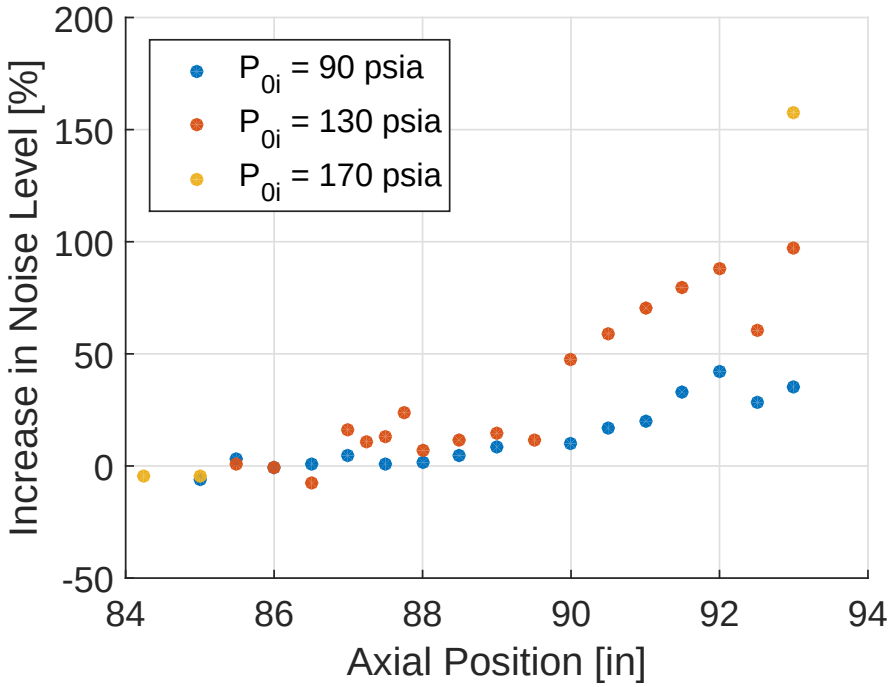

Figure 3.13. Increase in noise level at the end of a run ($t = 3.6$ s) as a percentage of the noise level at $t = 0.5$ s.

due to free convection in the contraction, the dependence on axial location would not be explained. Furthermore, this effect is not a result of amplified disturbances in the nozzle-wall boundary layer, since they increase later in the run when the Reynolds number is lower. Instead, it seems likely that the temperature fluctuations Borg measured are amplified in the nozzle-wall boundary layer. This would explain both why the increased noise levels are seen later in the run and why they occur at locations farther downstream from the nozzle.

Mach numbers calculated for the same time periods throughout the run that were used to find the noise levels are shown in Figures 3.14 through 3.16. The runs with $p_{0,i} = 90$ psia all display slightly decreasing Mach numbers during the run except for those farthest downstream. At $z = 93$ in. the Mach number decreases until about $t = 2.5$ s, at which point it increases. There is also, for the most part, a correlation between axial position and Mach number: locations farther downstream

typically have lower Mach numbers. The same trends are not seen when $p_{0,i} = 130$ psia. The farthest upstream position does experience a decreasing Mach number but there is not a clear correlation between position and the magnitudes or change in Mach number. Mach numbers that increase during the run are seen for more upstream locations than when $p_{0,i} = 90$ psia. Unfortunately there were not enough runs made at $p_{0,i} = 170$ psia to determine clear trends in Mach number. However, the farthest downstream position did show Mach numbers that not only increase during the run but are also significantly higher than those found farther upstream or at lower stagnation pressures.

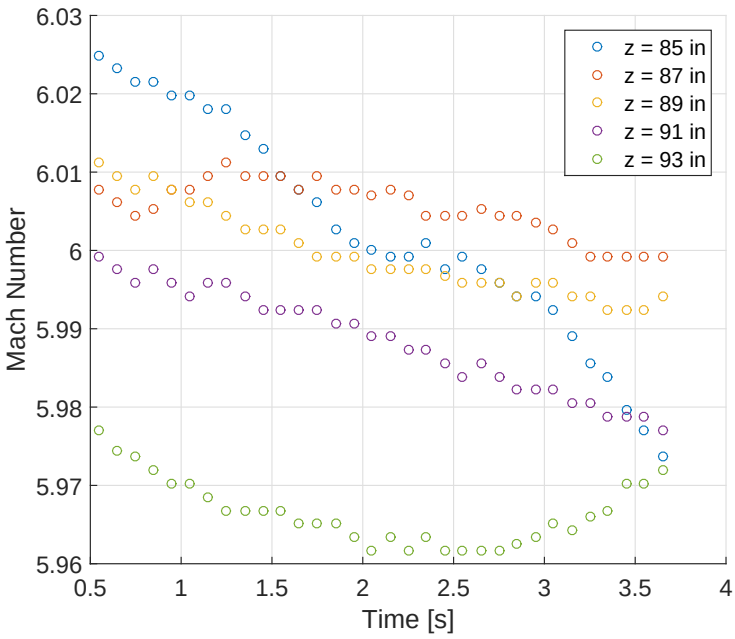

Figure 3.14. Mach numbers when $p_{0,i} = 90$ psia. Probe on centerline.

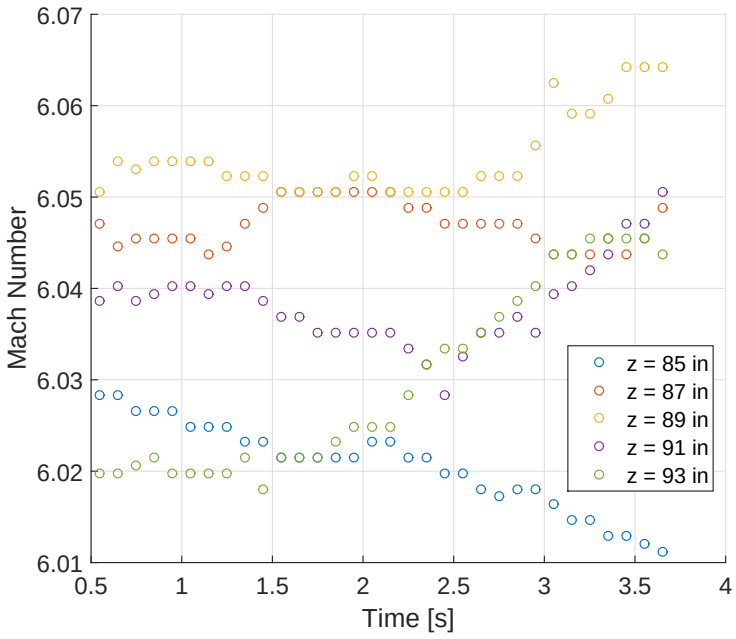

Figure 3.15. Mach numbers when $p_{0,i} = 130$ psia. Probe on centerline.

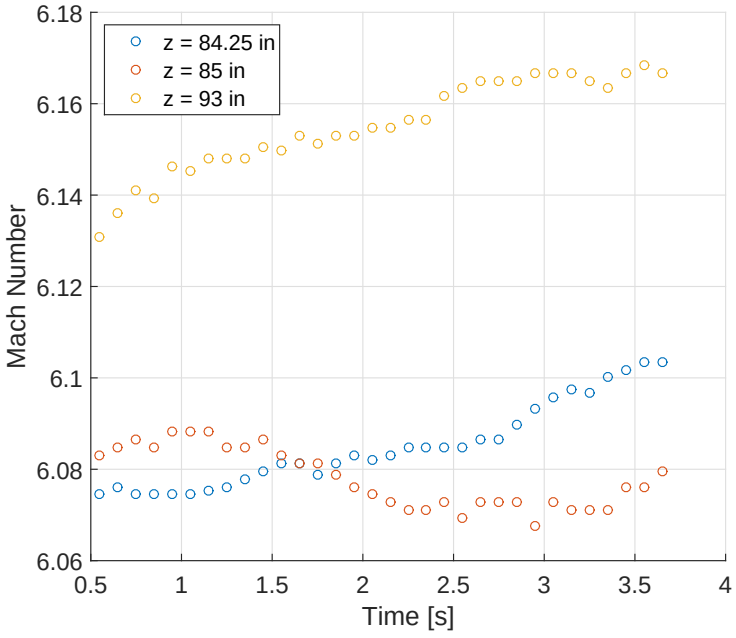

Figure 3.16. Mach numbers when $p_{0,i} = 170$ psia. Probe on centerline.

These changes in Mach number are likely a result of variations in the nozzle-wall boundary-layer displacement thickness, which would cause variations in the effective nozzle diameter. A summary of the axial position dependence Mach number is given in Figure 3.17. This plot shows the change in Mach number during a run as a percent of the Mach number at $t = 0.5$ s for each initial stagnation pressure. When $p_{0,i} = 90$ psia, there is not a clear increase in Mach number as z increases. However, for the two higher pressures, Mach number does increase as the probe moves downstream. Regardless of this trend, the difference in Mach number is, at most, 1.1% (for $p_{0,i} = 170$ psia and $z = 93$ in). This suggests that the noise increase seen after two seconds of runtime does not significantly affect the Mach number.

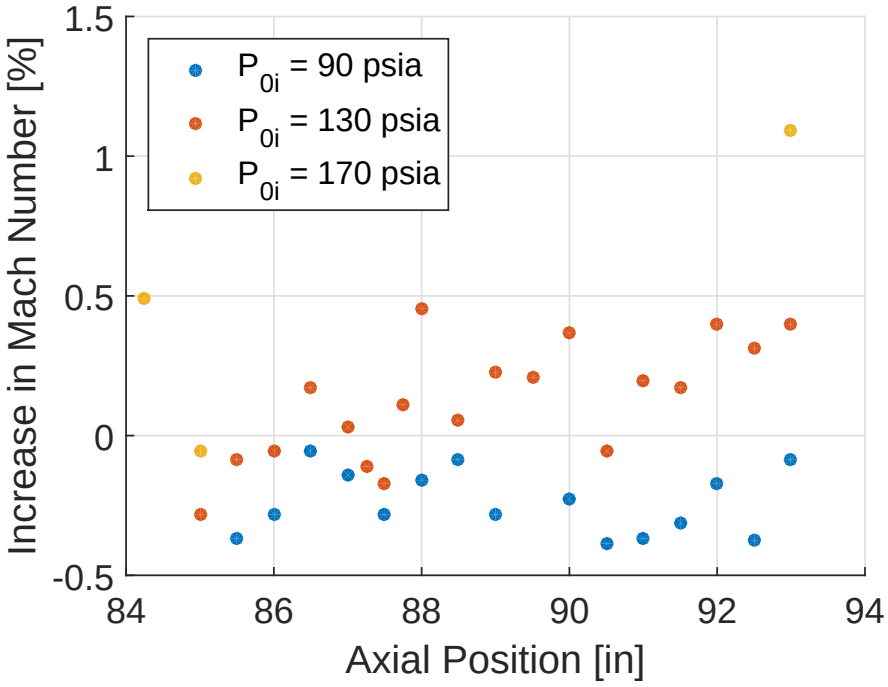

Figure 3.17. Increase in Mach number at the end of a run as a percentage of the Mach number at $t = 0.5$ s.

3.3 Effects of Pitot Probe Geometry

The experiments discussed in this thesis all utilize a pitot probe containing a pressure transducer. The bow shock that forms in front of the sensor affects the measured pressure fluctuations, and it is therefore impossible to directly measure the freestream disturbances. The measurements presented here examine the effects of probe size on the measured fluctuations to gain insight into the nature of pitot-probe transfer functions.

3.3.1 Power Spectral Densities

Unless otherwise stated, the probe was positioned on the tunnel centerline at an axial location of $z = 93$ in. downstream from the throat using the methods discussed in Section 2.2.1. Initial stagnation pressures of both $p_{0,i} = 130$ psia and $p_{0,i} = 45$ psia were used to determine any Reynolds number effects. The tunnel was run under noisy flow conditions for all data presented in this section. The power spectral densities of the normalized pressure fluctuations were calculated using the methods described in Section 2.3.4 from segments of data 0.1 seconds in length corresponding to a specific Reynolds number in the middle of the segment. For the $p_{0,i} = 45$ psia runs, $Re = 3.5\times10^6$/m, and for the $p_{0,i} = 130$ psia runs, $Re = 10.1\times10^6$/m. In all cases, the pressure fluctuations are normalized by the mean pitot pressure during the 0.1 second segment of data. Figure 3.18 shows the typical power spectral densities for measurements using each sleeve on the centerline at two different Reynolds numbers for noisy flow conditions. Figure 3.19 shows the small and large sleeve results for both Reynolds numbers to better show Reynolds number effects. The peak around $f = 260$ kHz is the resonance of the Kulite and is not a feature of the flow. For both Reynolds numbers, similar trends can be seen with respect to the forward-facing diameter. The no-sleeve case resulted in noticeably larger pressure fluctuations for most of the frequency range compared to the three cases where a pitot sleeve was used. At frequencies below 50 kHz the PSD for the large sleeve and the medium sleeve are very

similar. At the lower Reynolds number, the PSD falls off more sharply as frequency increases than for the higher Reynolds number. Small peaks just below $f = 50$ kHz are more visible for the higher Reynolds number. Finally, a small peak can be seen around $f = 150$ kHz for all cases but is most noticeable at the higher Reynolds number. It is possible that this feature is due to a resonance between the sensor face and the shock wave produced by the probe. As previously mentioned in Section 1.4, resonance between the shock and the probe was seen in the simulations done by Chaudhry and Candler [44]. However, the peak frequency in the computationally-determined transfer functions for flow-parallel disturbances was not $f = 150$ kHz, and it is not yet known how the peaks will change due to angled disturbances.

Several steps were taken to determine the repeatability of the dependence on sleeve size of the measured PSDs. One of those steps was comparing the data gathered for this thesis with similar data taken by Sweeney, who did not have data from multiple runs under the same conditions [55]. These data will be shown along with numerical results for comparison in the following section. In addition, when the data presented here were taken, at least two runs for each condition were performed to ensure repeatability. Off-centerline runs were performed for each sleeve to confirm that centerline effects did not influence the data. Figure 3.20 shows the PSDs resulting from measurements taken on the tunnel centerline along with those taken one inch below it. These plots show little variation in measured PSDs and indicate that the data presented here are repeatable.

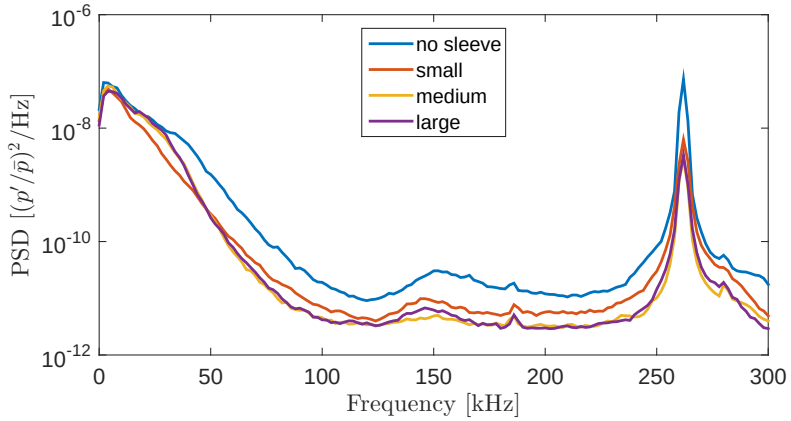

(a) $p_{0,i} = 45$ psia, $Re = 3.5{\times}10^6/\mathrm{m}$

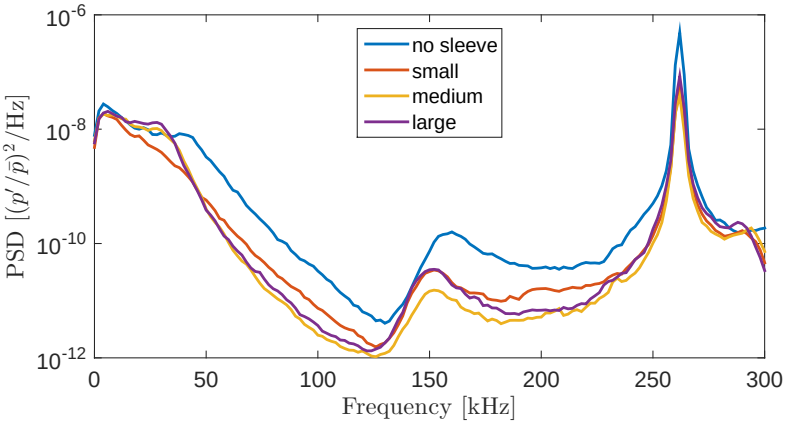

(b) $p_{0,i} = 130$ psia, $Re = 10.1{\times}10^6/\mathrm{m}$

Figure 3.18. PSDs of pressure fluctuations for the four probe geometries for two Reynolds numbers under noisy flow. Probe located on the centerline at $z = 93$ in downstream of the throat.

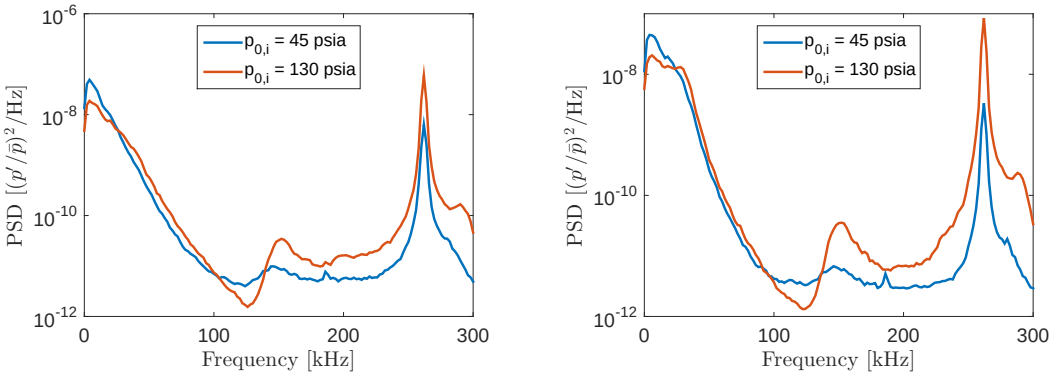

(a) small sleeve (b) large sleeve

Figure 3.19. Comparison of sleeve results for different Reynolds numbers.

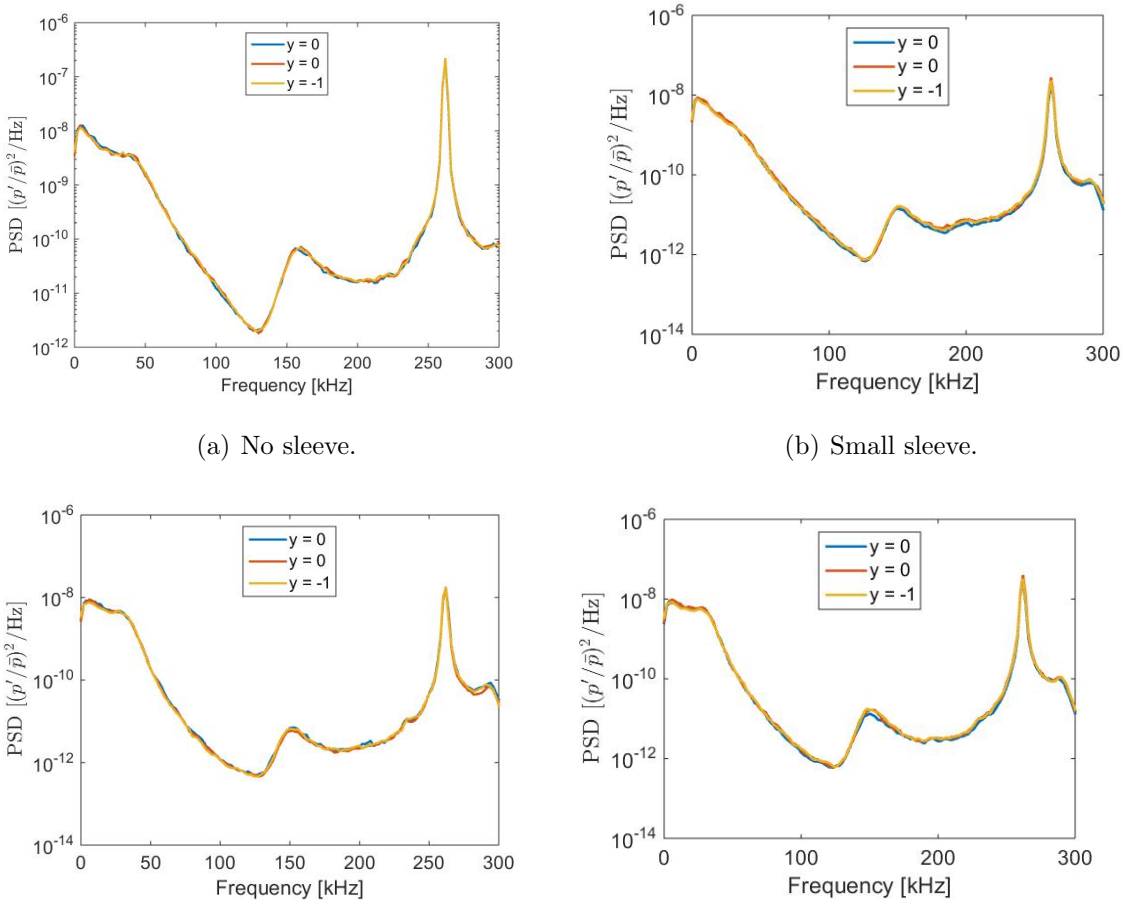

(a) No sleeve.

(b) Small sleeve.

(c) Medium sleeve.

(d) Large sleeve.

Figure 3.20. Centerline ($y = 0$ in.) and off-centerline ($y = -1$ in.) PSDs for each sleeve. $p_{0,i} = 130$ psia, noisy flow, $z = 93$ in.

3.3.2 Noise Levels

The noise levels were determined from PSDs calculated using 0.1 s of data corresponding to a given Reynolds number, including those shown in Figure 3.20. Plots comparing the resulting noise levels for each sleeve configuration are shown in Figure 3.21. Each data point represents the noise level calculated for a single run at the desired Reynolds number. These plots agree with the known trend of increasing noise levels with decreasing Reynolds number. For a given Re, the noise levels generally increase as the forward-facing diameter of the probe increases, with the exception of the no-sleeve case. It is unclear why the no-sleeve case does not follow the trend of the other sleeve sizes. The conditions under which each of these noise levels were calculated were comparable, with the exception of the sleeve size. Nevertheless, the three sleeves produced the same, repeatable trend for both Reynolds numbers. These results indicate that probe geometry has a clear effect on the measured noise levels. Therefore, caution should be used when comparing noise levels taken with probes of different forward-facing diameters, as the results likely depend on probe geometry in addition to freestream conditions.

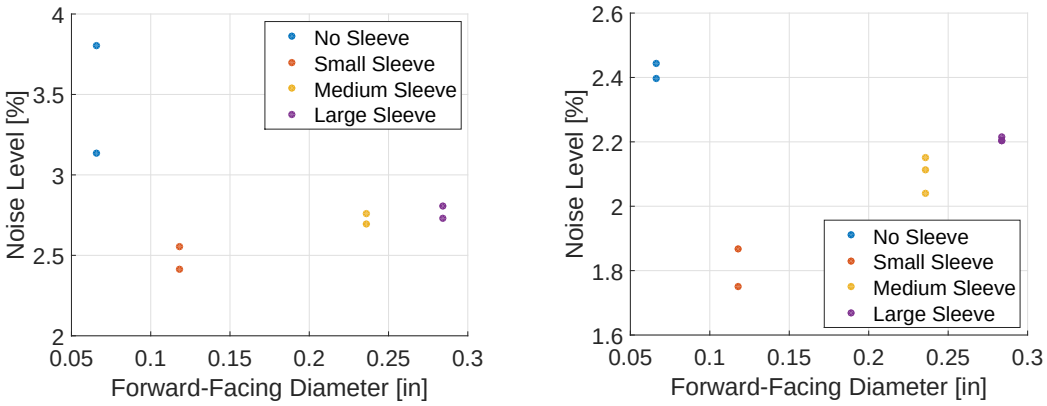

(a) $p_{0,i} = 45$ psia, $Re = 3.5{\times}10^6$/m (b) $p_{0,i} = 130$ psia, $Re = 10.1{\times}10^6$/m

Figure 3.21. Noise levels under noisy flow conditions, $z = 93$ in.

3.3.3 Comparisons to Computational Results

It is important to reiterate that the above results do not represent the freestream fluctuations, but rather those that have passed through the shock wave produced by the probe. The freestream cannot be directly measured with a pitot probe, so it is of interest to determine the transfer function of the probe, which could then be used to estimate the freestream fluctuations. Because it is not feasible to experimentally measure the transfer function for the general case, it must be calculated from simulations. The following simple method of combining the results from multiple probes was suggested by Chaudhry [47] and allows numerical and experimental comparisons. As stated in Section 1.4, the disturbances assumed in the simulations are acoustic fluctuations of a constant amplitude that impinge on the probes at an angle of 120°. The transfer function χ is defined as

$$\chi_{probe} = \frac{PSD_{probe}}{PSD_{\infty}} \tag{3.1}$$

and has been numerically shown to depend on probe geometry. If the forward-facing diameter of the probe is varied, the resulting PSDs calculated from measurements taken with two different diameters will change. Similarly, transfer functions computed using direct numerical simulation (DNS) will depend on the probe diameter. This size dependence is the bridge between experiments and simulations. The ratio of the transfer function of a probe with a sleeve to that of the sensor without a sleeve is then given by:

$$R_{sleeve} = \frac{\chi_{sleeve}}{\chi_{no-sleeve}} = \frac{PSD_{sleeve}}{PSD_{no-sleeve}} \tag{3.2}$$

when PSD_{∞} is assumed to be constant across runs of the same Reynolds number. Thus, this ratio allows direct comparisons to be made between the experimental measurements of the power spectral densities and numerical calculations of the transfer function. The ratios defined in Equation 3.2 are computed from the PSDs previously shown for each sleeve and Reynolds number, and are presented in Figure 3.22. Data for each Reynolds number are presented together to allow comparisons between sleeve sizes. As was seen in the PSDs, the results for the large sleeve and the medium sleeve

are similar while the small-sleeve case yields noticeably different results. Specifically, the peak below $f = 50$ kHz is much more defined for the two larger-sleeve ratios. The increase in the ratio for all three sleeves just under $f = 150$ kHz is present for all sleeves and ratios. There is no clear trend regarding this peak and sleeve size, but it is more prominent for higher Reynolds numbers.

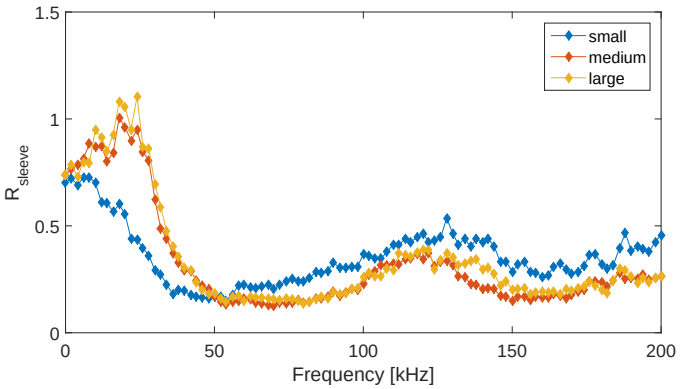

(a) $Re = 3.5{\times}10^6$/m

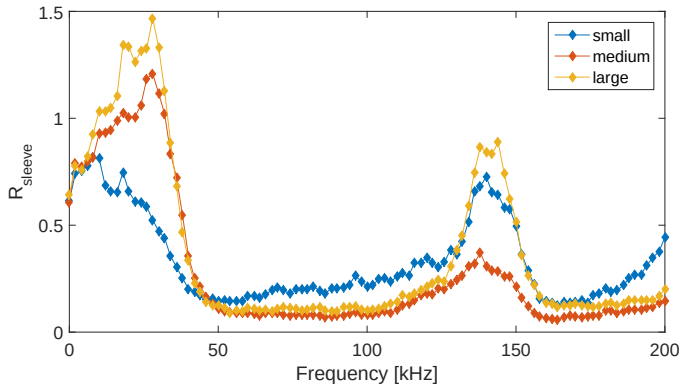

(b) $Re = 10.1{\times}10^6$/m

Figure 3.22. The ratios of the PSDs from the probes with the various sleeves to the PSD of the no-sleeve case.

Although these ratios allow easier comparison between the measured fluctuations depending on the sleeve size, the main purpose of calculating them is to compare experimental results to simulations. Figures 3.23 through 3.25 show both the experimentally and numerically derived ratios for each sleeve. Note that each plot shows

the ratios for a given sleeve size, the simulated results depend on sleeve size only (not on Reynolds number), and that results are also include from the data taken by Sweeney [55].

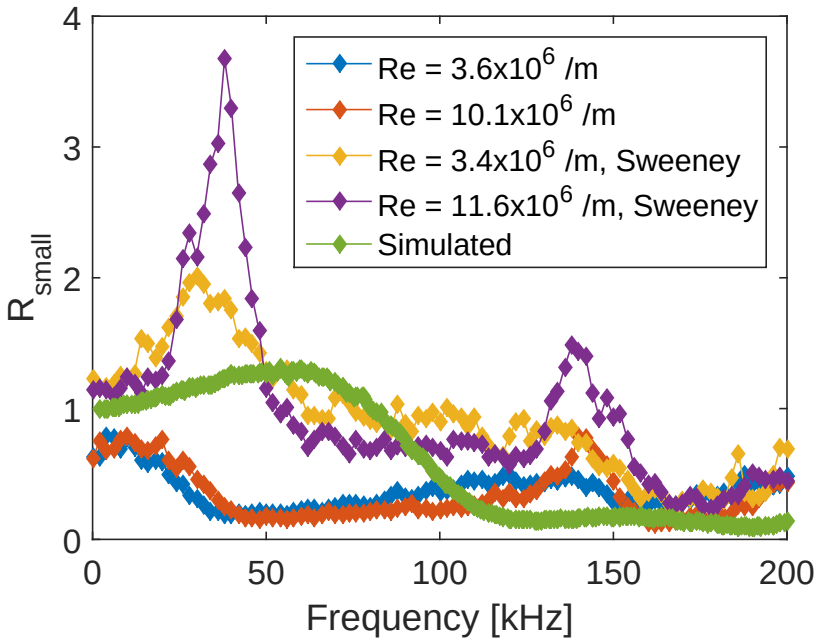

Figure 3.23. The ratios of the small-sleeve to the no-sleeve PSDs.

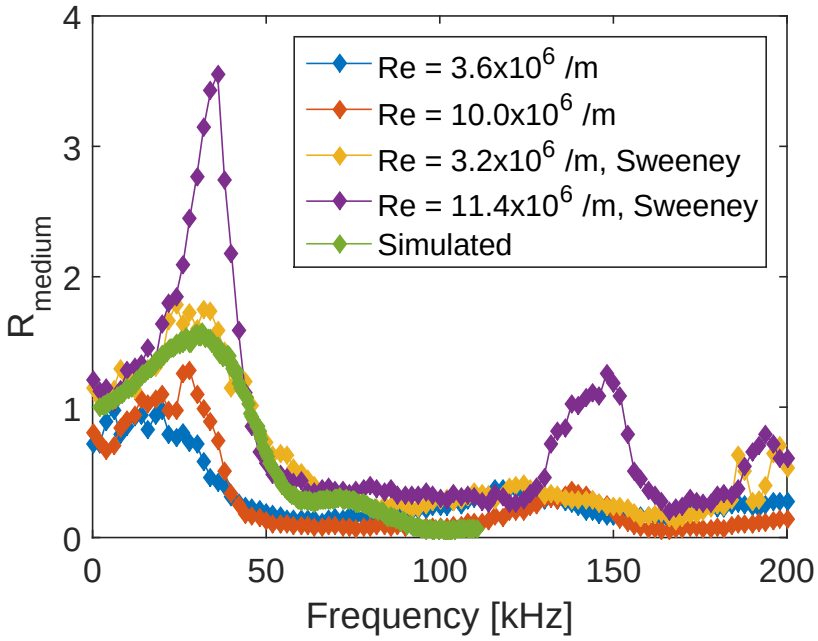

Figure 3.24. The ratios of the medium-sleeve to the no-sleeve PSDs.

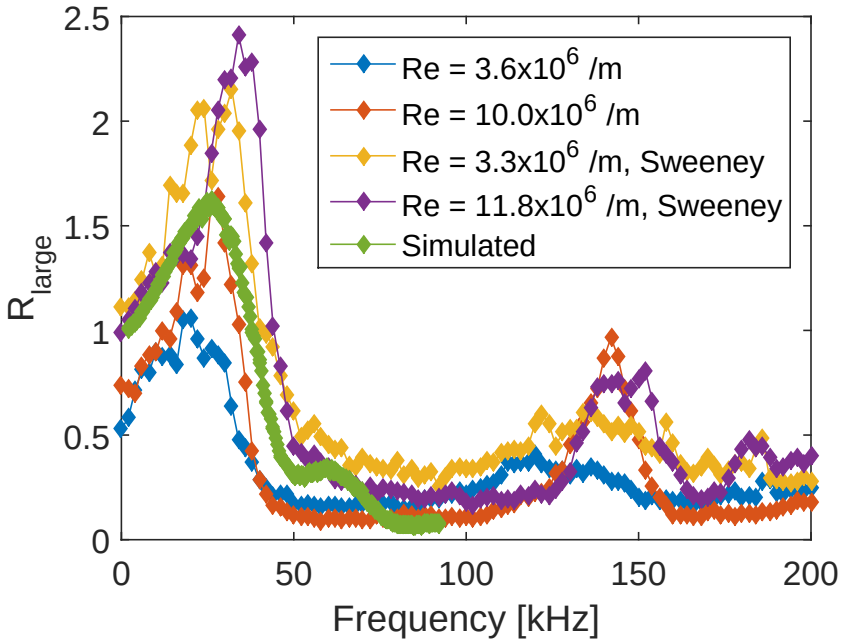

Figure 3.25. The ratios of the large-sleeve to the no-sleeve PSDs.

The experimental results found in both the author's data and Sweeney's indicate a Reynolds-number dependence, but the numerical simulations performed by Chaudhry were independent of Reynolds number. Although the general shapes can generally be seen in each plot for runs with different Reynolds numbers, there is significant scatter in the sizes of the peaks and frequencies of the peaks. In particular, the present author's data resulted in ratio amplitudes that are much lower than Sweeney's and that occur at much lower frequencies. However, if each researcher's data is looked at independently, the peaks in R_{sleeve} for each sleeve diameter are consistently larger for larger Reynolds numbers. The simulated ratios lie in the range of the experimental scatter for the medium and large sleeve results, and a few select experimental runs do match well with computations. However, the simulations for the smallest sleeve produced a ratio that was furthest from the experimental results. Overall, the experimental data do suggest a Reynolds number dependence.

Like the measured PSDs, the ratios computed from the measurements taken by the author were consistent throughout the data set. However, there is a significant difference between those results and those computed from Sweeney's data. Sweeney's data did not include repeat runs, so it is not possible to determine if his measurements were consistent. The present author processed Sweeney's data with the same methods as the rest of the data, so the variations are due to the data themselves and not a difference in analysis. About a year passed between the collection of the two data sets, during which the nozzle was opened for o-ring replacement. It is possible, although unlikely, that the tunnel freestream changed significantly enough in that time to affect the results. This would be especially surprising considering the present measurements were taken under noisy flow conditions. There was no observed difference in measured PSDs after the o-ring was replaced. However, small differences in the PSDs could become significant when the ratio is taken.

Additionally, the variations could be due to the way the data was obtained. The two data sets were not collected using the same sensor. Small differences in probe angle of attack may result in different measurements, especially since the simulations

were found to depend significantly on the angle of the incident disturbances [46]. Also, Sweeney's data was taken with the original Kulite wire intact. It is possible that cutting the Kulite wires and using the connectors, as described in Section 2.2.3, affected the sensor measurements. However, connectors such as those used for these experiments are commonly used with Kulites in the wind tunnel community and have not been shown to affect measurements. Figure 3.26 shows the electronic noise from before and after cutting the wires along with a typical signal for noisy flow. The PSDs shown are the raw voltages which have not been normalized, and the no-flow signals were taken at atmospheric pressure. The baseline noise spectra for both the intact cable and the cut cable with the connectors are well below the amplitudes of the noisy flow fluctuations. Furthermore, the sensor was calibrated each time a new sleeve was used and the wires were reconnected. Each calibration contained at least 8 data points in the relevant pressure range of 2 to 8 psia. The calibrations were all linear with an R^2 value of 0.9999 or 1.000 and were almost identical for each sleeve. Despite the similarities in calibrations, voltage data from each run were converted into pressure using the calibration for the particular sleeve.

The magnitudes of the ratios differ greatly between datasets. Some experimental scatter is expected, but this large of a difference is strange. One cause for the lack of good comparison may be the no-sleeve cases measured by the author. Recall that the no-sleeve noise levels were much larger than those taken using sleeves, and that they went against the trend. If the no-sleeve PSD magnitudes are artificially high, all of the ratios of the sleeve to no-sleeve PSDs would therefore be artificially lower. Figure 3.27 shows the ratios of the two larger sleeves to the smallest-sleeve case to remove the no-sleeve case from the ratios. Despite not using the no-sleeve data, there are still significant differences between the two sets of the experimental results. Thus, the no-sleeve measurements do not appear to be the only factor preventing good comparison between experiments. The cause of the stark difference in magnitudes between experimental data sets is unknown.

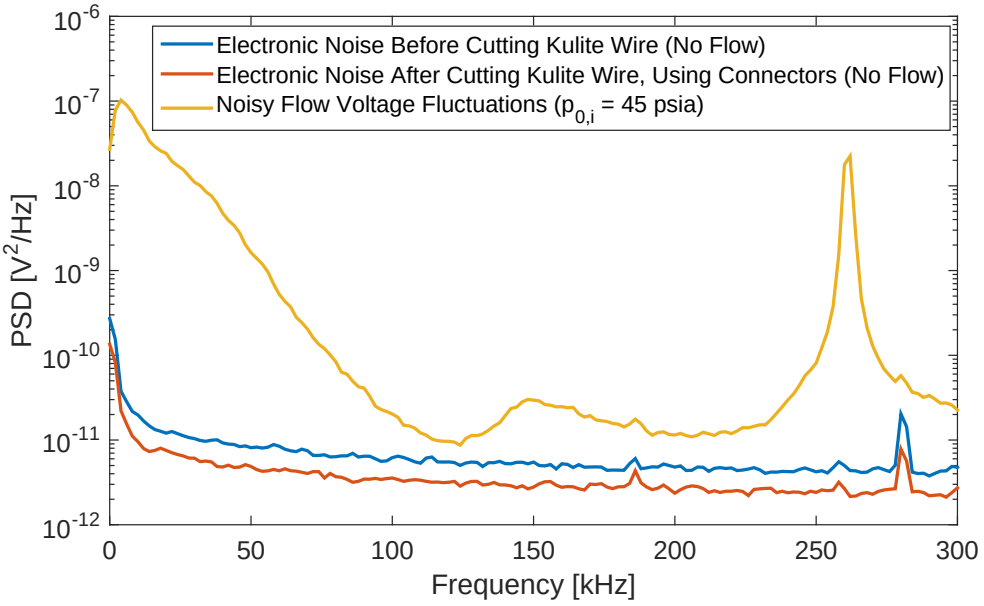

Figure 3.26. PSDs of the electronic noise from the intact wire and the cut wire that was connected with pin-and-socket connectors. The noisy flow trace is from the no-sleeve case and is included for reference. Note that all three PSDs are calculated from the raw voltage signals.

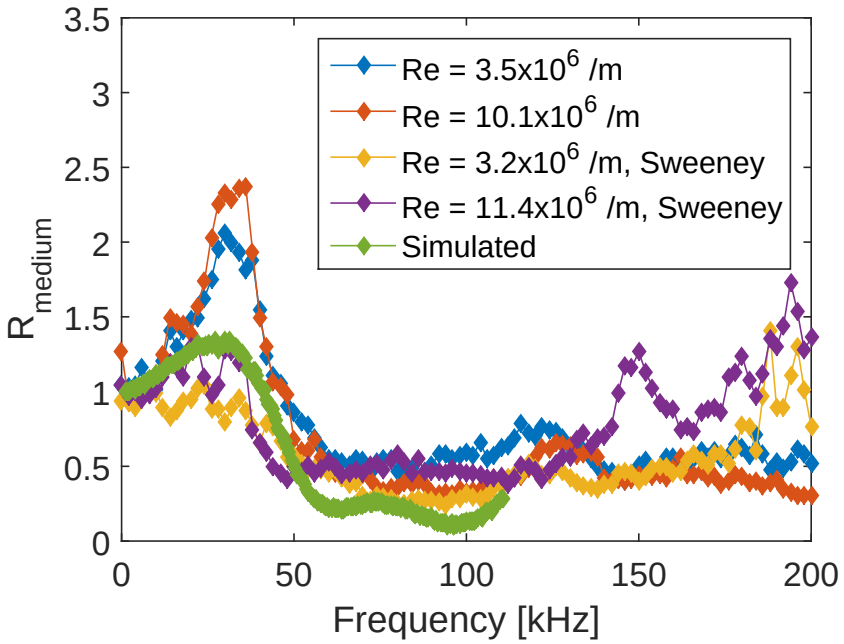

(a) Ratios of medium sleeve to small sleeve.

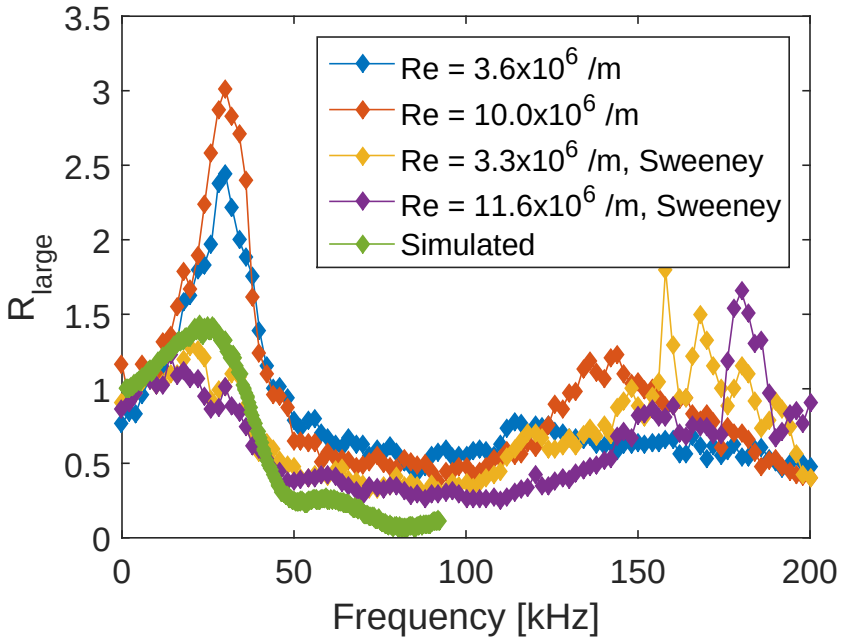

(b) Ratios of large sleeve to small sleeve.

Figure 3.27. Ratios resulting from dividing by the small sleeve PSDs.

3.4 Cone-Mounted Pitot Probe

Tunnel characterization measurements in the BAM6QT are typically taken using a pitot probe in the freestream and an otherwise empty tunnel. The experiments presented here were performed to verify that all regions of the model experience quiet flow.

The apparatus described in Section 2.2.4 was used to mount an A-screen Kulite sensor in a pitot probe on the base of a 7° half-angle circular cone. The cone was nominally at zero degrees angle of attack. Each quiet-flow run had an initial stagnation pressure of 130 psia, which was the highest pressure for which the flow was consistently quiet at the time of the experiments. There were no bleeds-closed runs made with the cone-mounted pitot probe because the goal was to ensure quiet flow at the aft end of a model. The probe was moved between runs to vary the parameter h, which is defined as the distance between the center of the sensor and the surface of the cone at the axial location of the sensor. A ruler accurate to $1/64^{th}$ in. was used to measure the distance between the base of the pitot-probe support and the center of the aft end of the Kulite support, which has a diameter of 0.25 in. The measured distance was then converted to h to give the height above the surface at the axial location of the sensor. The technique used to measure the distance above the probe base is thought to result in a measurement uncertainty of approximately 0.05 in. due to the lack of a concrete reference point on the back end of the Kulite support.

The shock location was determined by the measured pitot pressure. When the sensor is in the Mach-6 freestream, a strong shock is formed by the pitot probe. The stagnation pressure across the probe's bow shock decreases sharply. However, when the probe is inside the cone's shock, the Mach number is lower and the drop in stagnation pressure is less drastic. The measured pitot pressures inside the cone's shock are therefore larger than those measured when the sensor is located outside the cone's shock. A total of ten runs were performed: five runs determined to be inside the shock and five outside.

Two values for the shock location were determined using numerical methods. The first was found from the axisymmetric Taylor-Maccoll solution, which was calculated for a 7° cone in Mach-6 air with $T_0 = 423$ K. The shock angle was determined to be 11.94°, resulting in a standoff distance of 1.35 inches above the cone surface at the location of the sensor. The second numerically-derived shock location was calculated using the axisymmetric Navier-Stokes solver in STABL (Stability and Transition Analysis for Hypersonic Boundary Layers). The geometry was a 7° cone with $Re = 9.49\times10^6$/m, which is also the Reynolds number for the experimental data. STABL calculated a shock angle of 12.27° and a standoff distance of 1.44 inches above the cone surface at the sensor location.

Figure 3.4 shows the measured pitot pressures for each run, the pressures that were computed from Taylor-Maccoll flow, and the shock standoff distance that was calculated using STABL. Recall that the uncertainty in the pitot-probe position is about 0.05 inches. There is also uncertainty resulting from the computational values, as numerical methods are only as good as their assumptions. The axisymmetric results from the Taylor-Maccoll equation and STABL are simplifications of the true three-dimensional flowfield. The tunnel is not perfectly axisymmetric, and the cone itself was likely at some small angle of attack even though the zero-degree angle-of-attack adapter was used. Nevertheless, there is relatively good agreement between the experimentally-measured pressures and those from the Taylor-Maccoll equation. The difference between the two computational values of shock location is less than 7%. The experimentally-determined location of the shock is between $h = 1.35$ in and $h = 1.4$ in. It was not possible to accurately position the pitot probe between these two values. If the shock location is assumed to be exactly halfway between the two heights, it differs from the Taylor-Maccoll and STABL results by 1.8% and 4.5%, respectively. The Mach numbers for various heights above the cone surface are shown in Figure 3.4. Again, the experimental values are compared to the Taylor-Maccoll solution and relatively good agreement is seen. It was not a primary goal for this thesis to find the exact location of the shock, or to match the experimental data with

the simulated data. Instead, the shock location was approximately determined to ensure data was taken both inside and outside of the shock.

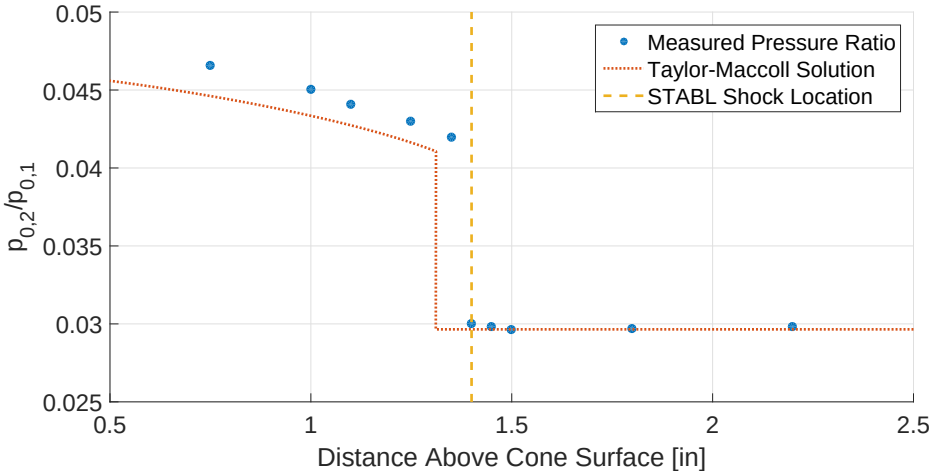

Figure 3.28. The stagnation pressure ratio for each run at varying heights above the cone surface.

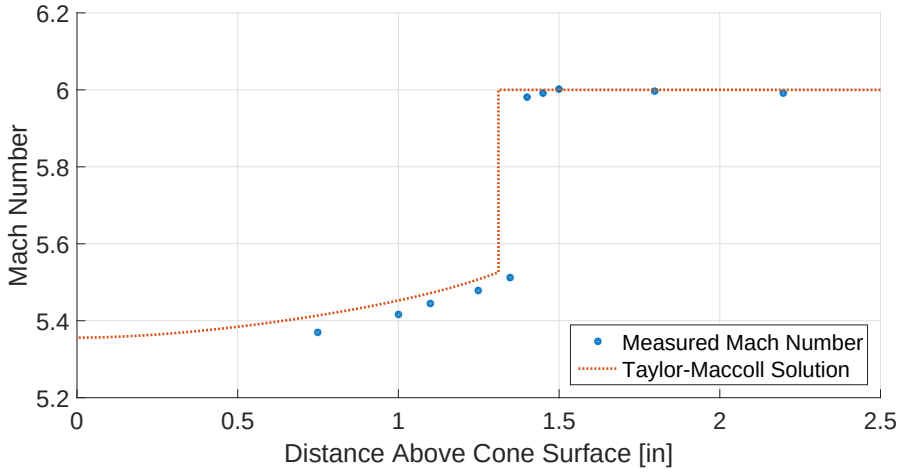

Figure 3.29. The Mach numbers calculated form experiments and those that result from the Taylor-Maccoll Equation.

The power spectral densities for the normalized pressure fluctuations from all runs using the cone-mounted pitot probe are shown in Figure 3.30. The PSDs correspond-

ing to runs for which the probe was inside the measured shock location are shown with solid lines, and the PSDs computed when the probe was above the shock are shown using dashed lines. Only frequencies up to $f = 50$ kHz are shown so the trends can be seen. This is also the region over which PSDs are integrated to calculate noise levels and the region where the Kulite sensor is most reliable. The PSD corresponding to the position farthest from the cone surface (the green dashed line, for which $h = 2.2$ in) has much higher values at low frequencies. This position is 4.02 inches above the centerline, which is outside the approximated boundary-layer displacement thickness at the nozzle exit for Mach-6 quiet flow (0.237 in). Note that the displacement thickness is smaller than the overall boundary-layer thickness, and this position could be measuring some boundary-layer interaction effects. Steen noted increased noise levels under quiet flow when the pitot probe was farther than 4.2 in. from the centerline [54]. For all locations outside the cone's shock there are three peaks below $f = 50$ kHz which have much larger magnitudes than for positions closer to the cone, and they occur at frequencies of approximately 7 kHz, 13 kHz, and 38 kHz. Although these trends are distinct and consistent, the peaks are small compared to the PSD amplitudes in noisy flow. For a comparison of these pressure fluctuations to those seen in noisy flow, see Figure 3.31. The methods used to calculate the PSDs in both Figure 3.31 and Figure 3.30 are the same as was described in Section 2.3. However, note the difference in the axis scales between the two plots.

Figure 3.31 compares the PSDs calculated from data taken with the cone-mounted pitot probe with typical PSDs from a traditional pitot probe under both quiet and noisy flow conditions. The data for the cone-mounted pitot probe were taken at $h = 1$ in above the cone surface, which is inside the measured shock location. Both PSDs from the typical pitot probes were calculated from data taken on the centerline with $p_{0,i} = 130$ psia. Figure 3.31 indicates that although the cone does affect the spectra of the pressure fluctuations, the magnitudes of the fluctuations are still comparable to those in the freestream for quiet flow. It is possible that the higher amplitudes of the fluctuations in the presence of the cone are due to disturbances radiated from

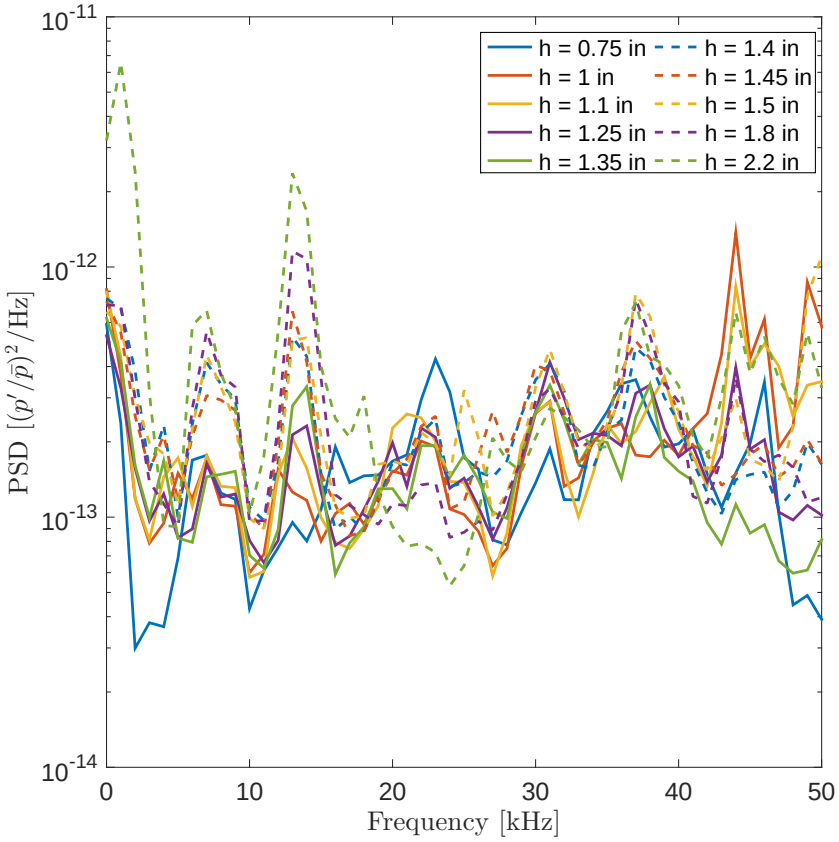

Figure 3.30. PSDs for all runs made using the cone-mounted pitot probe. Dashed lines indicate data from probe positions outside the measured shock location.

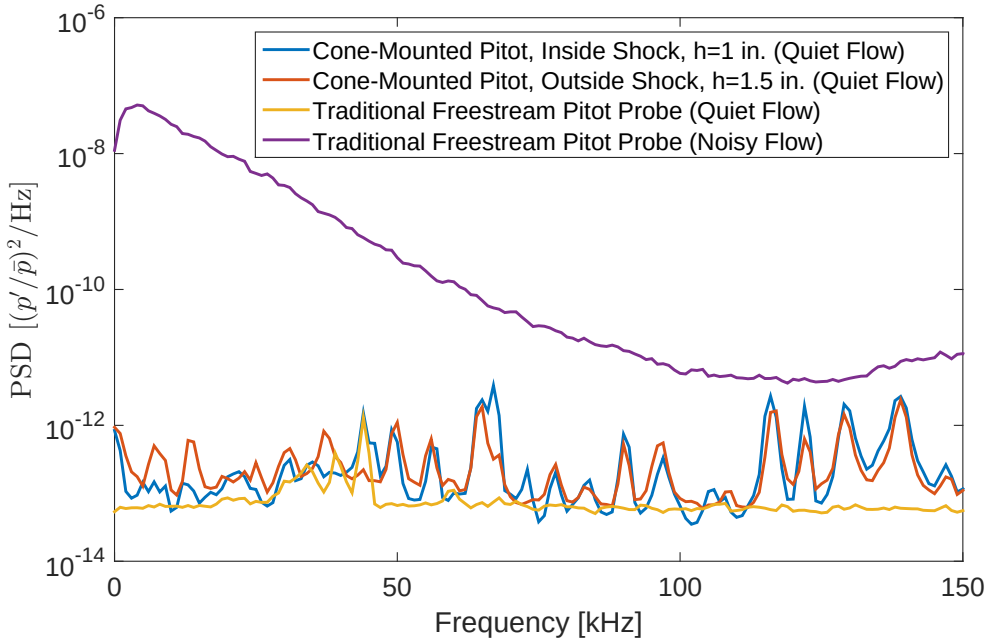

Figure 3.31. PSDs from the cone-mounted pitot probe located inside and outside of the shock and from the traditional pitot-probe hardware on the tunnel centerline.

the boundary layer on the cone. However, a 7°cone at zero angle of attack does not experience transition for the Reynolds number tested here, so the cone boundary layer is laminar. Also note that although the cone-mounted pitot-probe PSD is elevated across most frequencies compared to the typical quiet case, only fluctuations below $f = 50$ kHz are used to calculate noise levels. Thus, peaks in the cone-mounted pitot-probe PSD at frequencies above $f = 50$ kHz do not affect the noise levels.

Noise levels for each position above the cone surface are plotted in Figure 3.32. The noise levels do not indicate shock location. Therefore the shock locations are not given for comparisons but for reference. All values are below the threshold for quiet flow (0.05%) and there is not a significant difference between noise levels inside of and outside of the shock. However, the values do tend to increase as h increases. This trend is expected based on the normalized PSDs shown in Figure 3.30. The magnitudes of the peaks in the 0-50 kHz range are larger for locations outside the

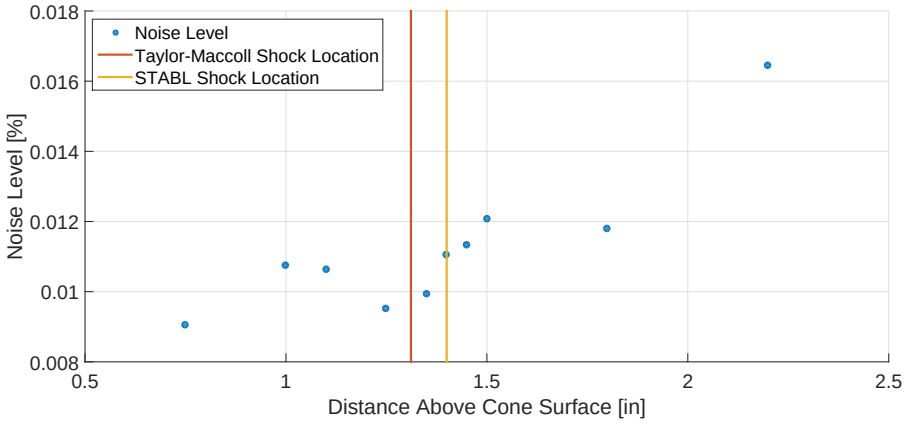

Figure 3.32. Noise levels calculated for each position of the cone-mounted pitot probe as a percent of the mean pitot pressure.

shock, and the noise levels are determined by integrating the PSDs. Furthermore, the noise level for the data taken at $h = 2.2$ in is significantly larger than the other values. As previously mentioned, the point corresponding to the farthest position of the probe away from the cone may measure increased pressure fluctuations due to effects from the nearby nozzle-wall boundary layer. Nevertheless, the noise level for each position measured with the cone-mounted pitot probe is comparable to the quiet noise levels seen when pitot probes are used to measure the disturbances without a model present.

The confirmation that the aft end of a model in the BAM6QT experiences fully quiet flow is significant. As was discussed in Section 1.2, only the upstream regions of models used in the Mach 3.5 Pilot Quiet Tunnel at Langley were under quiet flow, while elevated noise levels impinged upon the back end of the models [21]. As a result, the transition location was dependent on the axial position of the model in the tunnel. The present data shows that measurements made in the BAM6QT do not have this source of uncertainty, as the entire model is under fully quiet flow conditions. Therefore transition measurements made in this tunnel can be confidently assumed to result from the aerodynamics of the model rather than from the position of the model in the tunnel.

3.5 Flow Characterization Using Helium

Experiments were performed in the BAM6QT using helium instead of air. For each run, the entire tunnel was evacuated to vacuum to remove air before the tunnel was filled with helium. Pitot-probe measurements were made in an attempt to characterize the flow when helium was used. There were 17 tanks of helium available which allowed for one run with an initial stagnation pressure of 80 psia (6 tanks), two runs at 40 psia (3 tanks each), and five runs at atmospheric pressure (one tank each). All runs were made with the bleed valves open. The pitot probe was moved using the automated traverse system to increase the amount of data collected with the limited runs.

3.5.1 Kulite Calibration

The pressure transducer used for these experiments was an A-screen XCE-062-15A Kulite that is rated to a pressure of 15 psia. In previous testing, it was discovered that the helium molecules are small enough that they pass through the diaphragm, a phenomena that does not occur with the larger molecules making up regular air. Varying amounts of helium behind the diaphragm cause offsets in the calibration. Therefore, the sensor was calibrated once using air and once using helium to determine any effect helium behind the diaphragm might have. The helium calibration for the pitot Kulite took place after the first run with $p_{0,i} = 40$ psia. Once the ball valve was closed and the pressure in the driver tube settled, the vacuum hose set up for suction experiments was used to control the driver-tube pressure. The valve was open until the pressure dropped below atmosphere, because the Kulite is mechanically stopped above 15 psia. The valve was then closed to maintain a constant pressure. After significant time had passed so the pressure stabilized according to the Paroscientific pressure gage (1-2 minutes), the mean voltage read by the oscilloscope and the pressure read by the Paroscientific gage were recorded. The Paroscientific gage uses a force-sensitive quartz crystal and the frequency of the sensor's output changes with applied pressure [65]. Thus, the Paroscientific gage should not depend on the gas used. The vacuum valve

was again opened to decrease the pressure until the next point. A total of 15 data points were taken.

The contraction Kulite was calibrated similarly, except the data points were taken as the tunnel was being filled with helium. The first step when filling the tunnel with helium is to bring the driver tube to vacuum using the same vacuum hose used to decrease the pressure for the pitot-probe Kulite calibration. Once the pressure reaches its minimum (about 0.3 psia), the helium is added until the desired pressure is reached. For the calibration, the filling process was paused at several points to record the contraction Kulite's voltage and the Parascientific gage's pressure reading. A total of 11 points were used for the calibration, which took place while filling for the second $p_{0,i} = 40$ psia run. Unfortunately, the maximum pressure in the calibration was 45 psia so the calibration does not include data points closer to the maximum pressure used for these tests, which was 80 psia.

The helium calibrations for the two Kulites are compared to the calibrations for the same sensors in air in Figure 3.33. The linear fit for each individual calibration has an R-squared value of at least 0.9998. The two calibrations for the pitot-probe Kulite are not drastically different, especially for the lower pressures that are in the expected range for the pitot probe. However, there is a significant offset between the two contraction Kulite calibrations. The sensor in the pitot probe was calibrated in helium after only two runs, while the contraction Kulite was calibrated in helium after 6 runs had been performed in the same day. Thus, there was much more time for helium to diffuse into the sensor when the contraction Kulite was calibrated. This is likely why a significant offset is not seen between the two calibrations for the pitot-probe Kulite. The helium diffusion is slow, so the calibration changes significantly only over long time periods. The shift should be accounted for after each run so a more accurate calibration can be used. This is not the usual procedure because Kulites do not have this problem in air, but is something that needs to be implemented if helium is used for future testing. For the results presented here, the helium calibrations shown in Figure 3.33 for both sensors were used.

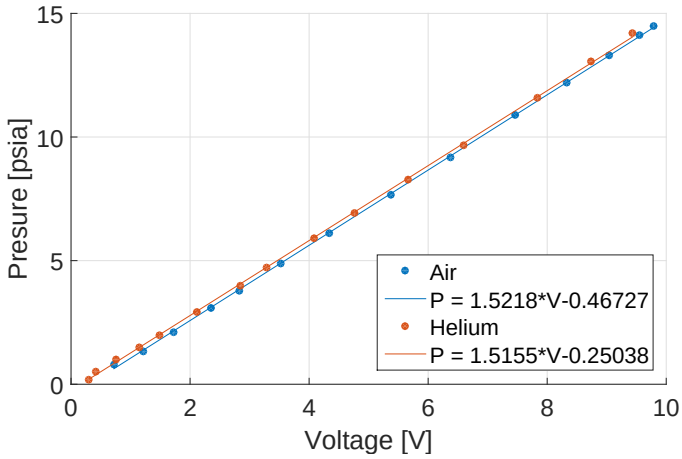

(a) Pitot-probe Kulite

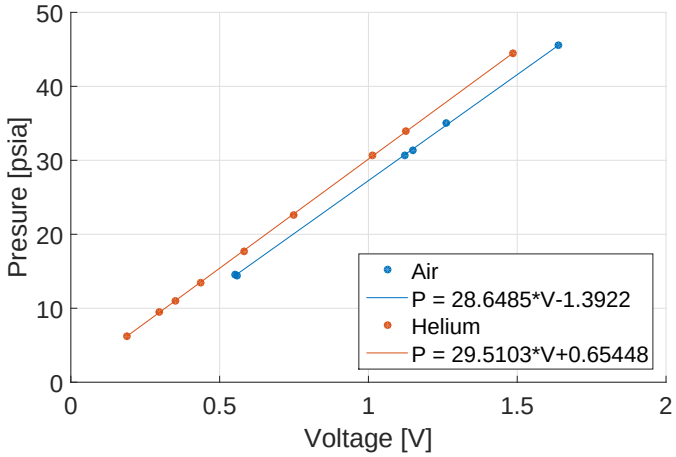

(b) Contraction Kulite

Figure 3.33. Calibrations for the two Kulites in both air and helium.

It is very likely that the calibration might change each time a run is performed if the amount of helium gathering behind the diaphragm changes between runs. This could be accounted for by taking a one-point measurement to determine the offset. Unfortunately, this was not done for the runs presented here, and the oscilloscope vertical range was such that the pre-run voltage data for the pitot-probe sensor were off the screen. Therefore, there is no way to adjust the pitot-probe data for offsets resulting from helium diffusing into the sensor, and thus there is a large uncertainty

in the calibration. However, the pre-run data for the contraction Kulite was captured in the vertical range of the oscilloscope. Figure 3.34 shows the pre-run data points for each of the runs with atmospheric initial pressures. The scatter in the voltage is obvious and significant. Each run allowed more helium to diffuse into the sensor and decreased the output voltage for a relatively-constant pressure. Even if the slope of the Kulite calibration is unchanged by helium, the calibration clearly changes between runs. Although a similar examination of the offset in the calibration of the pitot-probe sensor is impossible, Figure 3.34 shows the magnitude of the uncertainty in the calibrations.

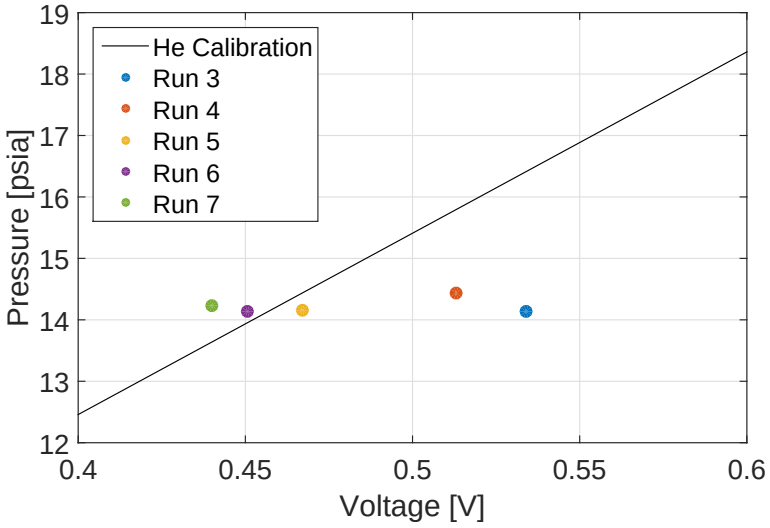

Figure 3.34. Pre-run contraction Kulite voltage and pressure for the 6 runs with atmospheric initial pressures.

3.5.2 Initial Stagnation Pressure of 80 psia

Figure 3.35 shows the mean pressure from the pitot probe during the run with an initial pressure of 80 psia. The red line is the position of the pitot probe measured in inches above the centerline. It appears that uniform flow begins at around $t = 0.1$ s. At t =0.2 s there is a sudden disruption in the signal, followed by fluctuating and

unusual pressures. There does not appear to be a relationship between the pressure and the probe position. The uncalibrated hot film, shown in Figure 3.35(b), shows the same disruption around $t = 0.1$ s. There is a period of relatively stable-looking flow that lasts for approximately one second before the sharp increase after $t = 1$ s indicates tunnel unstart. This was the first helium run performed by the author, and it was not known at the time that tunnel unstart could occur so soon; typically, the BAM6QT produces approximately 4 seconds of flow before unstart. Subsequent runs used a modified traverse movement program that included only two or three measurement locations per run before unstart.

Compared to the pressures during a typical air run, these signals are very strange. Figure 3.36 shows the signals that are typically produced when the bleed valves are open using air. The hot-film signals are taken from the entry in which the cone-mounted pitot probe was used because that is the only entry besides the helium entry for which the new hot film was used by the present author. However, the two pressure traces are from the entry that investigated the noise increase after two seconds because that entry used the same traditional pitot probe used for the helium experiments. Therefore, the colors correspond to different runs. Each plot contains signals that have been offset by some value to distinguish between runs and therefore only show qualitative trends.

The general features of the pitot pressures shown in Figure 3.36(a) are clear: pitot pressure generally steadily decreases during a run, with steps approximately every 200 ms resulting from the reflecting expansion wave. The helium pitot-probe pressure (Figure 3.35(a)) is not at all similar to these traces. The typical hot-film signals shown in Figure 3.36(b) have the same scaling as the hot-film trace from the $p_{0,i} = 80$ psia helium run to better compare the features. Although the hot-film signal from the helium run appears to be steady for about a second, it is significantly different than those typically resulting from air. It is expected that heat transfer would be different for helium than for air, but the details are unknown. Therefore, there is not a good standard to use for comparison to helium runs. The stagnation pressures measured

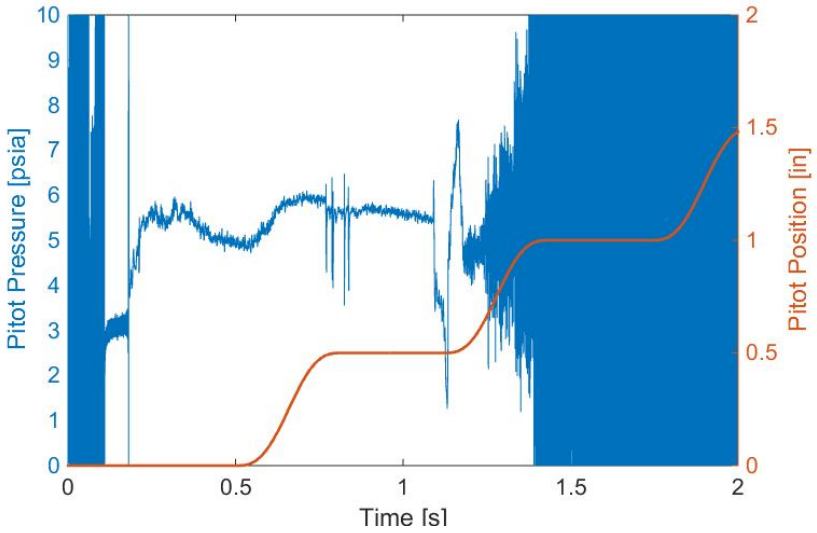

(a) Pitot pressure

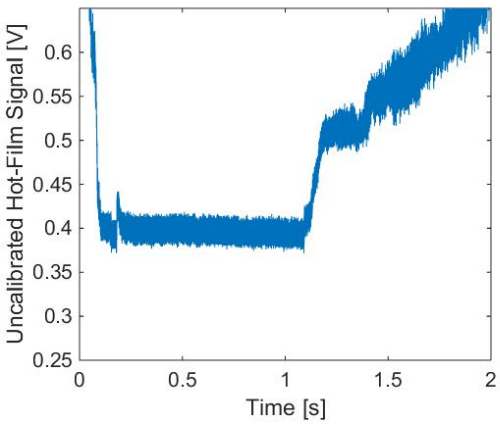

(b) Hot film

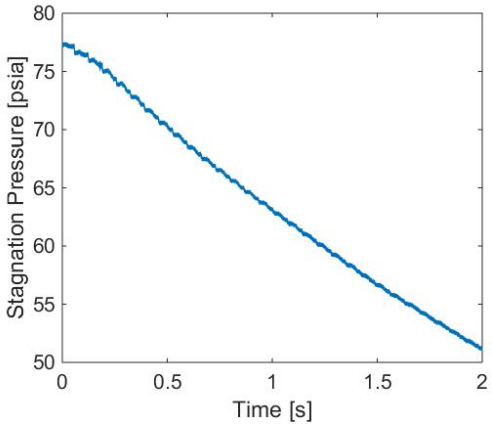

(c) Stagnation pressure

Figure 3.35. Run using helium with with an initial pressure of 80 psia.

by the contraction Kulite during the helium run, shown in Figure 3.35(c), contains much smaller steps from the reflection of the expansion wave than those seen in air. This feature is not unexpected, as the speed of sound in helium is faster than in air and thus expansion wave reflections between the upstream and downstream ends of the driver tube would be shorter.

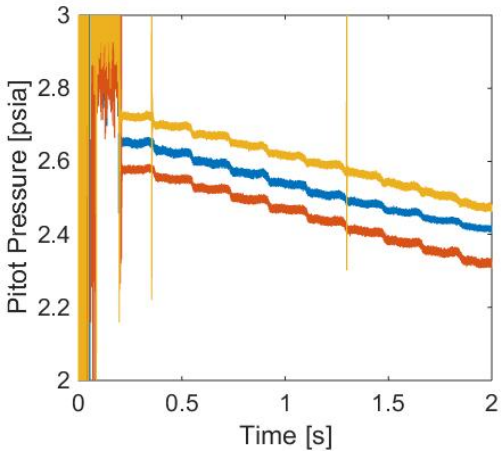

(a) Typical pitot pressures.

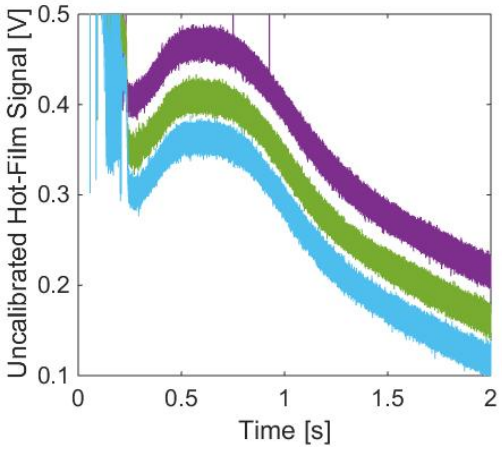

(b) Typical hot-film signals.

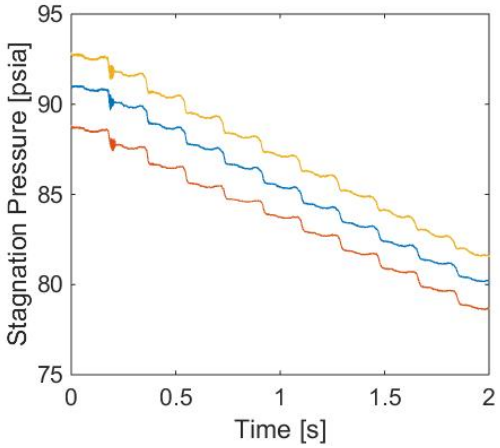

(c) Typical stagnation pressures.

Figure 3.36. Typical traces for quiet runs using air. Different colors indicate different runs. Values are qualitative because signals contain offsets for visibility and only trends are shown.

The stark differences of the pitot-probe and hot-film signals seen in helium compared to those typical of quiet-flow runs suggests that the tunnel may not have started for this run. The hot film used for these experiments was the new Dantec hot film. Not much is known about how it reacts when the tunnel fails to start, for example, due to blockage. Previous blockage experiments in the BAM6QT were performed with the Senflex hot-film array. A comprehensive study of the differences between

the two hot films has not been performed. The pitot pressure contains the previously-discussed calibration uncertainty due to helium diffusion into the sensor. However, it should be noted that an offset in the calibration could not be the sole cause of the unusual shape seen in Figure 3.35(a). It is possible that the odd signal was caused by non-steady flow produced because the tunnel did not fully start. In particular, unsteady separation of the nozzle-wall boundary layer could result in the sporadic behavior seen in the pitot traces. A Kulite was installed on the nozzle wall with the new hot film. Future experiments using helium should include measurements made with this sensor to investigate this theory. However, the wall Kulite was not operational at the time of these measurements.

3.5.3 Initial Stagnation Pressure of 40 psia

Two runs began with a total pressure of 40 psia, one for which the probe started at the centerline and moved up (Figure 3.37), and one for which the probe began three inches above the centerline and moved down (Figure 3.38). The hot film traces, which are shown in Figures 3.37(b) and 3.38(b), show the same strange behavior seen for the run with $p_{0,i} = 80$ psia.

The pitot-probe signals for this initial total pressure are also different from those that typically result from quiet runs with normal air. The peak in the pressure in Figure 3.37(a) near $t = 0.2$ s appears to be some artifact resulting from startup. This is followed by almost a second of relatively uniform pressure that coincides with the probe moving up half an inch. Once the probe reaches one inch above the centerline, the pressure signal is no longer constant. However, this is likely a result of being closer in time to tunnel unstart. It is unclear if the probe position affected the pressure, especially since the time period $t \approx [0.4 : 0.7]$ s contains a near-constant pressure while the probe moves. Although the near-steady pressure that occurs for about a second during this run is less sporadic than the trace when $p_{0,i} = 80$ psia, it does not

display the same features that are seen in typical air runs, namely the steady decrease in pressure with jumps approximately every 200 ms.

Figure 3.38(a) shows the pressure during the $p_{0,i} = 40$ psia run that started three inches above the centerline. Based on computations, this starting position is expected to be in the boundary layer and would thus have very low pitot pressures [66]. However, there are periods of time for which the pressures are negative. This is likely an indication of a calibration offset caused by helium entering the cavity behind the sensor diaphragm after the calibration was performed. However, when the probe moves down to two inches above the centerline, the pressure is more constant and nonnegative for about 0.4 s. Again, this may not be a result of the probe position because part of the time for which the pressure is constant corresponds to times when the probe was moving.

The pitot-probe Kulite was calibrated just after the first run with $p_{0,i} = 40$ psia. It is therefore likely that the sensor's calibration is more accurate for this run than any other run this entry. Additionally, there is a period of relatively stable pitot pressures between approximately $t = 0.1$ s and $t = 1.1$ s. The Mach numbers were calculated for intervals of 0.1 s during this time period and are shown in Figure 3.39. The position of the pitot probe is not taken into account here for two reasons. First, Figure 3.37(a) does not indicate that the positions affects the pitot pressure in this time period. Second, the probe moves off the centerline by only 0.5 in. Therefore, the probe remained in the core flow for this time segment. Note that the pressure drops during a run, so runtime increases from right to left for this plot. The Mach number generally decreases with decreasing stagnation pressure. For this run, the largest source of error is likely the calibration of the contraction Kulite that is used to determine the stagnation pressure.

3.5.4 Initial Stagnation Pressure of 14 psia

There were six runs made with an initial stagnation pressure of about one atmosphere (Figure 3.40). Each run contains several tenths of a second with relatively stable pitot pressures, which sometimes coincide with a period of rest for the pitot probe. However, these runs display the same unusual fluctuations as those for higher pressures using helium, and are not similar to air runs. There are also several instances where the pressures are negative due to the calibration offset that can not

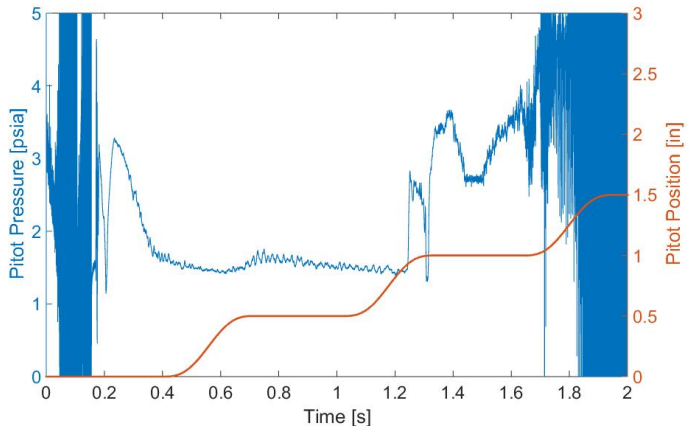

(a) Pitot pressure

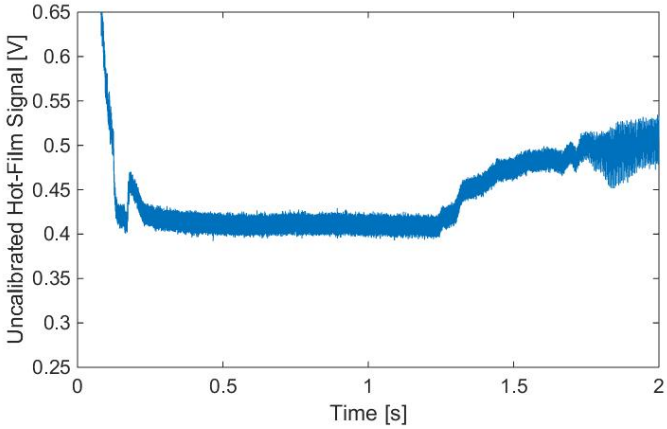

(b) Hot film

Figure 3.37. The first run with $p_{0,i} = 40$ psia using helium.

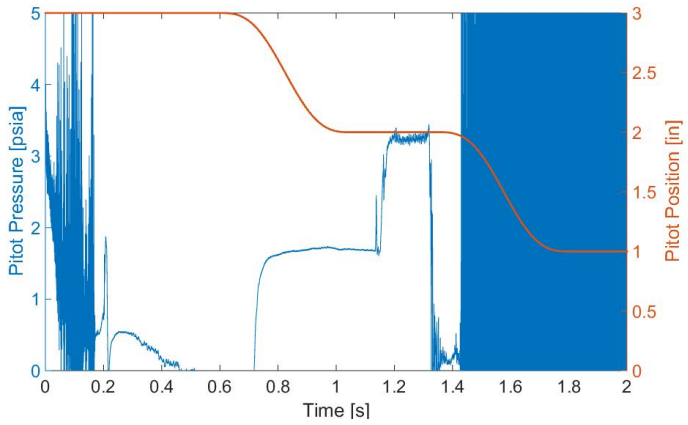

(a) Pitot pressure

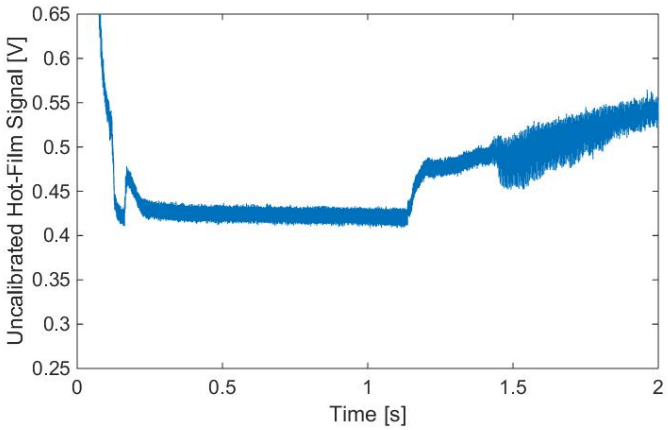

(b) Hot film

Figure 3.38. The second run with $p_{0,i} = 40$ psia using helium.

be accounted for with the available data. Several of the latter runs were made with small pitot-probe movements in an attempt to find the location of the boundary layer, which would contain lower pitot pressures. Unfortunately, due to calibration issues, it is not possible to say with any certainty where the boundary layer is.

The hot-film signals for each of the atmospheric runs were nearly identical, and a typical hot-film trace is shown in Figure 3.41. The hot-film signal is again unlike those typical for runs using regular air, although it does not display the sudden increase in magnitude seen for the other helium runs. It is possible that tunnel unstart is not

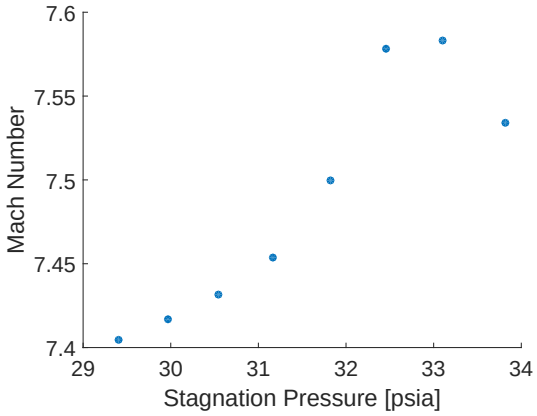

Figure 3.39. Mach number calculated during the first run with $p_{0,i} = 40$ psia.

as violent for runs with lower stagnation pressures. There is no obvious relationship between the hot-film trace for a particular run and the corresponding pitot-pressure trace. Even if the near-constant pitot pressures do indicate that the tunnel has started, there is no way to tell when during the run this happens using the hot film when a model without a pitot probe is used.

3.5.5 Comparisons to Simulations

A numerical solution of helium flow in the BAM6QT nozzle was performed by S. Esquieu using Fluent [66]. The mean-flow computations were based on the fully laminar, 2-D, steady Navier-Stokes solutions. The simulated and experimental pressure ratios between the pitot pressure and the freestream stagnation pressure ($p_{0,2}/p_{0,1}$) are shown in Figure 3.42. Due to the unusual behavior seen in the time traces, only segments of time which exhibited a relatively stable pitot pressure were used to determine these experimental results. Time periods of 0.1 s were used for each point except the one point used from the $p_{0,i} = 80$ psia run. A shorter segment of 0.05 s was used for this run because the pitot pressure trace was particularly sporadic and a 0.1-s period of near-constant pitot pressure was not available.

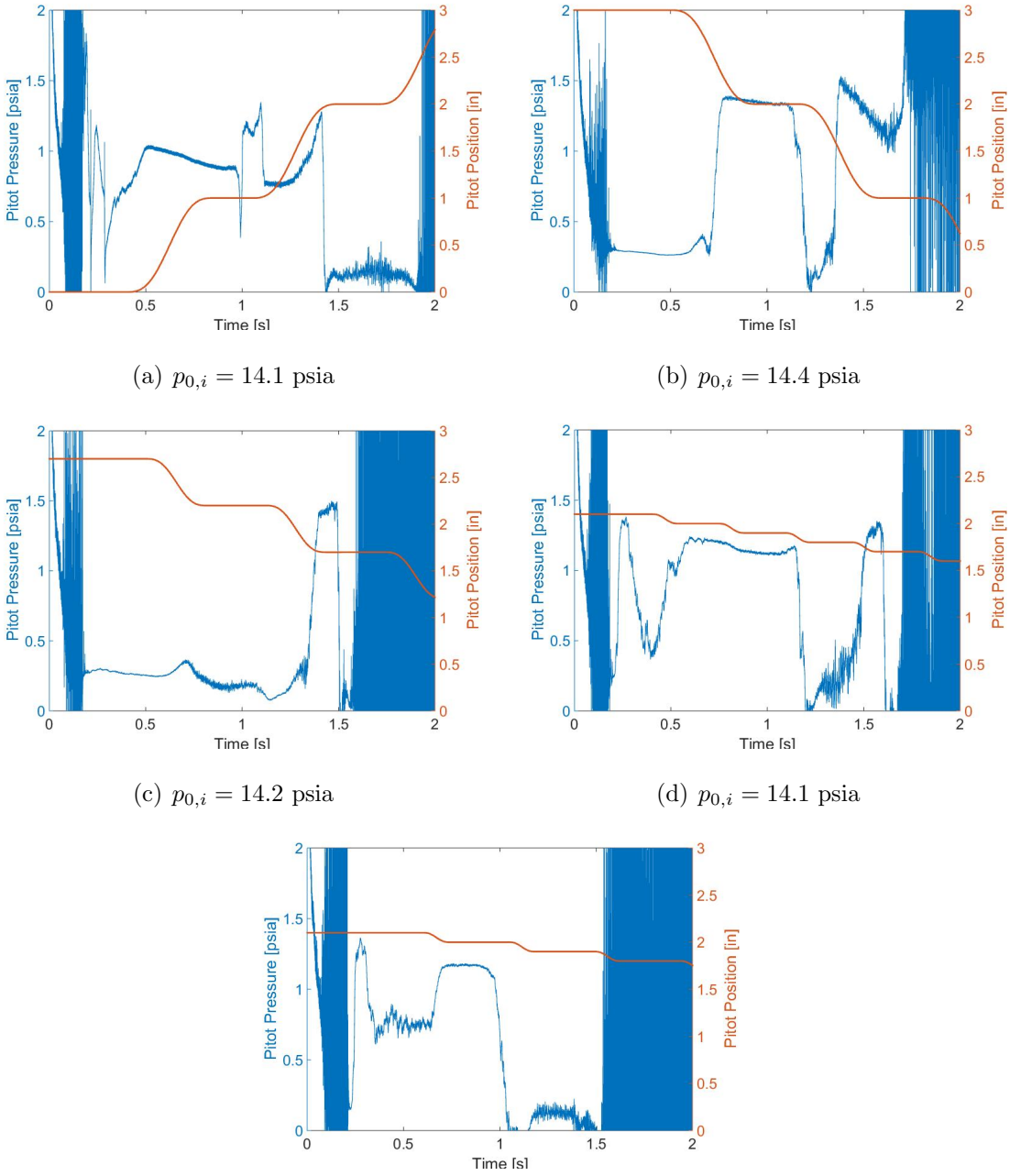

(a) $p_{0,i} = 14.1$ psia

(b) $p_{0,i} = 14.4$ psia

(c) $p_{0,i} = 14.2$ psia

(d) $p_{0,i} = 14.1$ psia

(e) $p_{0,i} = 14.2$ psia

Figure 3.40. Pitot pressure plotted with vertical position for the atmospheric runs using helium. The centerline has vertical position = 0 inches.

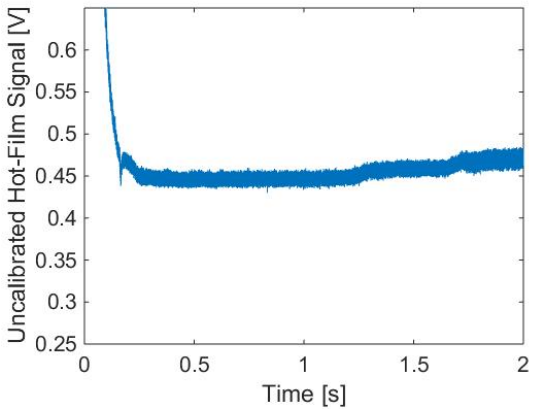

Figure 3.41. Typical uncalibrated hot-film trace for helium runs with atmospheric initial pressures.

Although only times that were specifically chosen to have stable pitot pressures were used for the data in Figure 3.42, there is still much scatter in the results. The point on the centerline for the $p_{0,i} = 80$ psia run matches closely with the numerical value, as do several of the $p_{0,i} = 40$ psia and $p_{0,i} = 14$ psia ratios. However, there is the most scatter in the results for runs which had atmospheric initial stagnation pressures. There were more runs performed at those conditions, and the variation in the ratios is likely due in part to the change in calibration offset that occurred between runs that cannot be accounted for with the present data. Still, there are enough points that match well with computations to indicate that there are times where helium results in uniform flow. In addition to calibration uncertainties, the scatter likely indicates a very unstable and unsteady flow. Perhaps unsteady nozzle-wall boundary-layer separation is causing the variations. Additionally, there are points for the atmospheric runs which were taken at locations inside the simulated nozzle-wall boundary layer ($y > 2.7$ in.) which do not agree as well with those points closer to the centerline. If these locations are in fact within the boundary layer, it could explain some of the unsteadiness seen in the pitot-pressure traces shown in Figure 3.40. The pressure ratios for atmospheric near $y = 2$ in. also have more scatter than those close to the centerline. This indicates that the flow near the core is more uniform and steady

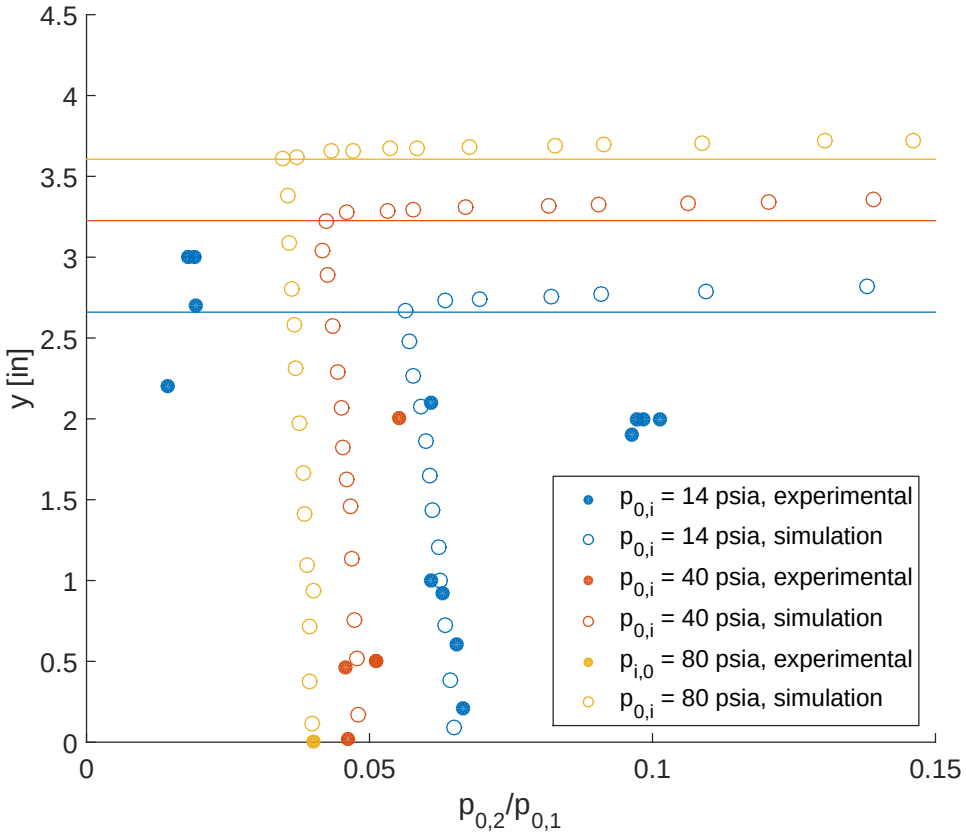

Figure 3.42. Ratios of pitot to stagnation pressure for helium. Lines indicate the approximate estimate of the boundary-layer edge based on the simulated pressure ratios. Probe located at $z = 93$ in.

than the flow closer to the nozzle wall and supports the theory that the nozzle-wall boundary layer experiences unsteady separation.

The Mach number was calculated from the experimental pressure ratios using the Rayleigh pitot-tube formula with $\gamma = 1.66$ for helium. This calculation is only valid outside of the nozzle-wall boundary layer, but the limited amount of data and the scatter in the experimental results do not allow an accurate determination of boundary-layer thickness. Therefore, the Mach number was determined for locations inside the numerically-determined core flow indicated by the horizontal lines in Figure 3.42. The results are compared to the numerical Mach numbers in Figure 3.43.

Predictably, these values display a similar scatter to that of Figure 3.42, and although some experimental data points do match well with computational results, the calibration offsets cause large amounts of error and uncertainty.

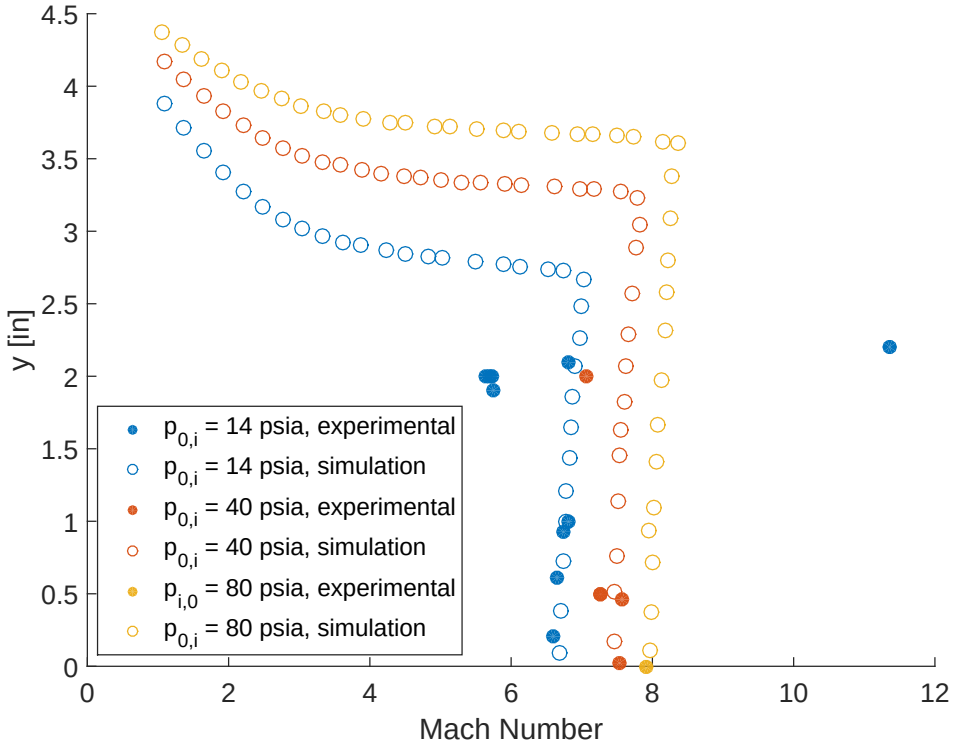

Figure 3.43. Mach numbers for helium. Probe located at $z = 93$ in.

4. CONCLUSIONS

The data presented in this thesis are composed of several projects aimed to contribute to the continuing effort towards better characterizing the BAM6QT nozzle flow. Several experiments were performed to continue and expand upon the work done by past researchers, including investigation of the effects of nozzle temperature distribution, axial location and probe geometry on the measured pitot-pressure fluctuations. Additionally, new hardware was used to measure disturbances in the presence of a model, and data were taken to characterize the flow when helium, rather than air, is used as the test gas.

Since the repolishing of the nozzle in June of 2010, the maximum consistent quiet pressure in the BAM6QT has been 170 psia. Four band heaters on the diverging section of the nozzle were used to vary the temperature distribution to determine whether the maximum quiet pressure could be raised. Each distribution had a negative temperature gradient so that temperatures decreased as z increased. For all runs, a higher temperature was observed on the upper wall of the nozzle and a lower temperature was observed on the lower wall. A distribution that increased the percent of a run that exhibited quiet flow was not found. The percentage of quiet flow in runs decreased with increasing initial stagnation pressure. Especially at $p_{0,i} = 185$ psia, significant scatter was seen in the percentage of quiet time for all temperature distributions. The heating was also not found to significantly affect the first pressure for which the flow was quiet. The maximum quiet pressure was found to be approximately 170 psia, as has been previously reported. However, the heating was limited by the nozzle. In order to maintain safe temperatures for the electroform finish, the set value was never higher than 120°C. It is possible that larger temperatures could have a stabilizing effect on the boundary layer and therefore increase the maximum quiet pressure. The new stainless steel throat, which is still being tested and has not

been extensively characterized, will be able to endure higher temperatures. It may be of interest to perform further experiments on the new nozzle.

It has been previously shown that there is an increase in quiet noise levels after approximately two seconds into the run, and the magnitude of the increase is dependent on both Reynolds number and axial location. Pitot-probe measurements were taken on the tunnel centerline at various axial locations to further study this occurrence. It was discovered that significant increases in noise levels do not occur upstream of $z = 88$ in. for $p_{0,i} = 90$ psia or upstream of $z = 86.5$ in. for $p_{0,i} = 130$ psia. The largest increase in noise level during a run was seen when $p_{0,i} = 170$ psia at $z = 93$ in. Although the cause of the increase in pressure fluctuations is still unknown, these measurements increased the precision of the known location where the noise increase occurs on the centerline. It seems unlikely that the increased noise levels are due only to temperature fluctuations in the contraction, as they depend on axial location. However, they begin at the same time as the temperature fluctuations and increase with distance downstream from the throat. It is therefore concluded that the larger noise levels later in the run are likely caused by the amplification of those initial temperature disturbances in the nozzle-wall boundary layer.

It is important to be able to compare noise levels between facilities, but measurements are often taken using different pitot probes whose sizes and shapes can affect the data. The effects of probe geometry on measured pressure fluctuation power spectral densities were investigated using three sleeves that change the forward-facing diameter of the probe. The ratios of the PSD from a case with a sleeve to the PSD from the no-sleeve case were then computed. This ratio was compared to those resulting from previous experimental data and to the ratio of transfer functions determined using direct numerical simulations assuming planar acoustic freestream disturbances at an angle of 120°. The three data sets had some scatter, but typically a peak between 0 - 50 kHz was observed in the ratios for both experimental and computational results. Although the transfer function cannot be experimentally determined, using the ratio of PSDs to compare to computations allows the study of geometry effects.

The results suggest that using a constant transfer function regardless of frequency is an oversimplification, since there is a clear frequency dependence based on the size of the sleeve. However, the peak frequencies and amplitudes do not match between experimental data sets. A significant effort was expended to determine the causes of these differences, but a likely source has not been identified. Although the cause of these discrepancies is unknown, the combination of experimental and numerical data could allow for an accurate method of computing the transfer function for the geometry used for these measurements. This would be an important step in the quest to determine the transfer function for the various geometries of pitot probes, which can be crucial when comparing measurements of noise taken in different wind tunnels.

Although the noise levels in the BAM6QT have been consistently shown to be on the order of 0.01%, the determination that the flow is quiet has typically been made using either pitot probes or hot wires in the tunnel without a model installed. It had not been confirmed that the flow remains fully quiet in the presence of a model. A new pitot-probe apparatus was designed that was mounted on the back of a 7° circular cone. An approximate shock location was measured based on the pitot pressure and measurements were taken both inside and outside the cones shock. Although the PSDs differed from typical freestream pitot-probe data, the flow was confirmed to be quiet at the aft end of the model with noise levels generally increasing as distance from the cone surface (h) increased. The exact reason for this trend is unknown, but even the position farthest from the cone produced noise levels consistent with quiet flow.

The measurements taken using helium were unusual compared to those typically seen when air is used. The hot-film traces were significantly different, and appear to indicate that Mach-6 flow lasted little more than a second. The pitot pressures do not steadily decrease, like they do when air is used, but rather there are significant discontinuities and jumps in the values. When time intervals are chosen specifically so that the pressure is relatively constant, the stagnation pressure ratios and calculated Mach numbers somewhat agree with the values determined computationally. The

thicker boundary layer in helium resulted in a smaller uniform core than the BAM6QT produces for air. The good agreement near the centerline indicates that there may be short periods of good flow, particularly in locations farther from the nozzle wall. However, there is significant scatter, which indicate that there are unsteady effects present as well. For example, unsteady separation of the nozzle-wall boundary layer could cause the discontinuities in the pitot-pressure trace and scatter in the pressure ratios. Furthermore, there is significant uncertainty due to the calibration offsets caused by helium diffusing across the Kulite diaphragm over the course of the tests.

4.1 Suggestions for Future Work

The work done for this thesis in no way completes the task of characterizing the BAM6QT nozzle. Even if a full characterization covering every aspect of the flow could be performed, measurements would need to be continuously taken so that the understanding of the tunnels properties remained up-to-date. The performance of the recently-completed stainless-steel nozzle will need to be investigated. In addition to that effort, the following projects are suggested based on the experiments presented in this thesis.

1. There are many potential avenues for future work with the band heaters on the diverging section of the model. Based on the literature that suggested that decreasing temperatures would stabilize the boundary layer, only temperature distributions that had a negative gradient were used. However, it is possible that other temperature distributions could have the desired effect. In addition, the new stainless-steel nozzle will be able to withstand higher temperatures. Further work with the band heaters should be done to determine if higher set points allow for higher quiet temperatures.

2. It appears that the increase in noise levels observed after two seconds of quiet flow may be due to temperature fluctuations which originate in the contraction and are amplified in the nozzle-wall boundary layer. To determine if this is the

case, measurements could be taken using sensors that are flush with the nozzle wall. Since the pressure fluctuations that radiate to the centerline originate upstream of the measured location, these sensors would need to be placed near the acoustic origin of the fluctuations, which is upstream of the axial position for which the centerline first experiences the noise increase. PCB sensors, which are capable of measuring higher frequencies than Kulite pressure transducers, may be able to measure the growth of the instabilities on the nozzle wall. However, they would add roughness to the wall which would be difficult to account for.

3. It goes without saying that much work remains to be performed to investigate the effects that pitot-probe geometry has on the measured pressure fluctuations. In general, there are endless experiments that could be made using different geometries. The specific hardware used in this thesis should be tested again so that the reasons for the discrepancies between the data taken by the author and those taken by Sweeney might be determined. Discovering the cause of the differences between data sets is crucial for this work because confidence in the experimental results is necessary if they are to be used to verify computations. One possible source of uncertainty in the experiments may be due to slight variations in probe geometry. Small differences in probe angle of attack or sleeve-Kulite flushness may cause unexpected variations. To determine concretely if the differences resulted from using the pin-and-socket connectors on a cut Kulite cable, simple freestream measurements using one probe geometry should be taken, first using the sensor with the cable intact and then using the same sensor with the connectors used on the cut wire. All other variables (tunnel location, Kulite conditioning box, probe geometry, etc.) should remain constant. Finally, although significant effort was expended to ensure the author reproduced the methods carried out by Sweeney, it is possible that the results were affected by some unknown factor resulting from two different experimenters collecting the data. Even once the source of the discrepancies between experimental data sets is found, the cause of the differences between experiments and

simulations will need to be further investigated. This may include using probes of different geometries and assuming a different freestream disturbance field for simulations.

4. If further experiments are to be made using helium in the BAM6QT, more measurements should be taken to improve the understanding of the flowfield. For initial measurements, the automated traverse should not be used. Keeping the pitot probe on the centerline would decrease the potential sources of uncertainty and allow cleaner measurements. Perhaps most importantly, pressure and Kulite voltage data should be recorded after each run made using helium so that the calibration offset can be determined and accounted for. This source of error is likely the largest cause of the scatter in the Mach number calculations, and more accurate sensor calibrations are needed. Finally, measurements might be made to determine if unsteady nozzle-wall boundary-layer separation is the cause of the scatter in the pressure ratio and Mach number results. This could be examined with a Kulite pressure sensor installed on the nozzle wall in addition to the pitot-probe Kulite sensor in the freestream and determining if nozzle-wall separation corresponds to the unsteady discontinuities in the pitot-probe pressure traces.

REFERENCES

[1] S. P. Schneider. Development of Hypersonic Quiet Tunnels. *Journal of Spacecraft and Rockets*, 45(4):641–664, July - August 2008.

[2] I. E. Beckwith and C. G. Miller, III. Aerothermodynamics and Transition in High-Speed Wind Tunnels at NASA Langley. *Annual Review of Fluid Mechanics*, 22(1):419–439, 1990.

[3] S. P. Schneider. Effects of High-Speed Tunnel Noise on Laminar-Turbulent Transition. *Journal of Spacecraft and Rockets*, 38(3):323–333, May - June 2001.

[4] K. M. Casper, H. B. Johnson, and S. P. Schneider. Effect of Freestream Noise on Roughness-Induced Transition for a Slender Cone. *Journal of Spacecraft and Rockets*, 48(3):406–413, May - June 2011.

[5] L. S. G. Kovasznay. Turbulence in Supersonic Flow. *Journal of the Aeronautical Sciences*, 20(10):657–674, October 1953.

[6] J. Laufer. Aerodynamic Noise in Supersonic Wind Tunnels. *Journal of the Aerospace Sciences*, 28(9):685–692, September 1961.

[7] S. R. Pate and C. J. Schueler. Radiated Aerodynamic Noise Effects on Boundary-Layer Transition in Supersonic and Hypersonic Wind Tunnels. *AIAA Journal*, 7(3):450–457, March 1969.

[8] J. Laufer, J. E. F. Williams, and S. Childress. Mechanism of Noise Generation in the Turbulent Boundary Layer. *AGARD*, AGARDograph 90, November 1964.

[9] R. D. Wagner Jr., D. V. Maddalon, and L. M. Weinstein. Influence of Measured Freestream Disturbances on Hypersonic Boundary-Layer Transition. *AIAA Journal*, 8(9):1664–1670, September 1970.

[10] T. Vrebalovich. On Supersonic Wind Tunnels with Low Freestream Disturbances. *Journal of Applied Mechanics*, 27(6):362–364, June 1960.

[11] J. Donaldson and S. Coulter. A Review of Free-Stream Flow Fluctuation and Steady-State Flow Quality Measurements in the AEDC/VKF Supersonic Tunnel A and Hypersonic Tunnel B. *AIAA Paper 95-6137*, April 1995.

[12] H. W. Liepmann. On the Acoustic Radiation from Boundary Layers and Jets. Unpublished GALCIT Report No. 79, Submitted to NACA in Partial Fulfillment of Contract NAw-6288, Avaiable on the California Institute of Technology Website, August 1954.

[13] S. R. Pate. Effects of Wind Tunnel Disturbances on Boundary-Layer Transition with Emphasis on Radiated Noise: A Review. *AIAA Paper 80-0431*, March 1980.

[14] P. C. Stainback and R. A. Rainey. Correlation of Freestream Pressure Disturbances in Supersonic Wind Tunnels. *AIAA Journal*, 14(2):286–288, February 1976.

[15] L. Duan, M. M. Choudhari, and C. Zhang. Pressure Fluctuations Induced by a Hypersonic Turbulent Boundary Layer. *Journal of Fluid Mechanics*, 804:578–607, 2016.

[16] K. R. Czarnecki and A. R. Sinclair. Factors Affecting Transition at Supersonic Speeds. Technical report, NACA RM L53I18a, November 1953.

[17] C. J. Schueler. A Comparison of Transition Reynolds Numbers from 12-in. and 40-in. Supersonic Tunnels. Technical report, AEDC-TDR-63-57, March 1963.

[18] A. J. Laderman. Review of Wind-Tunnel Freestream Pressure Fluctuations. *AIAA Journal*, 15(4):605–608, April 1977.

[19] N. S. Dougherty, Jr. Correlation of Transition Reynolds Number with Aerodynamic Noise Levels in a Wind Tunnel at Mach Numbers 2.0 - 3.0. *AIAA Journal*, 13(12):1670–1671, December 1975.

[20] E. C. Marineau. Prediction Methodology for Second-Mode-Dominated Boundary-Layer Transition in Wind Tunnels. *AIAA Journal*, 55(2):484–499, February 2016.

[21] I. E. Beckwith, F.-J. Chen, and M. R. Malik. Transition Research in the Mach 3.5 Low-Disturbance Wind Tunnel and Comparisons of Data with Theory. *SAE Transactions*, 98:1926–1933, 1989.

[22] I. E. Beckwith, T. R. Creel, Jr., F.-J. Chen, and J. M. Kendall. Free-Stream Noise and Transition Measurements on a Cone in a Mach 3.5 Pilot Low-Disturbance Tunnel. NASA Technical Paper 2180, September 1983.

[23] F.-J. Chen, I. E. Beckwith, and T. R. Creel, Jr. Effects of Streamwise Variations in Noise Levels and Spectra on Supersonic Boundary-Layer Transition. *AIAA Paper 84-0010*, January 1984.

[24] A. E. Blanchard, J. T. Lachowicz, and S. P. Wilkinson. NASA Langley Mach 6 Quiet Wind-Tunnel Performance. *AIAA Journal*, 35(1):23–28, January 1997.

[25] J. W. Hofferth, R. D. W. Bowersox, and W. S. Saric. The Mach 6 Quiet Tunnel at Texas A&M: Quiet Flow Performance. *AIAA Paper 2010-4794*, June 2010.

[26] L. Lees. The Stability of the Laminar Boundary Layer in a Compressible Fluid. Technical Report 876, NACA, 1947.

[27] L. M. Mack. On the Application of Linear Stability Theory to the Problem of Supersonic Boundary-Layer Transition. *AIAA Paper 74-134*, January 1974.

[28] A. Fedorov. Transition and Stability of High-Speed Boundary Layers. *Annual Review of Fluid Mechanics*, 43:79–95, 2011.

[29] L. M. Mack. Effect of Cooling on Boundary-Layer Stability at Mach Number 3. In *Instabilities and Turbulence in Engineering Flows*, pages 175–188. Springer, 1993.

[30] W. D. Harvey, P. C. Stainback, J. B. Anders, and A. M. Cary. Nozzle Wall Boundary-Layer Transition and Freestream Disturbances at Mach 5. *AIAA Journal*, 13(3):307–314, March 1975.

[31] P. C. Stainback, J. B. Anders, W. D. Harvey, A. M. Cary, and J. E. Harris. An Investigation of Boundary-Layer Transition on the Wall of a Mach 5 Nozzle. *AIAA Paper 74-136*, January 1974.

[32] J. A. Masad and A. H. Nayfeh. Laminar Flow Control of Subsonic Boundary Layers by Suction and Heat-Transfer Strips. *Physics of Fluids A: Fluid Dynamics*, 4(6):1259–1272, February 1992.

[33] G. Gasperas. Effect of Wall Temperature Distribution on the Stability of the Compressible Boundary Layer. *AIAA Paper 89-1894*, June 1989.

[34] A. Demetriades. Stabilization of a Nozzle Boundary Layer by Local Surface Heating. *AIAA Journal*, 34(12):2490–2495, December 1996.

[35] S. P. Schneider. Design of a Mach-6 Quiet-flow Wind-Tunnel Nozzle Using the e**N Method for Transition Estimation. *AIAA Paper 98-0547*, January 1998.

[36] S. P. Schneider. Laminar-Flow Design for a Mach-6 Quiet-Flow Wind Tunnel Nozzle. *Current Science*, 79(6):790–799, September 2000.

[37] T. Vrebalovich. *The Development of Direct and Alternating Current Glow Discharge Anemometers for the Study of Turbulence Phenomena in Supersonic Flow*. PhD thesis, California Institute of Technology, Pasadena, California, 1954.

[38] R. G. Folsom. Review of the Pitot Tube. *Transactions of the ASME*, 78:1447–1460, 1956.

[39] P. C. Stainback and R. D. Wagner. A Comparison of Disturbance Levels Measured in Hypersonic Tunnels Using a Hot-Wire Anemometer and a Pitot Pressure Probe. *AIAA Paper 72-1003*, September 1972.

[40] S. R. C. Ali, J. Wu, R. Radespiel, T. Schilden, and W. Schröder. High-Frequency Measurements of Acoustic and Entropy Disturbances in a Hypersonic Wind Tunnel. *AIAA Paper 2014-2644*, June 2014.

[41] A. Bounitch, D. R. Lewis, and J. F. Lafferty. Improved Measurements of "Tunnel Noise" Pressure Fluctuations in the AEDC Hypervelocity Wind Tunnel No. 9. *AIAA Paper 2011-1200*, January 2011.

[42] M. McGilvray, P. A. Jacobs, R. G. Morgan, R. J. Gollan and C. M. Jacobs. Helmholtz Resonance of Pitot Pressure Measurements in Immpulsive Hypersonic Test Facilities. *AIAA Journal*, 47(10):2430–2439, October 2009.

[43] H. G. Hornung and N. J. Parziale. Spectral Characteristics of Pitot Noise. *29th International Symposium on Shock Wave Paper 0301*, 2015.

[44] R. S. Chaudhry and G. V. Candler. Computing Measured Spectra from Hypersonic Pitot Probes with Flow-Parallel Freestream Disturbances. *AIAA Journal*, 55(12):4155–4166, December 2017.

[45] H. W. Liepmann and A. Roshko. *Elements of Gasdynamics*. Wiley, New York, 1957.

[46] L. Duan, M. M. Choudhari, A. Chou, F. Munoz, S. R. C. Ali, R. Radespiel, T. Schilden, W. Schröder, E. C. Marineau, K. M. Casper, R. S. Chaudhry, G. V. Candler, K. A. Gray, and S. P. Schneider. Characterization of Freestream Disturbances in Conventional Hypersonic Wind Tunnels. *AIAA Paper 2018-0347*, January 2018.

[47] R. S. Chaudhry, G. V. Candler, K. A. Gray, and S. P. Schneider. Computations of Measured Pitot-Probe Spectra using Angled Freestream Disturbances and Comparisons to Experiments, January 2019. Submitted to the AIAA Science and Technology Forum and Exposition 2019.

[48] S. P. Schneider and C. Skoch. Mean Flow and Noise Measurements in the Purdue Mach-6 Quiet-Flow Ludwieg Tube. *AIAA Paper 2001-2778*, June 2001.

[49] S. P. Schneider, C. Skoch, S. Rufer, S. Matsumura, and E. Swanson. Transition Research in the Boeing/AFOSR Mach-6 Quiet Tunnel. *AIAA Paper 2002-0302*, January 2002.

[50] S. P. Schneider, C. Skoch, S. Rufer, and E. Swanson. Hypersonic Transition Research in the Boeing/AFOSR Mach-6 Quiet Tunnel. *AIAA Paper 2003-3450*, June 2003.

[51] M. P. Borg. Characteristics of the Contraction of the Boeing/AFOSR Mach-6 Quiet Tunnel. Master's thesis, Purdue University School of Aeronautics and Astronautics, West Lafayette, Indiana, December 2005.

[52] T. J. Juliano. Nozzle Modifications for High-Reynolds- Number Quiet Flow in the Boeing/AFOSR Mach-6 Quiet Tunnel. Master's thesis, Purdue University School of Aeronautics and Astronautics, West Lafayette, Indiana, December 2006.

[53] C. R. Skoch. *Disturbances from Shock/Boundary-Layer Interactions Affecting Upstream Hypersonic Flow*. PhD thesis, Purdue University School of Aeronautics and Astronautics, West Lafayette, Indiana, December 2005.

[54] L. E. Steen. Characterization and Development of Nozzles for a Hypersonic Quiet Wind Tunnel. Master's thesis, Purdue University School of Aeronautics and Astronautics, West Lafayette, Indiana, December 2010.

[55] C. J. Sweeney. Characterization of a Hypersonic Quiet Wind Tunnel Nozzle. Master's thesis, Purdue University School of Aeronautics and Astronautics, West Lafayette, Indiana, December 2016.

[56] F. D. Turbeville. Helium Filling Instructions. Technical report, Unpublished, Purdue University, October 2017.

[57] S. Beresh, J. Henfling, R. Spillers, and B. Pruett. Measurements of Fluctuating Wall Pressures Beneath a Supersonic Turbulent Boundary Layer. *AIAA Paper 2010-0305*, January 2010.

[58] J. B. Edelman. Secondary Instabilities of Hypersonic Stationary Crossflow Waves. Master's thesis, Purdue University School of Aeronautics and Astronautics, West Lafayette, Indiana, December 2016.

[59] A. Pope and K. L. Goin. *High-Speed Wind Tunnel Testing*. Wiley, New York, 1965.

[60] M. P. Borg and R. L. Kimmel. Ground Test Measurements of Boundary-Layer Instabilities and Transition for HIFiRE-5 at Flight-Relevant Attitudes. *AIAA Paper 2017-3135*, June 2017.

[61] F. D. Turbeville. Nozzle Wall Hot Film and Static Pressure Kulite Overview. Technical report, Unpublished, Purdue University, February 2018.

[62] J. D. Anderson, Jr. *Fundamentals of Aerodynamics*. McGraw-Hill, 5th edition, 2010.

[63] A. Chou, B. M. Wheaton, C. A. C. Ward, P. L. Gilbert, L. E. Steen, and S. P. Schneider. Instability and Transition Research in a Mach-6 Quiet Tunnel. *AIAA Paper 2011-283*, 2011.

[64] S. P. Schneider, S. J. Rufer, L. Randall, and C. Skoch. Shakedown of the Purdue Mach-6 Quiet-Flow Ludwieg Tube. *AIAA Paper 2001-0457*, Januaury 2001.

[65] Digiquartz Broadband Pressure Transducers and Depth Sensors with Frequency Outputs. User Manual, 2014.

[66] S. L. Esquieu. Personal Communication. E-Mail, February 2018.

[67] B. Wheaton. Aerotech Low-Noise Traverse System. Technical report, Unpublished, Purdue University, July 2010.

[68] E. O. Swanson. Mean Flow Measurements and Cone Flow Visualization at Mach 6. Master's thesis, Purdue University School of Aeronautics and Astronautics, West Lafayette, Indiana, December 2010.

A. DETAILED DRAWINGS OF HARDWARE DESIGNED FOR THE PRESENT EXPERIMENTS

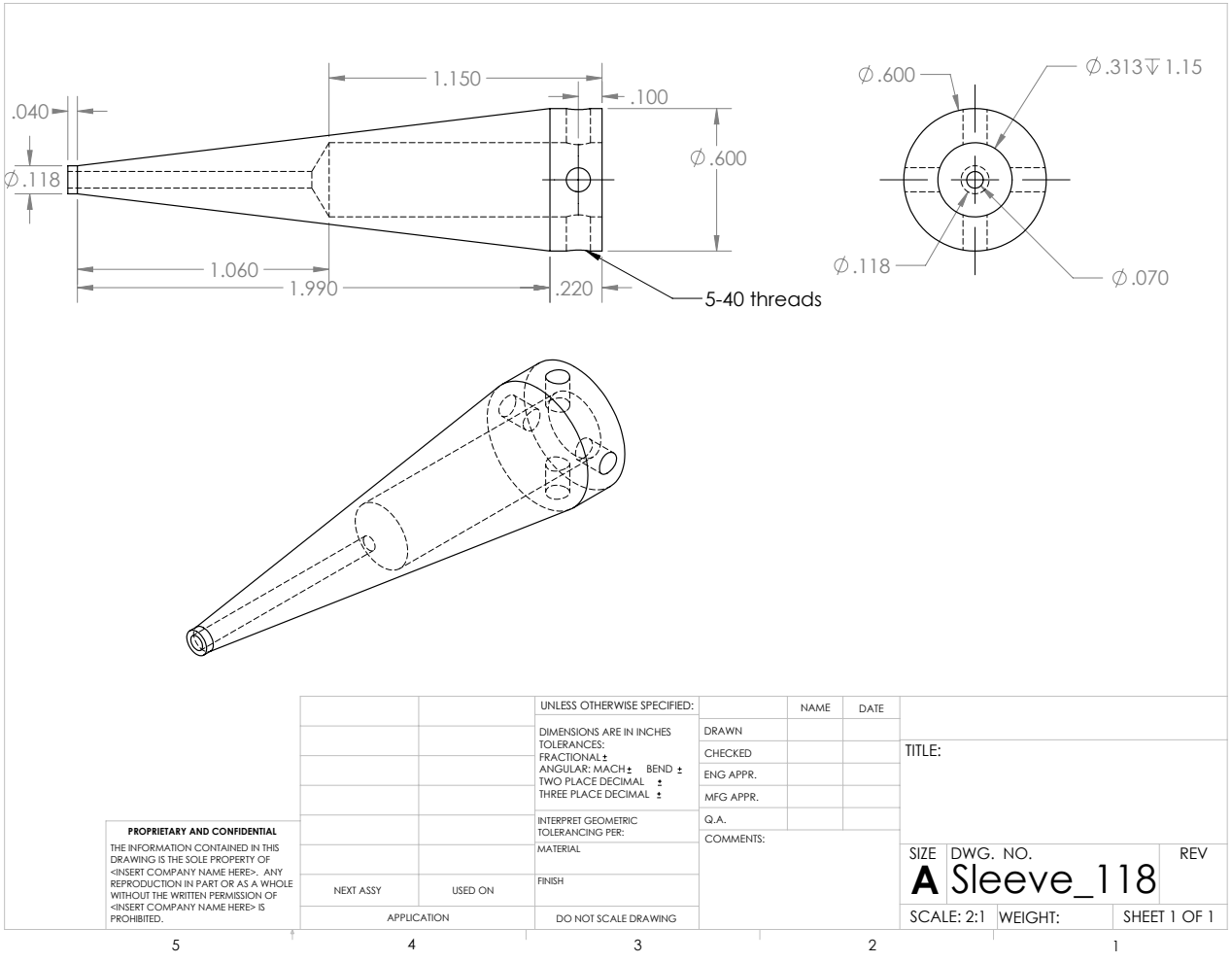

Figure A.1. The small pitot sleeve. Forward-facing diameter is 0.118 in.

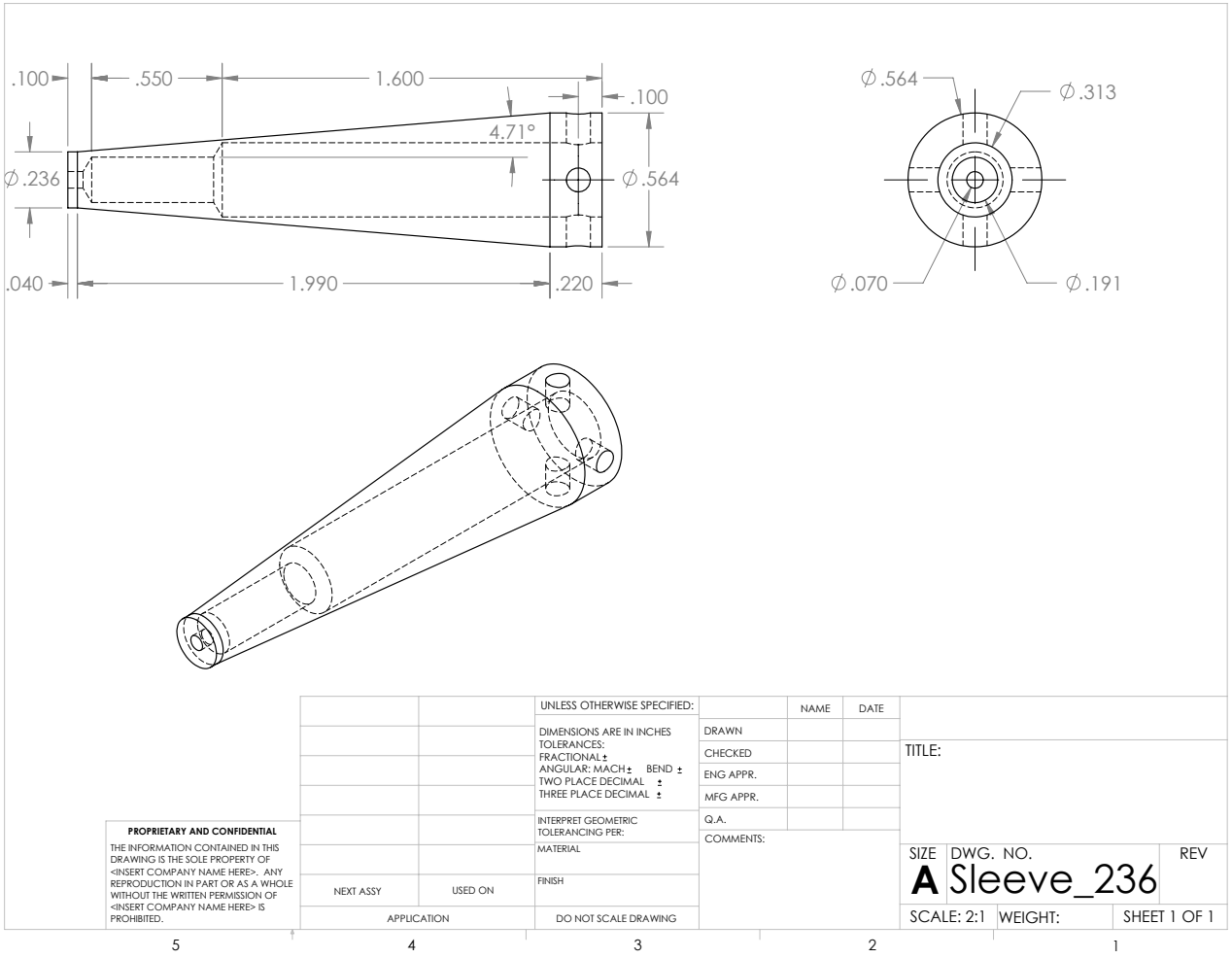

Figure A.2. The medium pitot sleeve. Forward-facing diameter is 0.263 in. Hardware designed by Sweeney [55].

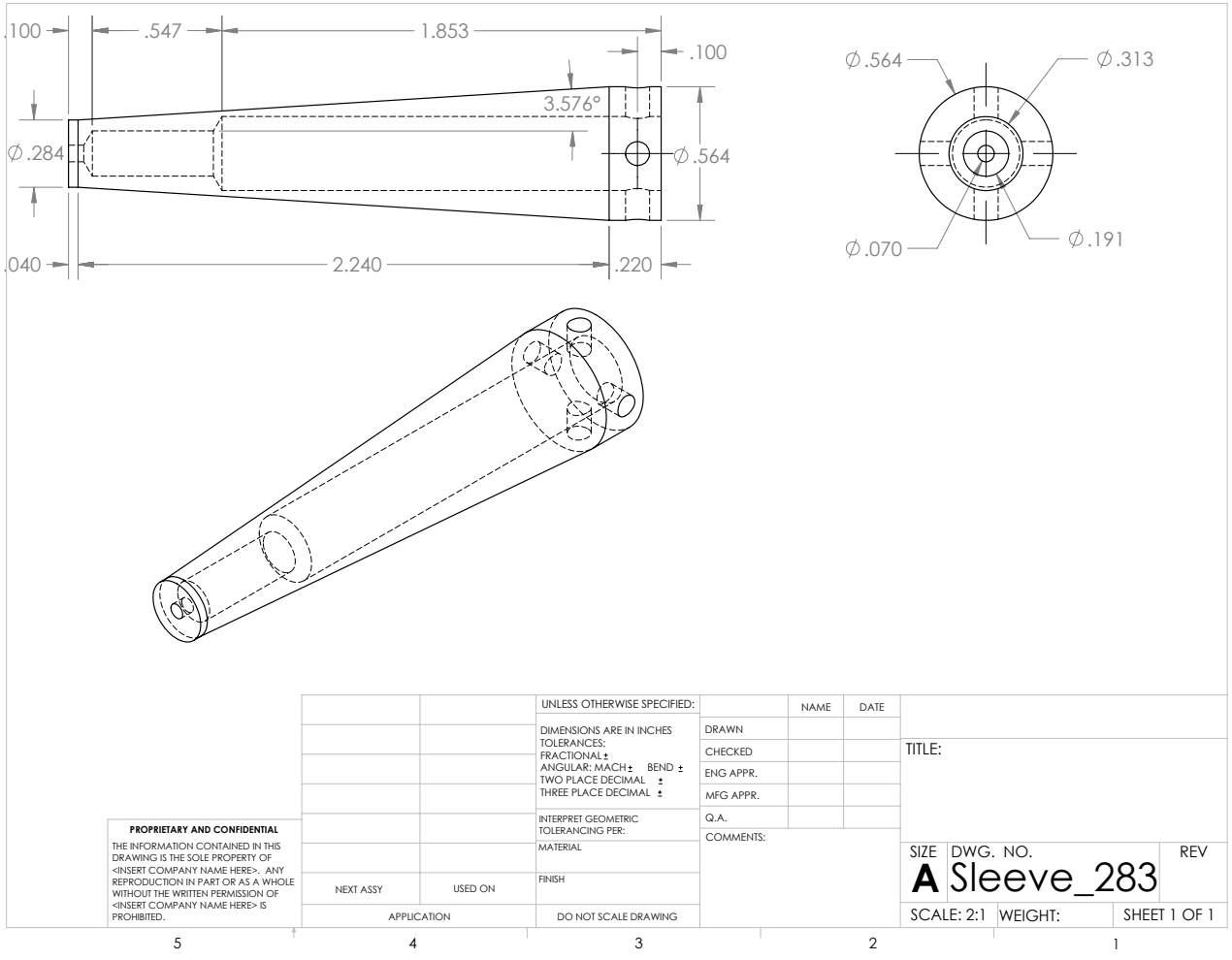

Figure A.3. The large pitot sleeve. Forward-facing diameter is 0.283 in. Hardware designed by Sweeney [55].

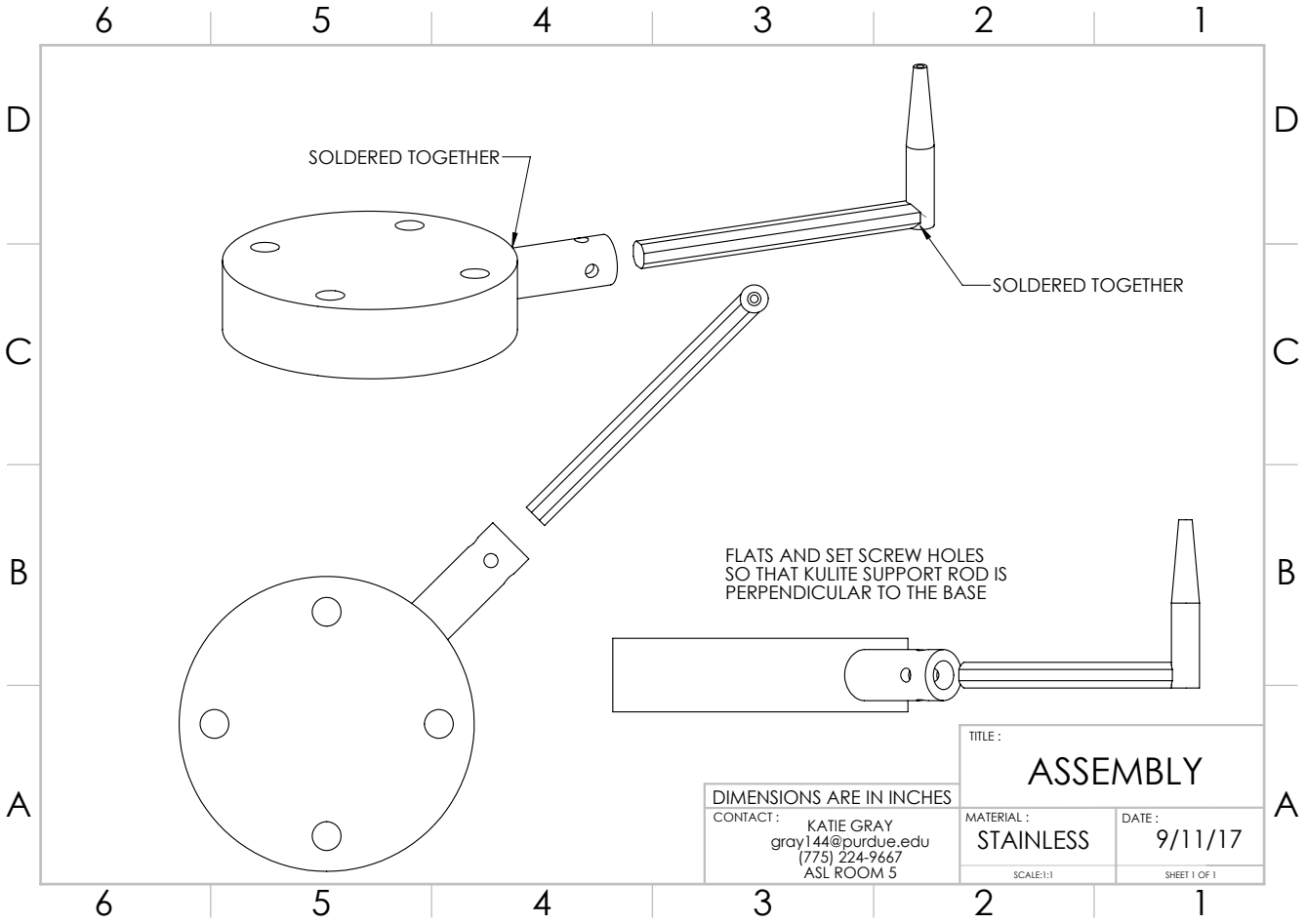

Figure A.4. The cone-mounted pitot-probe assembly.

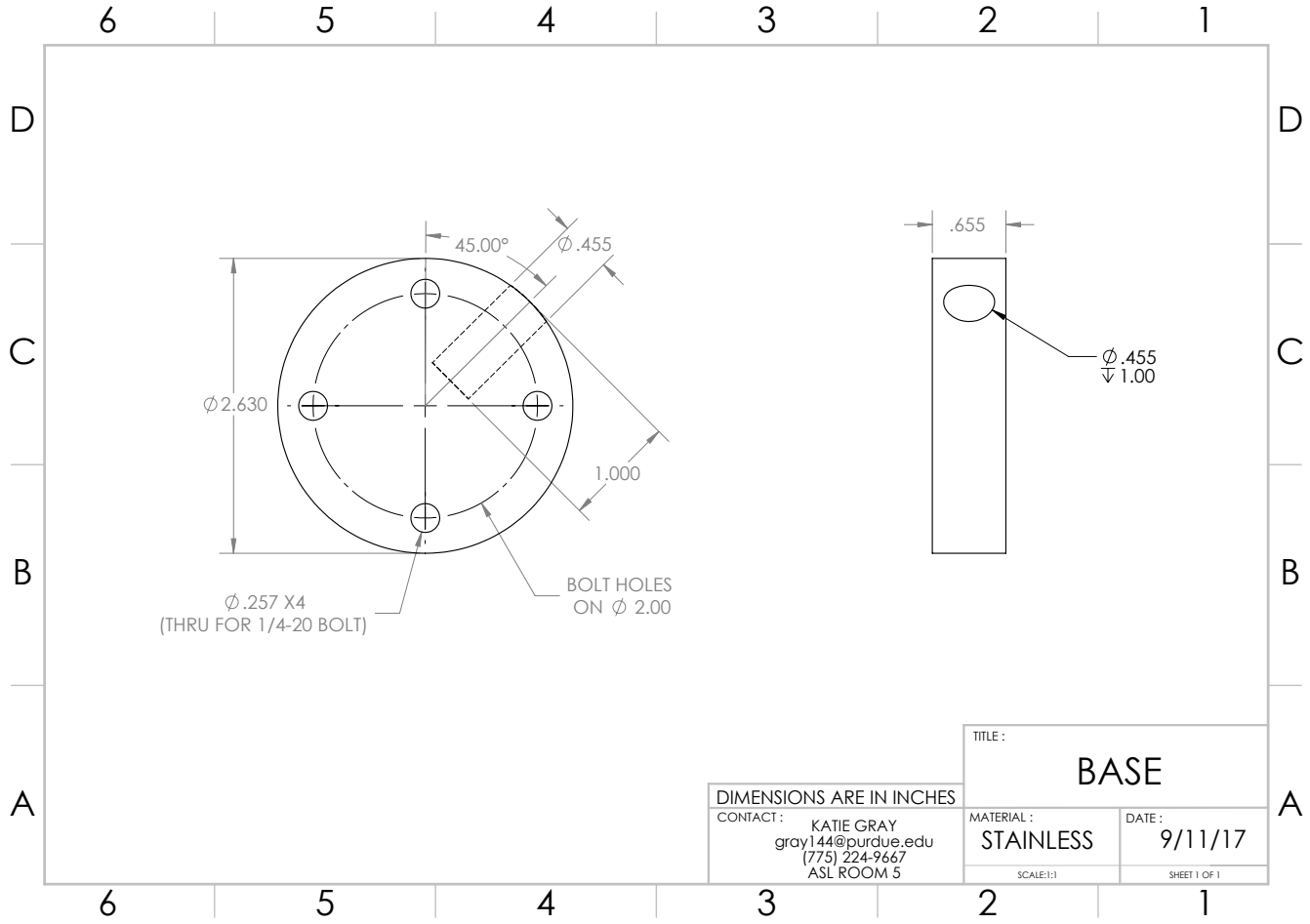

Figure A.5. The base of the cone-mounted pitot probe.

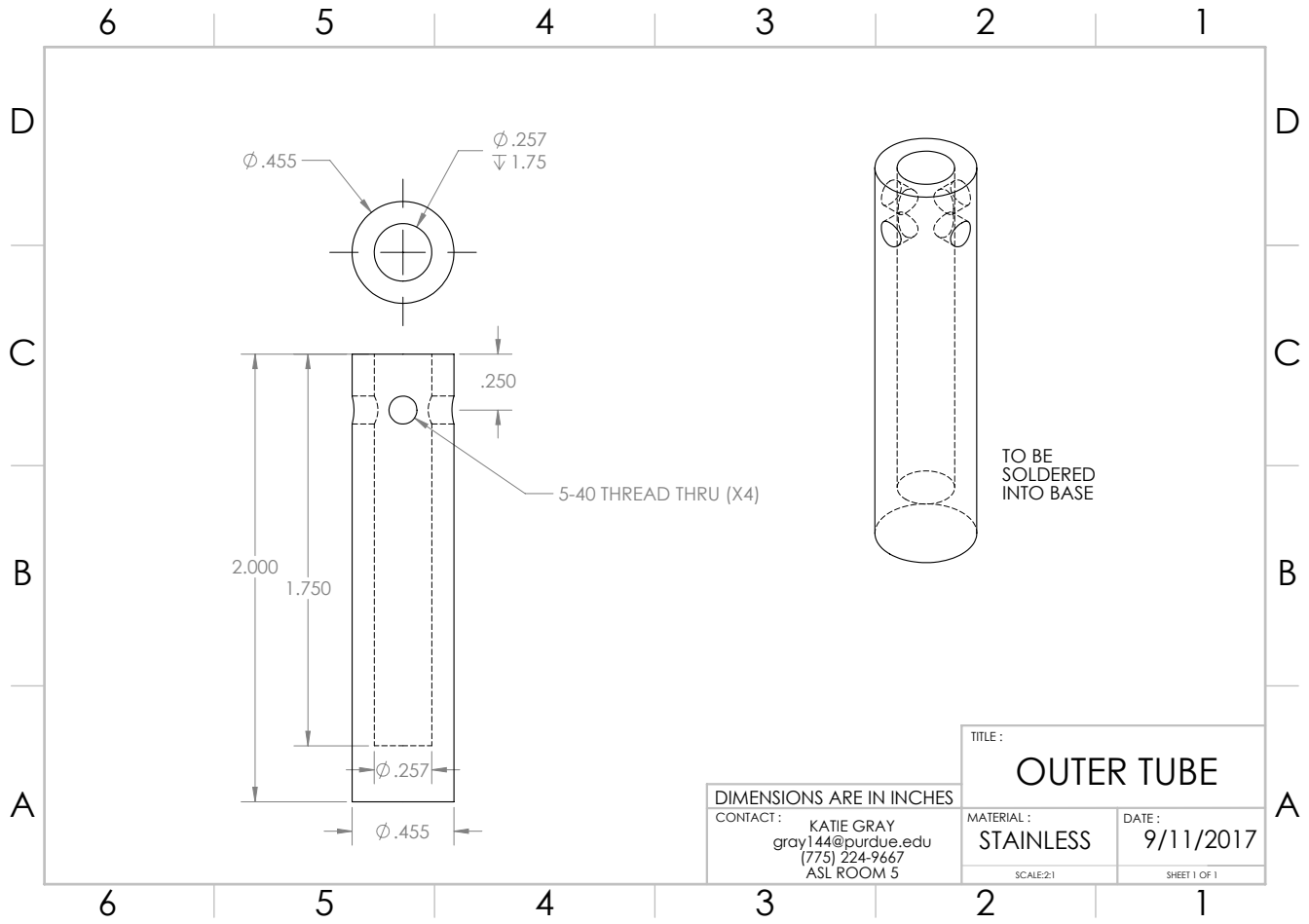

Figure A.6. The outer tube that was brazed into the base to support the inner rod for the cone-mounted pitot probe.

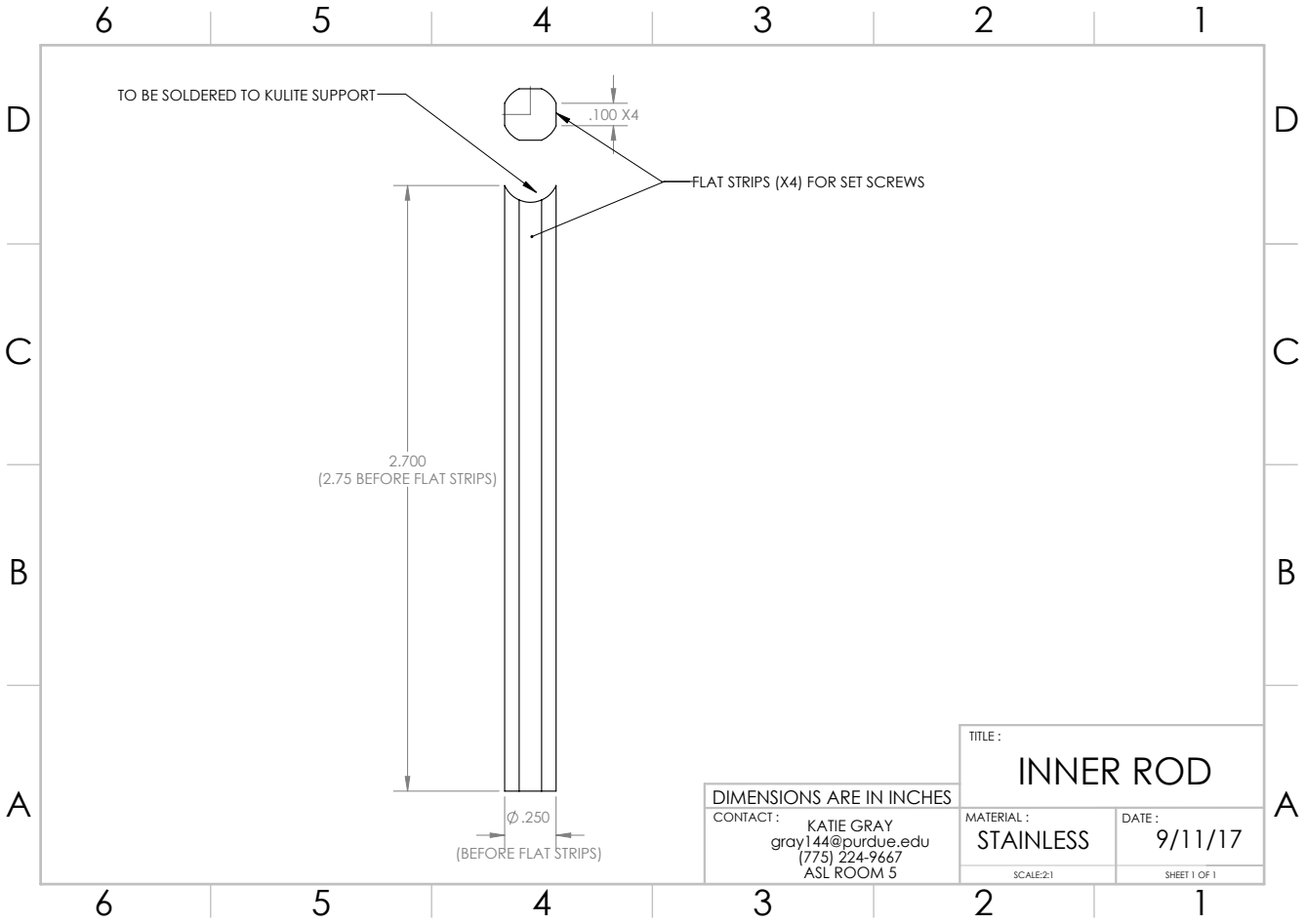

Figure A.7. The inner rod of the cone-mounted pitot probe.

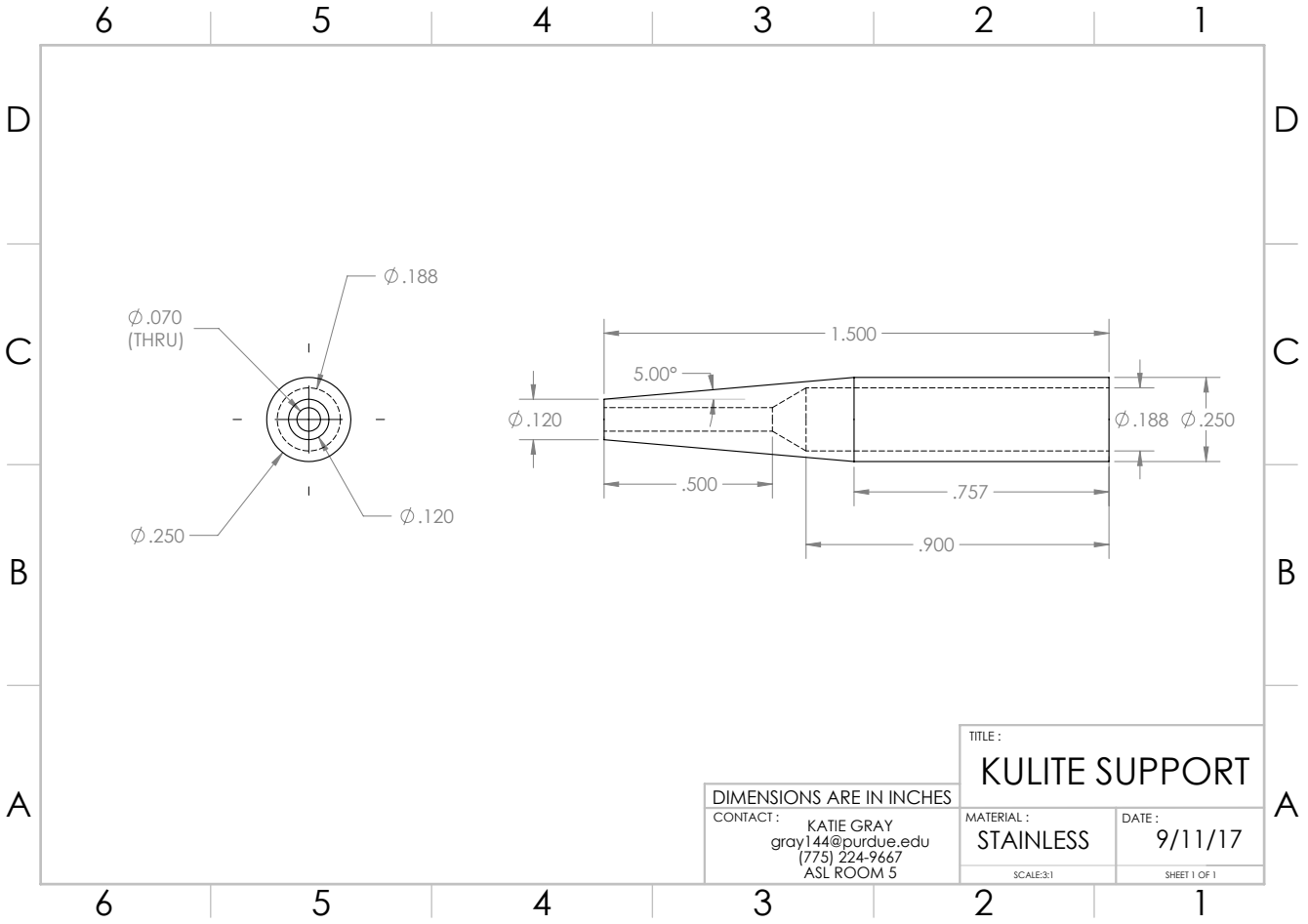

Figure A.8. The Kulite support that was brazed onto the inner rod of cone-mounted pitot probe.

B. UPDATED AUTOMATED TRAVERSE SYSTEM

The automated traverse system is used to raise and lower a pitot probe along the tunnel centerplane. The previous system consisted of a 404150XR-MP-D2H1 Parker Square Rail Positioner, an Aerotech BMS280-AH-MS-E100H brushless rotary motor, and an Aerotech NDriveHL 10-80-A-IO controller. The controller's switching power supply was discovered to introduce electronic noise, and as a result two Schaffner FN2070-10-06 EMI filters were installed on the power lines. The switching power supply was later replaced by Aerotech with inputs for an external linear DC power supply, which eliminated this source of noise. The power cable was outfitted with a Schaffner EMI filter. Further details about the previous system can be found in Reference [67].

B.1 New Components

The motor and controller were both replaced in the fall of 2017. The new motor is an Aerotech BMS280-E1000H brushless rotary motor, and the new controller is an Aerotech NDRIVEHLE 10-80-A-IO with updated A3200 motion control software. For this new model, the factory replaced the switching power supply with a linear supply for all production units and therefore the new controller does not have the same electronic noise that the old controller originally had. There was no need for an external power supply, and the controller was plugged into a wall outlet using the same power cable with the Schaffner EMI filter.

B.2 Specifications

The Parker linear positioner has a maximum velocity of 60 rev/s and a maximum acceleration of 4,000 rev/s^2. The motor has a rated speed of 50 rev/s. Because the positioner moves 5 mm for every motor revolution, this corresponds to 250 mm/s or 9.84 in/s. The positioner has a maximum velocity of 20 m/s^2. These values should not be exceeded. The linear positioner is accurate to 20 μm and the smallest unit of distance that the motor can traverse is 0.5 μm. Therefore, the traverse system is accurate to within 20 μm, or 790 μin.

B.3 Operating the Traverse

The procedure for installing pitot probes in the tunnel is unchanged, and details can be found in Reference [68]. The following useful tools are included in the A3200 software, version 5.04.003.

B.3.1 Status Utility

The Status Utility is a debugging tool that shows the status of the axes and controller tasks. The Diagnostics Tab shows the inputs for the physical hardware of the system. Most notable are the quantities FireWire Error and Analog In #1. If the controller is not properly connected to the software, the FireWire Error will read a value other than zero. The Analog Input value is the voltage that is input from an oscilloscope. Each time the traverse is used, this value should be checked, because a specific value for this parameter is what is used to trigger the Motion Controller program.

B.3.2 Configuration Manager

The Configuration Manager is used to connect the controller to the software and has a specific set of values used for the stage and motor assembly. It contains the

Parameter File, which provides the conversions between user inputs and the motion of the linear positioner. The values in this file are specific to the other components of the traverse system. Since the motor and controller are both made by Aerotech, the configuration for the motor is done automatically by selecting the correct model in the Axis Parameter Calculator. Converting the motor revolutions to linear movement can be accomplished by inputting a multiplier, found using the following equation:

$$\frac{\text{Encoder Line Count} \times 4 \times \text{Transmission Ratio}}{\text{Ball Screw Lead}} \tag{B.1}$$

The motor has an internal 1,000 line encoder, and the motor shaft is connected directly to the 5 mm ball screw with a coupler. Therefore the Encoder Line Count is 1,000 and the Transmission Ratio is 1:1, and the Ball Screw Lead is 5 mm/revolution. The factor of 4 is an internal multiplier for the controller. This results in a value of 800, and entering this into the CountsPerUnit parameter finishes configuring the parameter file to the traverse system.

B.3.3 Motion Composer

The Motion Composer can be launched after the connection is established in the Configuration Manager. There are two options for using the automated traverse that can be found in the Motion Composer tool: controlling the motion manually or by using a motion program.

The manual mode allows the user to adjust the position incrementally. This is typically the method used when moving the probe between runs. The X axis must be enabled before the motor can be run. Once the axis is enabled, the user should change the jog type to distance and input the desired increment. The arrows move the probe the set distance along the axis. **Note that the positive direction is down, and the negative direction is up.** Vertical movement is limited by the position of the clamp relative to the tunnel outer wall below and the motor above. It should also be ensured that the probe will not impact the lower tunnel wall, as this would likely damage the nozzle. The position should be checked before each movement to

ensure there is room for the desired motion. Note that if the tunnel is being run at high pressures (above 200 psia) the automated traverse system should be used to secure the probe in place even if motion is not desired during the run. This can be accomplished by simply enabling the axis and not commanding any movement. When the axis is engaged, the motor actively works to prevent movement unless otherwise specified, and this technique has prevented the probe from moving due to the violent loads that occur during tunnel startup and unstart for high pressures.

Motion programs allow the user to write a program that will control the movement of the probe. The distance, velocity, acceleration, time delay, and other parameters can be input to the program. A full list of available commands can be found in the help file. A sample program is included below. Lines which begin with an apostrophe are commented out. The program waits for a trigger from the oscilloscope before starting. The trigger results in a change in voltage ready by Analog In #1 which continues the program. The program directs the probe to wait half a second for tunnel start up and then make 6 movements upwards with a 0.3 s period of rest after each. Finally, the probe waits two seconds before returning to the starting position.

B.3.4 Sample Program

```
'Sample program written by Katie Gray, 1/2/18
'Based on Brad Wheaton's AERINTRO.PGM from 7/16/10

ENABLE X
  'turns on control for the X axis
  '(vertical motion in the tunnel and only possible axis)
HOME X
  'sets current position to 0.00, which is home (eg, on tunnel
  'centerline) NOTE: HomeType parameter should be set to 4,
  'otherwise probe might move durring this command
```

```
INCREMENTAL
  'sets programming mode to incomental. ie, all distances are
  'defined relative to previous position.
  'remains in effect until ABSOLUTE mode is specified
SECONDARY
  'uses secondary units, determined by parameter file.
  'with parameter file parameter_file_with_stage.prma
  'this means inches. Use PRIMARY to use primary units,
  'which are mm for this parameter file
SECONDS
  'specifies that feedrates are in distance units per second.
RAMP MODE RATE X
  'rate-based acceleration and deceleration which is specified
  'in parameter file.
WAIT( $AI[1].X > 1 ) -1
  'the program pauses here until the scope is triggered
  'controller waits until Analog Input #1 on the X axis is
  'less than 1 volt. this condition may need to be changed
  'depending on scope AUX out settings before and after trigger
  'the -1 means to wait infinite time
DWELL 0.5
  'probe is held in place - here, to wait for tunnel startup
REPEAT 3
  'the following will be repeated 3 times:
        LINEAR X-1 F9
          'moves probe up 1 inch because using secondary units
          '(incrementally)
          'to move downwards one inch, put X1
          'F9 dictates the velocity: 9 in/s
```

```
        'max velocity is 9.8 in/s
      DWELL 0.3
        'probe waits between movements for 0.3 seconds - here,
        'to take data
ENDRPT
  'end the repeatloop
DWELL 0.8
  'wait 0.8 seconds - arbitrary amount of time.
ABSOLUTE
  'change mode to absolute rather than incremental.
  'distances are defined relative to home
LINEAR X0 F2
  'moves probe back to home position at 2 in/sec
DISABLE X
```

B.3.5 Digital Scope

The Digital Scope program, which is also included in the software, records the positions, velocity, error, and other parameters of interest. These can be selected in the Configuration tab. Although the Digital Scope was not used during the run, the trace can be used to determine the position of the probe at any given time. Figure B.1 shows the commanded position, the position feedback, and the error between the two values for the sample program given above.

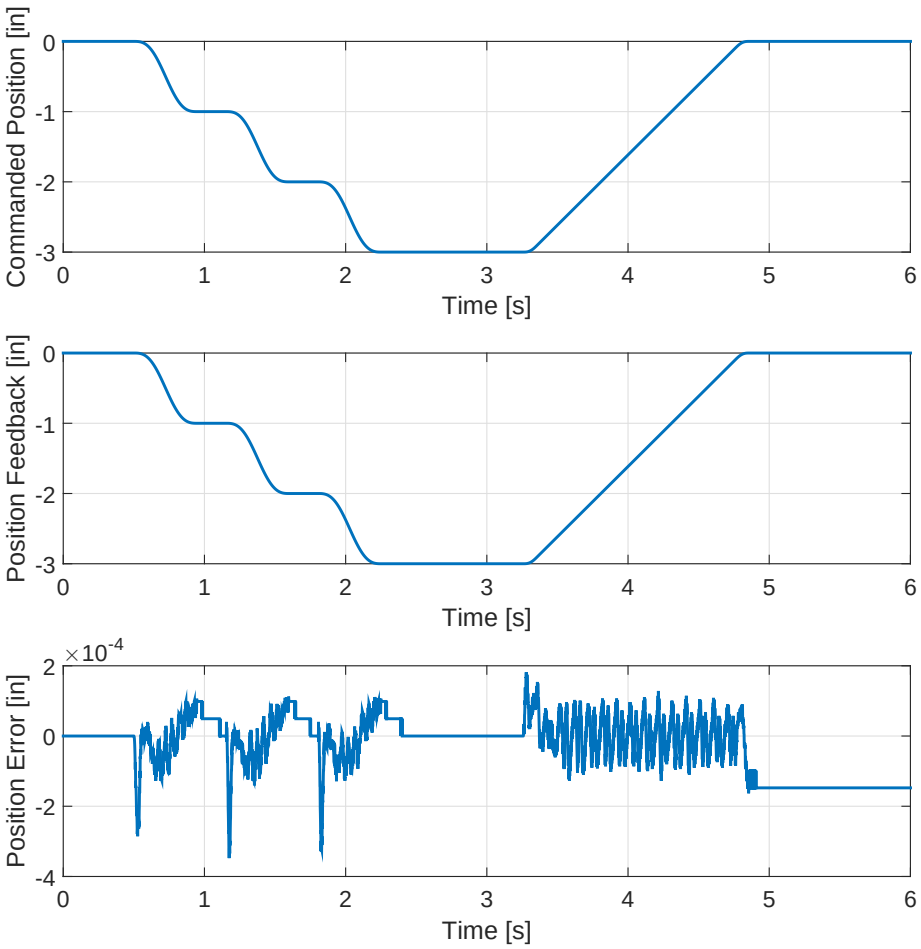

Figure B.1. The commanded position, feedback position, and position error from the Digital Scope for the sample program given above.